# COMPUTER SIMULATIONS OF LIPID BILAYER DYNAMICS

**Sergey Alfredovich Shkulipa**

Shkulipa, S. A.
Computer simulations of lipid bilayer dynamics
Thesis, University of Twente, Enschede
ISBN: 90–365–2408–3.



**Printed by**: Print Partners Ipskamp, www.ppi.nl
P.O. Box 333, 7500 AH Enschede, The Netherlands

**COMPUTER SIMULATIONS OF LIPID BILAYER DYNAMICS**

DISSERTATION

to obtain
the doctor's degree at the University of Twente,
on the authority of the rector magnificus,
prof. dr. H.W.M. Zijm,
on account of the decision of the graduation committee
to be publicly defended
on Wednesday, 22 November 2006 at 15.00

by

**Sergey Alfredovich SHKULIPA**

born on 1 March 1976
in Odessa, USSR

This dissertation has been approved by:

the promotor

Prof. dr. W.J. Briels

and the assistant-promotor

Dr. ir. W.K. den Otter

# Contents

# 1 Introduction

## 1.1 Biological membranes

The membranes of living cells serve several related yet distinct functions. One of their most obvious roles is to define the cell. The outer membrane of the cell serves as a barrier, forming the limiting boundary of every cell, while intracellular membranes compartimentalize functions into the organelles of eukaryotic cells. Various membranes of organelles have specific functions associated with them because the molecules responsible for these functions are either embedded in or localized on these membranes.

Membranes also regulate the transport in to and out of the cell. Nutrients, ions, gases, water and many other substances are taken up by the cell, while various products and waste are secreted. Membranes are differentially permeable, and are endowed with several modes of passage. Molecules such as water, oxygen and carbondioxide readily diffuse through membranes because of their small size. Charged ions, like sodium and potassium, and smallish molecules such as glucose, require special carrier proteins or channels to actively transport them across the membrane. Even molecules as large as proteins can enter or leave cells by being incorporated into vesicles, in processes called endocytosis and exocytosis respectively.

The outer membrane of the cell also plays a key role in signal recognition. Information that impinges on the cell, in the form of chemical or electrical signals, may initiate activities within the cell, such as protein production, muscle cell contraction or cell division. The signalling molecules are sometimes transmitted into the cell, but in most cases they bind to specific receptors in the plasma membrane which generate a secondary signal inside the cell.

Futhermore, membranes need to be flexible and elastic in order to allow motion and growth, to cope with external forces, and to execute many of the aformentioned tasks.

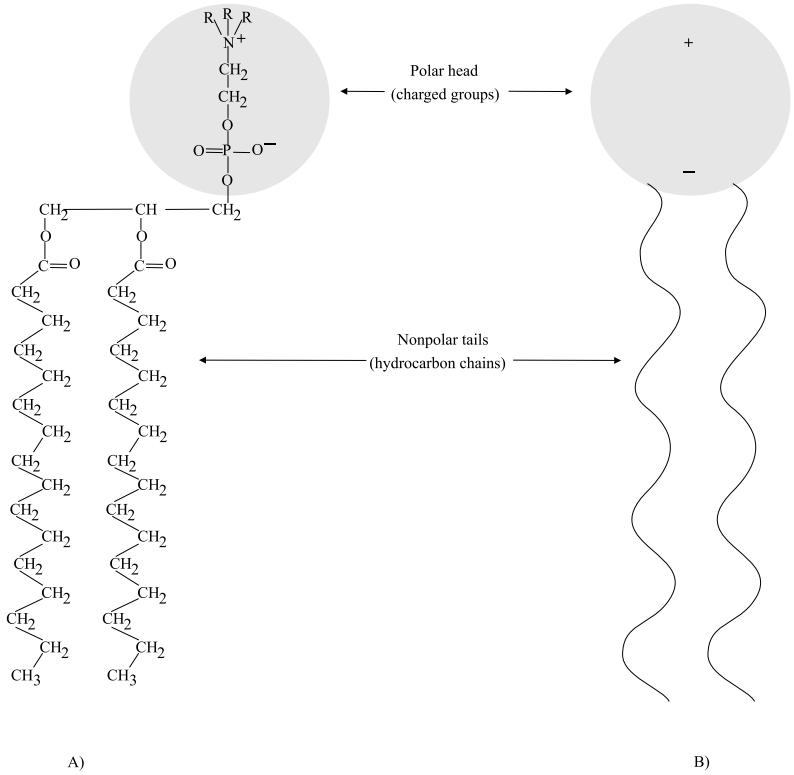


Figure 1.1: An amphiphilic molecule: (A) Chemical structure. (B) A schematic representation.

In this thesis, the dynamical properties of membranes are studied by molecular dynamics simulations. This chapter gives an overview of the preceding experimental studies of these properties, and a brief introduction to the basics of simulations. But first we discuss the physical-chemical structure which enables membranes to perform all above tasks.

## 1.2 Lipids

As we have seen, every cell and organelle needs some sort of physical barrier to keep its contents in and the external environment out, as well as some means of controlling exchange between its inside and the external environment. Ideally, such a barrier should be imper-

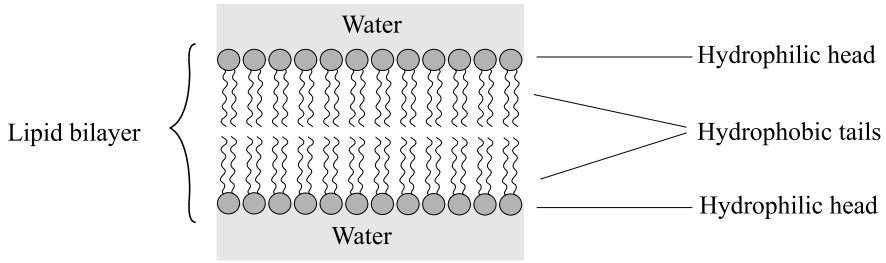


Figure 1.2: The lipid bilayer as the basis of membrane structure. Due to their amphiphatic nature, lipids in aqueous environment orient themselves in a double layer, with the hydrophobic tails buried inside and the hydrophilic heads pointing toward the aqueous milieu on either side of the membrane.

meable to most of the molecules and ions found in cells and their surroundings. Otherwise, substances could diffuse freely in and out, and the cell would not really have a defined content at all. On the other hand, the barrier cannot be completely impermeable, or else desired exchanges between the cell and its environment could not take place. Moreover, such a barrier must be insoluble in water so that it will not be dissolved by the aqueous medium of the cell. At the same time, it must be readily permeable for water, because water is the basic solvent system of the cell and must be able to flow into and out of the cell as needed. As one might expect, the membranes that surround cells and organelles satisfy these criteria admirably.

A membrane is essentially a hydrophobic permeability barrier consisting of lipids, proteins, and (in case of human and animal cells) cholesterol. These molecules have both a hydrophobic and a hydrophilic region and are therefore referred to as amphiphilic molecules (the Greek prefix amphi means ‘of both kinds’, and ‘philos’ means friend). Membrane phospholipids, illustrated in Fig. 1.1, consist of a polar ‘head’ and two nonpolar hydrocarbon ‘tails’. The polarity of the hydrophilic head is due to the presence of a negatively charged phosphate group linked to a positively charged amine. When exposed to an aqueous environment, amphiphatic molecules spontaneously arrange themselves into clusters, such that their polar heads are facing out toward the aqueous phase, shielding their hydrophobic tails from the water. The resulting structure is the bilayer shown in Fig. 1.2. The hydrocarbon tails extend inward, forming the continuous hydrophobic phase of the membrane. Every biological membrane has such a lipid bilayer as its basic structure. Each of the phospholipid layers is

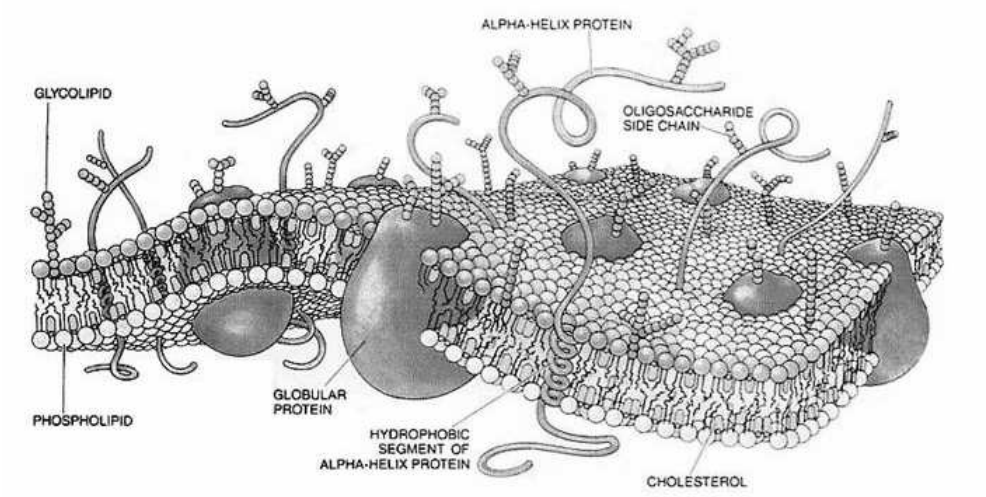


Figure 1.3: Membrane structure. Biological membranes consist of cholesterol and a variety of proteins within a lipid bilayer. *Picture copied from http://en.wikipedia.org/wiki/Cell_membrane*

about 4-5 nm thick, so the bilayer has a width of about 8-10 nm.

Embedded within or associated with the lipid bilayer are various membrane proteins, see Fig. 1.3. These proteins are almost always amphiphatic, and they orient and fold themselves in the lipid bilayer accordingly. Hydrophobic regions of the protein associate with the interior of the membrane, whereas hydrophilic regions protrude into the aqueous environment at the surface of the membrane. Depending on the particular membrane, the membrane proteins may play any of a variety of roles. Some are transport proteins, responsible for moving specific substances across an otherwise impermeable membrane. Others are enzymes that catalyse reactions associated with the specific membrane. Still others are signal receptors on the outer surface of the cell membrane. We study idealised membranes, containing no proteins.

Membranes play a key role in the cell structure – their mechanical and flow properties are important for the proper functioning of the cell. Cells in a tissue interact with their neighbours, while other cells, like red blood cells, interact with the surrounding liquid. So, every living cell experiences bending, stretching, compression, and flow deformations. Because the

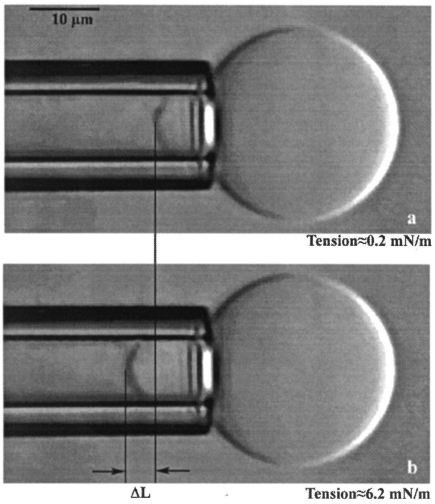


Figure 1.4: Video micrograph of a vesicle area expansion test by suction into a pipet. (a) The vesicle at low tension. (b) The vesicle at high tension. The change in projection length $\Delta L$ is proportional to the change in apparent surface area. *Picture courtesy of prof. E. Evans.*

lipids in a membrane are not covalently bond, a membrane will deform in response to these forces. The mechanical properties of membranes include the elastic modulus or area compressibility and the bending ridigity. Our focus is on the flow properties: the surface shear viscosity of a membrane resisting a lateral shear deformation and the intermonolayer friction opposing lateral velocity differences between the two leaflets of the bilayer.

## 1.3 Experiments

Over the last few decades, a variety of experimental techniques have been applied to investigate the static and dynamical properties of lipid bilayers. In this section we briefly review several relevant techniques.

Various techniques have been used to quantitate mechanical stretch properties of bilayers. Most prominent is the micropipette approach, pioneered by Evans for giant vesicles [1, 2]. This technique is based on measuring the vesicle extension in the tip of a pipette due to an applied pressure gradient, see Fig. 1.4. Photon correlation spectroscopy and dynamic

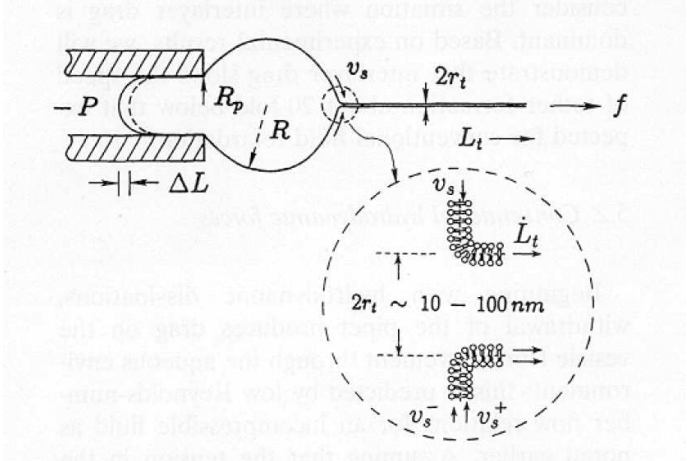


Figure 1.5: Illustration of the relative flow produced between layers as the bilayer is forced to flow through a region of enormous change in curvature ( $\sim$ 1000-fold increase) as it forms an ultrasmall tube. *Picture courtesy of prof. E. Evans.*

light scattering provide the monitoring of small vesicles under osmotic stress [3, 4]. The cryoelectron microscopy of vesicles subjected to osmotic stress [5], and NMR and x-ray diffraction of strongly dehydrated multibilayer arrays [6] are also used for the calculation of the elastic area compressibility modulus. Furthermore, the combination of NMR and x-ray techniques yields accurate determinations of the lateral area per lipid molecule.

The bending stiffness of a bilayer has traditionally been derived from a detailed analysis of thermal shape fluctuations of flaccid vesicles [7, 8, 9] and by measurement of the forces needed to pull nanoscale bilayer tubes from vesicles under tension [10, 11, 12]. Thus, the bending stiffness can be calculated directly from measurements of the tether radius as a function of force, see Fig. 1.5. The micropipette pressurization of a single vesicle can also be used to quantitate the bilayer bending modulus, measuring the entropy-driven tension that arises as thermal bending undulations are smoothed under pipette aspiration of a giant vesicle [13, 14], see Fig. 1.4.

The above described technique involves the formation of a thin tube (tether) of phospholipid bilayer from a large vesicle. Using last method [11], the intermonolayer friction of the vesicle has been measured for the first time by Evans *et al.*. The demonstration that inter-

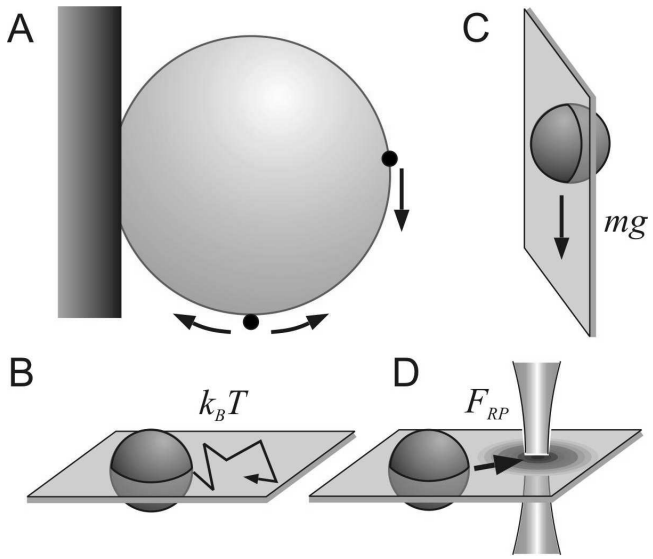


Figure 1.6: Three approaches to measure the friction coefficient of a particle moving on a membrane. (A) Vesicle fixed to a surface with two possible positions of a particle adhered to the vesicle membrane. (B) A Brownian particle performs a random walk at the bottom (or top) of the vesicle. (C) A heavy particle sediments towards the vesicle bottom due to gravity. (D) A particle is driven towards the axis of an optical trap beam by the radiation pressure force $F_{RP}$. The sketch is exaggerated in terms of particle-trap distance. *Picture courtesy of prof. R. Dimova.*

monolayer friction is an important phenomenon for the relaxation processes of fluctuating bilayers has been proved by spin echo experiments of highly ordered stacks of lipid bilayers [15] and using video microscopy studies of thermal shape fluctuations of vesicles [16]. These experiments support the theory by Evans and Yeung and by Seifert and Langer that the lipid bilayer is not a single entity, but consists of two layers coupled by friction.

The surface viscosity of lipid vesicles are also calculated in the tether formation experiment [17]. Two other optical techniques for calculating surface shear viscosity of a membrane are falling-ball viscosimetry and optical dynamometry [18, 19] see Fig. 1.6. Particles move on the surface of the vesicle, spontaneously (Brownian motion) or driven by an external force, either gravity or a laser beam's radiation pressure. The value of the membrane hydrodynamic

shear viscosity can be deduced from the analysis of the particle motion.

All of these techniques have increased our understanding of lipid bilayer and cell mechanical properties.

## 1.4 Computer simulations

Computer simulations are a very powerful technique to investigate material properties, including membranes. They serve as a complement to conventional experiments, providing detailed information on a system while allowing us full control over the system. Computer simulations act as a bridge between microscopic length and time scales and the macroscopic world of the laboratory: we provide the interactions between particles, and obtain predictions of bulk properties. Simulations also act as a bridge in another sense: between theory and experiment. We may test a theory by conducting a simulation using the same model. We may test the model by comparing with experimental results.

Molecular dynamics (MD) is based on the dynamical evolution of a many particle system. It consists of the numerical, step-by-step, solution of the classical equations of motion,

$$m_i \frac{d^2\mathbf{r}_i}{dt^2} = -\nabla \mathbf{F}_i, \tag{1.1}$$

here $m_i$ is the mass , $\mathbf{r}_i$ is the poasition, and $-\nabla\mathbf{F}_i$ is the force on interacting particle $i$. In the l.h.s. $\frac{d}{dt}$ is the time differentiation. For this purpose we need to be able to calculate the force $\mathbf{F}_i$ acting on the atoms, and these are derived from a potential energy U($\mathbf{r}_N$), where $\mathbf{r}_N = (\mathbf{r}_1, \mathbf{r}_2, ..., \mathbf{r}_N)$ represents the complete set of 3N atomic coordinates. After that we integrate Newton's equations of motion. This step and the previous one make up the core of the simulation and are calculated using for instance the Verlet scheme [20, 21],

$$\mathbf{v}_i(t + \frac{\Delta t}{2}) = \mathbf{v}_i(t - \frac{\Delta t}{2}) + \frac{\mathbf{F}_i(t)}{m_i}\Delta t \tag{1.2}$$

$$\mathbf{r}_i(t + \Delta t) = \mathbf{r}_i(t) + \mathbf{v}_i(t + \frac{\Delta t}{2})\Delta t \tag{1.3}$$

Where $\Delta t$ is an integration time step. They are repeated until we have computed the time evaluation of the system for the desired length of time.

An important aspect of simulating a system is the implementation of the boundaries. The way this is done depends on the problem under consideration. In case one is interested in bulk

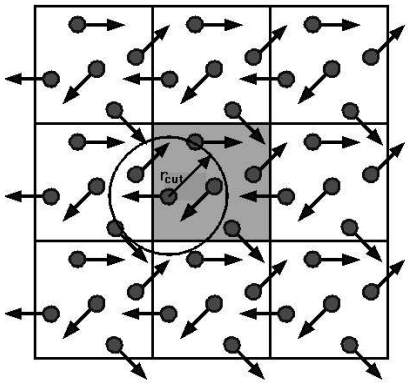


Figure 1.7: A two-dimensional periodic system. Molecules can enter and leave each box across each of the four edges. In a three-dimensional example, molecules would be free to cross any of the six sqare faces of a cube.

properties of a system, it is convenient to introduce periodic boundary conditions. The central box is repeated infinitely many times in all directions. The idea is that particles leaving the box at one side enter the box at the opposite side. This is shown in Fig. 1.7. The number of particles in a simulation box is thus conserved. In cases when non-equilibrium molecular dynamic simulations have been used to set up and maintain a steady homogeneous shear flow with a linear velocity profile we used the Lees-Edwards boundary conditions. The idea is that using 'sliding bricks' above and below the central box induces planar Couette flow in a simulation, see Fig. 1.8.

Without potential cut-off, the particles in the central box interact with all the particles in their own box as well as with all the particles in the periodic images. That remarkably decrease the speed of calculations.

In the remainder of this section we briefly review the different lipid membrane models that have been described in the literature.

Bilayer models with atomic resolution have been studied by extensive computer simulations [22, 23, 24, 25]. Since these simulations require a huge amount of computing time, they are restricted to relatively small bilayer segments which contain 50-200 amphiphilic molecules. For a lipid bilayer, this corresponds to a membrane area of the order of 3 $nm^2$ to 8 $nm^2$. With the aim of increasing efficiency of computer simulations, various simplified

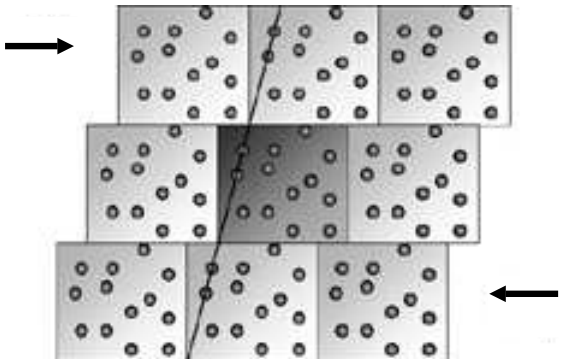

Figure 1.8: Homogeneous shear boundary conditions.

models have been introduced.

The evolution of lipid membrane models began with modelling the oil-water interface as a first approximation. The first model of the interface was a lattice model, which was proposed by Widom and co-workers [26, 27, 28, 29]. Their model of the interface predicts a three-phase equilibrium and ultra-low surface tensions. Various other lattice models with small differences from the original one (Schick and Gompper, Alexander) have since appeared in the literature. The common basic ingredient of all of them is the presence of three different chemical species $a$, $b$, and $c$ with at least unequal interactions between the amphiphile ($c$) and the water ($b$) and oil ($c$) species. The difference between them is the location of the particles, on the bonds of the lattice or on lattice sites.

Another basic model is the coarse-grained surface model for a membrane, developed by Telo da Gama and Gubbins [30, 31]. Three different chemical species are moving off-lattice with unequal interactions between the amphiphile and other two species. This model also has a lot of offsprings; for a recent reviews see [32]. The single most obvious advantage of using off-lattice models in this context is their lattice independence. All mentioned above models focus on membrane behaviour on length scales large compared to the membrane thickness. Thus, in these models the bilayer thickness is treated as a small-scale cut-off and the molecular structure of the bilayer is not taken into account explicitly.

Recently, models appeared which bridge the gap between these two types of models, i.e., between discrete models with atomic resolution on the one side and flexible surface models

on the other side. These new models describe the membrane behaviour on intermediate length scale. The first and simplest model has been proposed by Smit [33]. He represented a lipid by two particles, a hydrophilic one and a hydrophobic one, which are connected via a harmonic spring. The surrounding solvent is represented by particles identical to the head particles. All these particles interact via a Lennard-Jones potential. Smit demonstrated in molecular dynamics simulations that the interfacial tension could be reduced by the addition of amphiphilic compounds. The resolution of this model helps to investigate membrane properties at two different levels: the simplicity of the model allows large numbers of molecules to investigate bulk properties of the membrane, while the separate representation of each molecule helps to investigate surface and even intra-membrane properties. A number of models have appeared since, using the same ideas, but with different approximations of the atomic representation and particle interactions [34, 35, 36]. The main idea in all of them is that each surfactant molecule consists of a small hydrophilic part, called ”head”, and a large hydrophobic part, called ”tail”. The number of ”head” and ”tail” particles varies across models, each particle representing a few up to a dozen atoms. The particles are connected by bonds in different ways, depending on the topology of the molecule. The bending stiffness of chains is incorporated by using a bending potential between 3 neighbouring particles, a dihedral potential incorporated between 4 neighbouring particles is responsible for 3D stiffness of the chain. Binary soft-core potentials are involved in interactions between all types of particles. The big advantage of these models is the possibility to obtain ”exact” predictions of membrane bulk properties by providing the interactions between molecules. The predictions are ”exact” in the sense that they can be made as accurate as we like, subject to the limitations imposed by the computer budget. All molecular dynamic simulations in this work are based on the models of Goetz and Lipowsky and Marrink et. al.

## 1.5 Thesis outline

In chapter 2 we establish methods to determine both the shear viscosity and inter-monolayer friction coefficient of bilayers from sheared molecular dynamics simulations. By applying a shear perpendicular to the bilayer, i.e. the vorticity lies parallel to the bilayer, we find a linear velocity profile for the amphiphiles, from which we deduced the in-plane viscosity.

The friction between the upper monolayer and the lower monolayer as they slide along one another, as determined by applying a shear field parallel to the bilayer, was linear in the velocity difference between the two monolayers. For very high shear rates the bilayer became instable and disintegrated.

In chapters 3 and 4 we present simulations of the dynamics of stationary bilayers. Molecular dynamics simulations of a coarse-grained bilayer model have been used to obtaine the time correlation functions of the thermal undulations and density fluctuations of a lipid membrane. We observe a double-exponential decay, with relaxation rates in good agreement with the theory by Seifert and Langer [37]. Intermonolayer friction resulting from local velocity differences between the two monolayers is shown to be the dominant dissipative mechanism for fluctuations with wave lengths below $\sim 0.1\mu$m.

In chapter 5 molecular dynamic simulations show the impact of pair friction and different architectures of lipids on the dynamical parameters of a lipid bilayer, such as the surface viscosity and the intermonolayer friction.

In chapter 6 a coarse-grained model is studied for the simulation of a wormlike micelle. We demonstrate that our worm is inherently stable. The worms are observed to buckle under sufficiently strong compression forces. The persistence length and bending rigidity follow from analysing the thermal undulations of a tensionless worm. System size dependencies of the elastic modulus of the worm, are eliminated by explicitly calculating the arc length of the worm.

At the end of the thesis, the results are summarized in both English and Dutch.

# Bibliography

[1] R. Kwok and E. Evans. Thermoelasticity of large lecithin bilayer vesicles. *Biophys. J.*, 35:637–652, 1981.

[2] E. Evans and D. Needham. Physical properties of surfactant bilayer membranes; thermal transitions, elasticity, rigidity, cohesion, and colloidal interactions. *J. Phys. Chem.*, 91:4219–4228, 1987.

[3] C. A. Rutkowski, L. M. Williams, T. H. Haines, and H. Z. Cummins. The elasticity of synthetic phospholipid vesicles obtained by photon correlation spectroscopy. *Biochemistry.*, 30:5688–5696, 1991.

[4] F. R. Hallet, J. Marsh, B. G. Nickle, and J. M. Wood. Mechanical properties of vesicles. ii. a model for osmotic swelling and lysis. *Biophys. J.*, 64:435–442, 1993.

[5] B. L.-S. Mui, P. R. Cullis, E. A. Evans, and T. D. Madden. Osmotic properties of large unilamellar vesicles prepared by extrusion. *Biophys. J.*, 64:443–453, 1993.

[6] B. W. Koenig, H. H. Strey, and K. Gawrisch. Membrane lateral compressibility determined by nmr and x-ray diffraction: effect of acyl chain polyunsaturation. *Biophys. J.*, 73:1954–1966, 1997.

[7] M. D. Schneider, J. T. Jenkins, and W. W. Webb. Thermal fluctuations of large quasi-spherical biomolecular phospholipid vesicles. *J. Phys.*, 45:1457–1472, 1984.

[8] H.-P. Duwe, H. Englehardt, A. Zilker, and E. Sackmann. Curvature elasticity of smectic a lipid bilayers and cell plasma membranes. *Mol. Cryst. Liq. Cryst.*, 152:1–7, 1987.

[9] J. F. Faucon, M. D. Mitov, P. Meleard, I. Bivas, and P. Botherol. Bending elasticity and thermal fluctuations of lipid membranes; theoretical and experimental requirements. *J. Phys*, 50:2389–2414, 1989.

[10] L. Bo and R. E. Waugh. Determination of bilayer membrane bending stiffness by tether formation from giant, thin-walled vesicles. *BioPhys. J.*, 55:509–517, 1989.

[11] E. Evans and A. Yeung. Hidden dynamics in rapid changes of bilayer shape. *Chem. Phys. Lipids*, 73:39–56, 1994.

[12] E. Evans, H. Bowman, A. Leung, D. Needham, and D. Tirrell. Biomembrane templates for nanoscale conduits and networks. *Science*, 273:933–935, 1996.

[13] E. Evans and W. Rawicz. Entropy-driven tension and bending elasticity in condensed-fluid membranes. *Phys. Rev. Lett.*, 64:2094–2097, 1990.

[14] W. Rawicz, K. C. Olbrich, T. McIntosh, D. Needham, and E. Evans. Effect of chain length and unsaturation on elasticity of lipid bilayers. *Biophys. J.*, 79:328–339, 2000.

[15] W. Pfeiffer, S. König, J. F. Legrand, T. Bayerl, D. Richter, and E. Sackmann. Neutron spin echo study of membrane undulations in lipid multibilayers. *Europhys. Lett.*, 23:457–462, 1993.

[16] T. Pott and Méléard. The dynamics of vesicle thermal fluctuations is controlled by intermonolayer friction. *Europhys. Lett.*, 59:87–93, 2002.

[17] R. M. Raphael and R. E. Waugh. Accelerated interleaflet transport of phosphatidylcholine molecules in membranes under deformation. *BioPhys. J.*, 71:1374–1388, 1996.

[18] R. Dimova, C. Dietrich, A. Hadjiisky, K. Danov, and B. Pouligny. Falling ball viscosimetry of giant vesicle membranes: Finite-size effects. *Eur. Phys. J. B*, 12:589–598, 1999.

[19] R. Dimova, B. Pouligny, and C. Dietrich. Pretransitional effects in dimyristoylphosphatidylcholine vesicle membranes: Optical dynamometry study. *Biophys. J.*, 79:340–356, 2000.

[20] L. Verlet. Computer "experiments" on classical fluids. i. thermodynamical properties of lennard-jones molecules. *Phys. Rev.*, 159:98–103, 1967.

[21] L. Verlet. Computer "experiments" on classical fluids. ii. equilibrium correlation functions. *Phys. Rev.*, 165:201–214, 1967.

[22] E. Egberts and H. J. C. Berendsen. Molecular dynamics simulation of a smectic liquid crystal with atomic detail. *J. Chem. Phys.*, 89(6):3718–3732, 1988.

[23] H. E. Alper, D. Bassolino, and T. R. Stouch. Computer simulation of a phospholipid monolayer-water system: The influence of long range forces on water structure and dynamics. *J. Chem. Phys.*, 98(12):9798–9807, 1993.

[24] H. Heller, M. Schaefer, and K. Schulten. Molecular dynamics simulation of a bilayer of 200 lipids in the gel and in the liquid crystal phase. *J. Chem. Phys.*, 97(31):8343 – 8360, 1993.

[25] Stouch and Terry R. Molecular dynamics simulation of a bilayer of 200 lipids in the gel and in the liquid crystal phase. *Mol. Simul.*, 10(2-6):335–362, 1993.

[26] B. Widom. Lattice-gas model of amphlphiles and of their orientation at interfaces. *J. Phys. Chem.*, 88:6508–6514, 1984.

[27] B. Widom. Lattice model of microemulsions. *J. Chem. Phys.*, 84(12):6943–6954, 1986.

[28] B. Widom. Correlation and scattering functions in a lattice model of oil-water-amphiphile solutions. *J. Chem. Phys.*, 90(4):2437–2443, 1989.

[29] K. A. Dawson. Interfaces between phases in a lattice model of microemulsions. *Phys. Rev. A*, 35:1766–1773, 1987.

[30] M. M. Telo da Gama and K. E. Gubbins. Adsorption and orientation of amphiphilic molecules at a liquid-liquid interface. *Mol. Phys.*, 59(2):227–239, 1986.

[31] M. M. Telo da Gama. Phase equilibria and interfacial properties of model ternary mixtures. *Mol. Phys.*, 62(3):585–604, 1987.

[32] R. Lipowsky and E. Sackmann. *Structure and dynamics of membrane.*, volume 1. Elsevier, Amsterdam, 1995.

[33] B. Smit. Molecular-dynamics simulations of amphiphilic molecules at a liquid-liquid interface. *Phys. Rev. A*, 37(9):3431–3433, 1988.

[34] R. Goetz and R. Lipowsky. Computer simulations of bilayer membranes: Self-assembly and interfacial tension. *J. Chem. Phys.*, 108:7397–7409, 1998.

[35] R. Goetz, G. Gompper, and R. Lipowsky. Mobility and elasticity of self-assembled membranes. *Phys. Rev. Lett.*, 82:221–224, 1999.

[36] S. J. Marrink, A. H. de Vries, and A. E. Mark. Coarse grained model for semiquantitative lipid simulations. *J. Phys. Chem. B*, 108:750–760, 2004.

[37] U. Seifert and S. A. Langer. Viscous modes of fluid bilayer membranes. *Europhys. Lett.*, 23:71–76, 1993.

# 2 Surface Viscosity, diffusion, and intermonolayer friction: simulating sheared amphiphilic bilayers

*The flow properties of an amphiphilic bilayer are studied in molecular dynamics simulations, by exposing a coarse grained model bilayer to two shear flows directed along the bilayer surface. The first field, with a vorticity perpendicular to the bilayer, induces a regular shear deformation, allowing a direct calculation of the surface viscosity. In experiments this property is measured indirectly, by relating it to the diffusion coefficient of a tracer particle through the Saffman-Einstein expression. The current calculations provide an independent test of this relation. The second flow field, with a vorticity parallel to the bilayer, causes the two constituent monolayers to slide past one another, yielding the interlayer friction coefficient.* *

## 2.1 Introduction

Amphiphilic bilayers and biological membranes are planar self-assembled aggregates of amphiphilic molecules, such as surfactants or lipids, in which a hydrophilic head group is covalently bound to a hydrophobic tail. These structures are locally flat, but smoothly undulating on a length scale well beyond their thickness [2, 3]. Because bilayers are held together by relatively weak non-bonded interaction forces, they behave in many respects as two dimensional liquids suspended in a three dimensional solvent matrix. This makes bilayers very susceptible to external forces, which give rise to deformations of the overall shape of the bi-

∗ The work described in this chapter previously appeared in Biophysical Journal **89**, 823 (2005) [1].

layer and to flow within the bilayer. Examples hereof include the elongation and rupture of vesicles sucked into a pipet [4, 5], the shear induced transition of a stack of bilayers into an onion like structure [6, 7, 8, 9], the large changes in shape of red blood cells as they creep through narrow passageways [10], the resilience of a cell when prodded by a needle, and the pulling of tethers from a vesicle by a localised force [11, 12, 13, 14, 15, 16]. In this paper we will concentrate on deformations that preserve the overall shape of the bilayer.

A flat or weakly undulating bilayer oriented parallel to the *xy* plane, see Fig. 6.1, can be exposed to two distinct flow deformations, as illustrated in Fig. 2.2. The first flow field, $\mathbf{v}(\mathbf{x}) = (\dot{\gamma}y, 0, 0)$, describes the linear velocity profile of a regular shear flow with a shear rate $\dot{\gamma}$. Following the convention in the literature on sheared block-copolymers [17], this flow is referred to as a perpendicular shear flow. The resistance of the bilayer against this flow is characterised by a two dimensional surface viscosity, $\eta_s$, which, analogous to the regular three dimensional viscosity, relates the shear force per unit of length of bilayer to the shear rate. Note that both leaflets of the bilayer move in unison under this field. In the so-called parallel flow field, $\mathbf{v}(\mathbf{x}) = (\dot{\gamma}z, 0, 0)$, on the other hand, the two monolayers of the bilayer are sliding past one another as two flat rigid objects with velocities $\pm\Delta v\hat{\mathbf{e}}_x$. A friction coefficient, $\xi$, is defined by the ratio between the sliding force per unit of bilayer area and the velocity difference between the two leaflets.

The viscosity and friction coefficient are not easily accessible under experimental conditions. Forced deformations of a bilayer frequently culminate in the simultaneous occurrence of both flow fields, and are often accompanied by bending and stretching of the bilayer. Non-uniform stress distributions resulting in diffusion-like stress relaxation processes, both within and between ('flip-flops') the monolayers, further complicate the interpretation of the experimental data. For an extensive discussion of these processes, we refer the reader to Evans and co-workers [12, 13].

Viscosity measurements by pulling a tether from a vesicle, for instance, are hampered by the above effects. It proves more convenient, therefore, to deduce the viscosity from the translational and rotational diffusion coefficients of fluorescent transmembrane tracer particles in a quiescent bilayer, see reference [15] and references cited therein, using a Stokes-Einstein type expression derived for this particular system by Saffman [18]. Saffman elegantly solved Stokes' equations of the creeping flow around a cylinder (*i. e.* the tracer) moving in a thin

sheet of viscous liquid (*i. e.* the bilayer), by emphasising the role played by the liquid, of viscosity $\eta_w$, on either side of this sheet. Falling ball viscosimetry [19], in which a microsphere moving under gravity is constrained to a bilayer vesicle, is essentially based on the same theory. An independent validation of the Saffman-Einstein expression for use with bilayers is therefore welcomed.

Friction coefficients have been measured by pulling a thin tether from a vesicle [11, 12, 13, 14], where the sharp change in curvature at the vesicle-tether junction induces a velocity difference between the inner and outer layers. A second method focuses on the slip occurring when amphiphiles flow through an hour glass shaped fusion pore from a bilayer under low surface tension to a bilayer under a higher tension [20]. The wide range of the few reported friction coefficients illustrates the complexity of (the interpretation of) these ingenious measurements, and the sensitivity to the amphiphiles used in the experiment.

The objective of this paper is to establish methods to determine both the shear viscosity and the friction coefficient of a bilayer by means of computer simulations on the molecular level. Bilayers have been the subject of numerous modelling studies, which for the most part focused on the equilibrium properties and on the self-assembly from a disordered amphiphilic solution [21, 22, 23, 24, 25, 26]. To the best of our knowledge, the flow behaviour of a bilayer has never been simulated at this level. Since our aim here is to develop and validate new techniques, we opted for a relatively simple and fast coarse grained amphiphilic model known to reproduce realistic thermodynamic properties [27, 28, 29, 30, 31]. No claims are made to the applicability of the model to calculate realistic values of dynamical properties. Our aim is to develop methods and to test the applicability of the Saffman-Einstein equation. The model and other simulation details are summarised in Section 6.3. Results are presented in Section 6.4, where we describe the response of the bilayer, and of the individual amphiphiles, to the applied flow fields. We end with a discussion of the applied methods, and a comparison with the available experimental data, in Section 2.4.

## 2.2 Setup

The speed of coarse grained (CG) simulation models makes these models very attractive for simulations requiring large length and time scales, where fully atomistic models are compu-

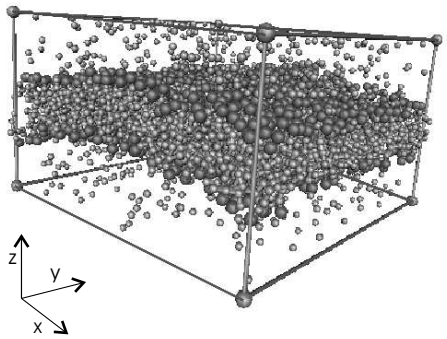


Figure 2.1: A snapshot of the bilayer-liquid simulation box. The number of surrounding solvent particles has been reduced for clarity.

tationally too demanding, and to put new simulation techniques to the test, as is the case here. In coarse grained models, a number of atoms is grouped together to form a CG particle. The equation of motion of the CG particle follows, in principle, by averaging over the dynamics of the constituent atoms [32]. The resulting Langevin equation combines conservative forces with friction and random forces [33]. The conservative forces are responsible for the thermodynamic properties of the CG model, and therefore deservedly lie at the heart of the currently available fitting procedures [25, 26, 28]. In case one restricts attention to structural and thermodynamic properties, the precise values of the friction and random forces are irrelevant. Of course, as soon as one wants to calculate realistic dynamical properties, the precise nature of these forces matters a lot. Unfortunately it is still not fully understood how to calculate friction and random forces from atomistic simulations [32, 34]. As was already mentioned in Section 2.1, however, our aim is primarily to develop and test methods to study the flow properties of a bilayer. We therefore decided to use a simplified CG model, in which friction and random forces are neglected altogether.

The simulation model we used was developed by Goetz and Lipowsky [27, 28]. They chose for an amphiphilic architecture in which the head is represented by a single bead ($h$)

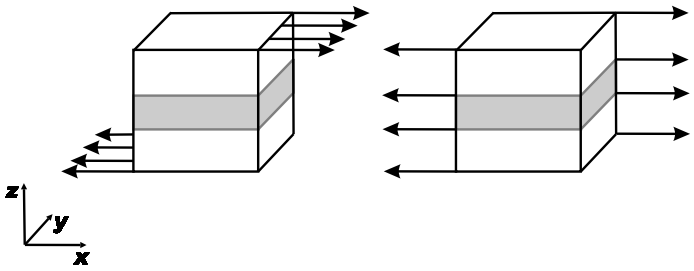


Figure 2.2: Side views of the simulated system, highlighting parallel (left) and perpendicular (right) shear flows.

and the tail is reduced to four beads ($t$) representing roughly three $CH_2$ units each. The solvent consists of loose water beads ($w$), corresponding with two water molecules. Interactions between like particles, as well as the hydrophilic head-water interactions, are modeled by a Lennard-Jones potential, $\Phi_{\mathrm{LJ}}(r) = 4\varepsilon[(r/\sigma)^{-12} - (r/\sigma)^{-6}]$, with $\varepsilon = 2\,\mathrm{kJ/mol}$ and $\sigma = 1/3\,\mathrm{nm}$. The hydrophobic tail-water and tail-head interactions are modeled by a purely repulsive potential, $\Phi_{\mathrm{rep}}(r) = \varepsilon[r/(1.05\sigma)]^{-9}$. The non-bonded forces are implemented in a shifted-force fashion, ensuring a smooth truncation of the energy and the force at the cut-off distance of $2.5\,\sigma$. The particles of the amphiphilic molecules are held together by harmonic bond potentials, $\Phi_{\mathrm{bond}}(l) = 5000\varepsilon\sigma^{-2}(l-\sigma)^2$. An angle potential between every set of three consecutively bonded particles, $\Phi_{\mathrm{angle}}(\phi) = 2\varepsilon[1-\cos(\phi)]$, introduces a bending stiffness. There are no dihedral potentials. All particles have the same mass $m$ of 36 a.u., and the number density is 2 particles per $3\sigma^3$. In all our simulations the temperature $T$ was 325 K, or $1.35\,\varepsilon/k_B$ with $k_B$ Boltzmann's constant, and was maintained by means of a Nosé-Hoover thermostat. The time step used in the Verlet leapfrog scheme was $\tau/500$, where $\tau = \sqrt{m\sigma^2/\varepsilon}$ is the unit of time. Previous simulations with this CG model showed that its equilibrium area, elastic modulus, bending rigidity and line tension coefficient compare favourably with experimental data [27, 28, 29, 30, 31]. All simulations were run using the DL_POLY_2.0 package [35], tailored to the specifications of the problem.

Rectangular periodic simulation boxes were used, each having a square ground plane of sides $L_{\parallel}$ parallel to the bilayer and the $xy$ plane, and a height $L_{\perp}$ perpendicular to these.

Initial bilayer-solvent configurations were created by constructing two parallel square lattice layers of straight amphiphilic molecules, 1152 in total, with their heads pointing outward. The 10 800 solvent particles were placed at random in the box, taking care to avoid overlap with the bilayer and with previously inserted solvent particles. The boxes were then energy minimized for a limited number of steps, followed by equilibration runs at the desired temperature. A snapshot of the resulting bilayer box is shown in Fig. 6.1. On varying $L_\parallel$ it was found that at $L_\parallel = 34.9\sigma$ the bilayer is in the tensionless state, in which the average pressures parallel and perpendicular to the bilayer are identical, to wit, about $1.5\,\varepsilon\sigma^{-3}$ or 1.4 kbar. The structure factors $S$ of the thermal undulations followed the theoretical prediction for the tensionless state, $S(\mathbf{q}) \propto \mathbf{q}^{-4}$, with $\mathbf{q}$ a wave vector commensurate with the box dimension $L_\parallel$ [2, 3, 27]. The box height of $20.4\,\sigma$ allows the solvent enough freedom to reach an isotropic pressure in the middle between two periodic images of the bilayer [28].

Simulations under shear rate $\dot{\gamma}$ were run using Lees-Edwards boundary conditions [36, 37], such that the flow was directed along the $x$ axis, *i. e.* such that $\mathbf{v}(\mathbf{x}) = v(\mathbf{x})\hat{\mathbf{e}}_x$. For homogeneous solvent boxes the shear direction is of course irrelevant, but this is no longer the case for boxes with a bilayer. A perpendicular flow was generated such that $v_\perp(\mathbf{x} + L_\parallel\hat{\mathbf{e}}_y) = v_\perp(\mathbf{x}) + \dot{\gamma}L_\parallel$ and a parallel flow such that $v_\parallel(\mathbf{x} + L_\perp\hat{\mathbf{e}}_z) = v_\parallel(\mathbf{x}) + \dot{\gamma}L_\perp$. Analogous flow fields along the $y$ axis produce identical results. The Nosé-Hoover thermostat [36] was adapted for these shear conditions, by calculating the temperature from the velocity distribution relative to the local flow field and by rescaling only superficial velocities. In these calculations the flow fields were assumed to be given by appropriate linear expressions, although some runs yielded a distinctly non-linear profile. Using the actual flow field in the thermostatting routine did not significantly change the results. The structure factors $S(\mathbf{q})$ of the thermal undulations of the bilayer still scaled as $\mathbf{q}^{-4}$ under shear, suggesting that the flow does not induce any significant tension on the bilayer. After turning on the shear flow, the simulations were continued till all transient effects had died out and a steady laminar flow field had formed, before starting the production runs.

Three techniques were used to determine the overall shear viscosities of the simulated systems [36]. In the non-sheared runs, the viscosity $\eta_{\text{tot}}$ was calculated using the Green-Kubo relation

$$\eta_{\text{tot}} = \frac{V}{k_B T}\int_0^\infty \langle P_{\alpha\beta}(t)P_{\alpha\beta}(0)\rangle\, dt, \tag{2.1}$$

where $P_{\alpha\beta}$ is an off-diagonal ($\alpha \neq \beta$) element of the pressure tensor, $V$ is the volume of the box, and the angular brackets denote a canonical average. For a sheared system the viscosity is defined as the ratio between the total shear force per unit area and the shear rate,

$$\eta_{\text{tot}} \equiv \frac{F_{\text{shear}}/A}{\dot{\gamma}} = \frac{\langle P_{\alpha\beta} \rangle}{\dot{\gamma}}. \tag{2.2}$$

For systems containing a bilayer we use $\alpha = x$ and $\beta = y$ or $z$ for the perpendicular and parallel shear flows, respectively. The third method is based on the realization that the rate of energy production, $\eta_{\text{tot}} \dot{\gamma}^2 V$, by the shearing boundaries is easily calculated as the time derivative, $\dot{E}$, of the extended Hamiltonian of the system plus thermostat, to arrive at

$$\eta_{\text{tot}} = \frac{\dot{E}}{\dot{\gamma}^2 V}. \tag{2.3}$$

Notice that in the stationary state the energy of the system is constant and therefore $\dot{E}$ is equal to the rate of energy extraction from the system by the thermostat. A similar approach was recently proposed by Holian [38]. The conversion from total shear viscosities into the viscosity and friction coefficient of the bilayer will be discussed at the appropriate places in the next section.

## 2.3 Results

We start with the viscosity of the solvent. Two boxes were filled randomly with 2250 and 66 667 solvent particles, respectively. For both boxes and for all three calculation methods mentioned in the previous section, we found a viscosity $\eta_{\text{w}}$ of just over $1.0\,\varepsilon^{1/2} m^{1/2} \sigma^{-2}$, virtually independent of the applied shear rate $\dot{\gamma}$ ranging from zero to $0.2\,\tau^{-1}$. This value translates into $1.3 \cdot 10^{-4}$ Pa s, which amounts to about a quarter of the experimental viscosity of $5 \cdot 10^{-4}$ Pa s for water at this temperature. The diffusion coefficient of the solvent particles was found to be $0.1\sigma^2/\tau$, or $1 \cdot 10^{-8}$ m$^2$/s, which is about four times larger than the experimental self-diffusion coefficient, $2.5 \cdot 10^{-9}$ m$^2$/s, of a water molecule at this temperature.

Using the same approaches, the viscosity of a homogeneous liquid of chains of five particles, $t_5$, was found to be $\eta_{\text{b}} \approx 2.1 \varepsilon^{1/2} m^{1/2} \sigma^{-2}$, twice the value obtained for the solvent, again independent of the shear rate. For comparison, the experimental viscosity of a comparable liquid of hydrocarbon chains, *n*-hexadecane, is about eight times higher [39]. These results

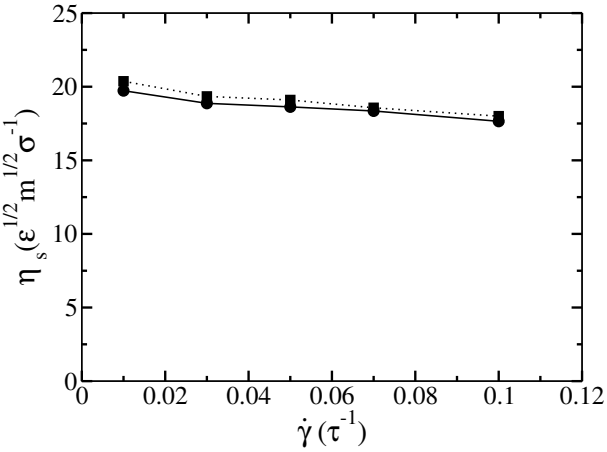


Figure 2.3: The surface viscosity of the bilayer, derived from simulations with a perpendicular shear flow, plotted against the applied shear rate. The data points were obtained by calculating the total shear force on the system, i.e. the first term on the right hand of Eq. 5, from the pressure (solid circle) or from the thermostat (solid square).

indicate that the model is not well suited to aim for dynamical properties in quantitative agreement with experiments. Marrink *et al.* [26], following Groot and Rabone [23], addressed the spurious speed-up of their coarse grained model by introducing an ad hoc scaling factor of four to relate the elapsed simulation time to the real time. An alternative physically sound route to solve the dynamical discrepancy is to maintain the friction and random forces in the equations of motion of the coarse grained particles. In case these forces grow large relative to the inertial forces, one is of course better off running Brownian dynamics.

### 2.3.1 Perpendicular shear

Of the two interesting shear directions of a box containing a bilayer, the perpendicularly sheared system will be discussed first. The total viscosity of the system has been calculated for the quiescent box, as well as for those with shear rates ranging from 0.001 to 0.1 $\tau^{-1}$, to be about 1.6 $\varepsilon^{1/2} m^{1/2} \sigma^{-2}$ in each case. In the steady state, the velocity distribution of the amphiphilic particles closely follows a linear flow field. This suggests that the bilayer behaves

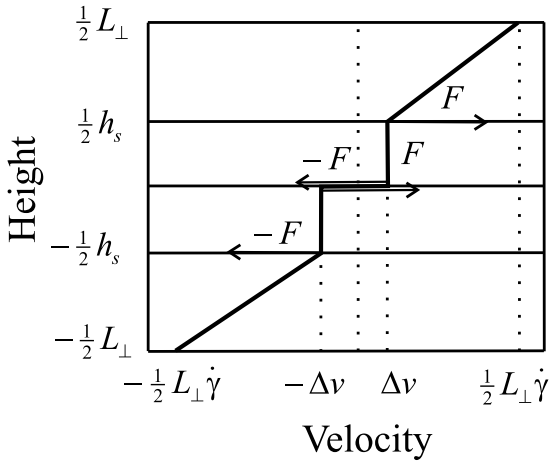


Figure 2.4: Sketch of the velocity profile (line) and of the forces (arrows) for a bilayer system under parallel shear.

like a regular sheared liquid (be it one in which the molecules are bound to a plane), which is a prerequisite for a well-defined bilayer surface viscosity. Analogous to Eq. (2.2), the surface viscosity is defined as the total shear force on the bilayer per unit of length, divided by the shear rate,

$$\eta_\mathrm{s} \equiv \frac{F_\mathrm{bilayer}/L_\parallel}{\dot{\gamma}}, \tag{2.4}$$

$$F_\mathrm{bilayer} = \langle P_{xy}\rangle L_\parallel L_\perp - \eta_\mathrm{w}\dot{\gamma}L_\parallel\left(L_\perp - h_\mathrm{s}\right). \tag{2.5}$$

The last equation defines the shear force on the bilayer, $F_\mathrm{bilayer}$, as the total shear force across the $xy$ plane minus the contribution acting on the solvent, where $h_\mathrm{s} \approx 6.8\sigma$ is the thickness of the bilayer. The shear viscosity of the bilayer was found to be about $20\,\varepsilon^{1/2}m^{1/2}\sigma^{-1}$, or $8.5\cdot10^{-13}$ Pa m s. Figure 2.3 reveals a weak dependence of this value on the shear rate, with a reduction by about 10% over the entire range covered.

### 2.3.2 Parallel shear

Under a parallel shear field the total viscosity of the box was about $1.4\,\varepsilon^{1/2}m^{1/2}\sigma^{-2}$, for shear rates ranging from 0.002 to $0.05\,\tau^{-1}$. A similar value was obtained by applying the Green-Kubo relation to the quiescent box. As in the previous section, we now have to convert this

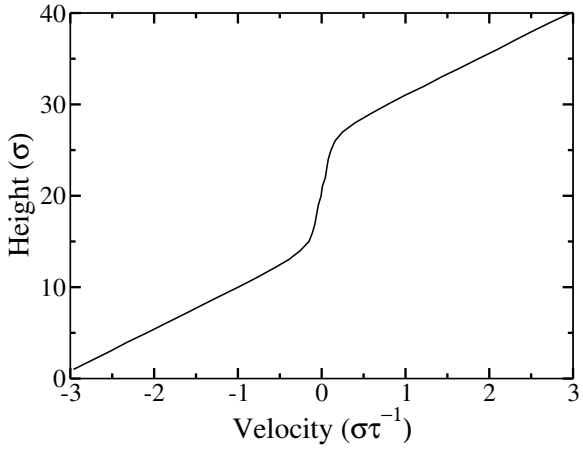


Figure 2.5: Velocity profile of a bilayer system at a parallel shear rate of 0.03 $\tau^{-1}$.

number into a property of the bilayer.

Because of the orientation of the bilayer relative to the sheared boundaries, we expect a velocity profile like the one drawn in Fig. 2.4. The profile in the solvent will be linear, with a slope $\dot{\gamma}_w$ different from the imposed shear rate $\dot{\gamma}$. In the middle of the box the two leaflets of the monolayer are sliding past one another, like two flat solid objects, with velocities $\pm\Delta v\hat{\mathbf{e}}_x$, giving rise to a friction force between the two leaflets. The friction coefficient of this motion follows from the shearing force $F$ exerted on the top (bottom) monolayer, by the solvent above (below) the bilayer, according to

$$\xi \equiv \frac{2F/L_{\parallel}^2}{2\Delta v}. \tag{2.6}$$

All that remains is to determine the two unknowns featuring on the right hand side of the above expression.

The actually calculated velocity profile, see Fig. 2.5, shows that the velocity gradient within the bilayer region is considerably smaller than in the solvent, but not zero. This is caused by a convolution of the idealised profile with the thermal undulations of the bilayer. Unfortunately, this renders direct estimates of $\Delta v$ from the velocity profiles highly inaccurate. The shear rate of the solvent at some distance from the bilayer, however, is not affected by

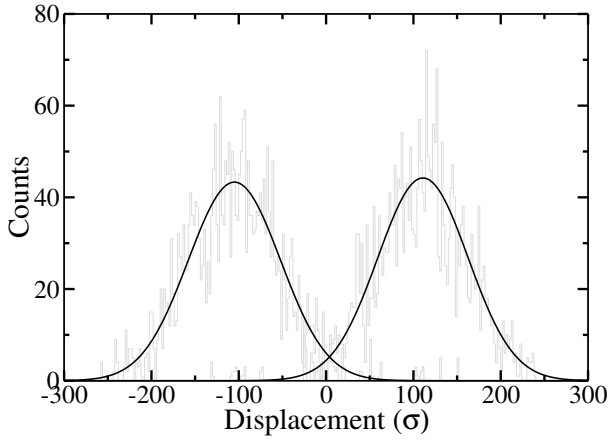


Figure 2.6: Probability distributions of displacements, along the flow direction, of head particles in the top (right peak) and bottom (left peak) monolayers. At a shear rate of $0.03\,\tau^{-1}$, the amphiphiles cover a distance of nearly three box lengths over a period of about $18\,000\,\tau$. The solid lines are Gaussian fits.

these undulations. Under the assumption of stick boundary conditions at the bilayer-solvent interface, we can calculate the slip velocity from

$$2\Delta v = \dot{\gamma} L_\perp - \dot{\gamma}_w (L_\perp - h_\mathrm{s}). \tag{2.7}$$

This velocity turns out to be proportional to the overall shear rate.

Alternatively, one could look at the distances travelled by the amphiphilic particles, along the flow direction, over the course of a simulation. This distribution is shown in Fig. 2.6 for the head particles of the two monolayers, excluding a few that flipped from one monolayer to the other. Because of the covalent bonding, the distributions for the tail particles are virtually identical. From the location of the peak, divided by the length of the simulation, we again obtain $\Delta v$. The numerical values obtained by both methods agree very well, implying stick boundary conditions at the two bilayer-solvent interfaces. Consequently, the force exerted on the top monolayer by the solvent above the bilayer can be calculated from the shear rate in the solvent, $F = \dot{\gamma}_w \eta_\mathrm{w} L_\parallel^2$. Inserting these results in Eq. (2.6), we find a friction coefficient $\xi = 3.7 \varepsilon^{1/2} m^{1/2} \sigma^{-3}$, or $1.4 \cdot 10^6\,\mathrm{N\,s\,m^{-3}}$. As shown in Fig. 2.7, this value is effectively

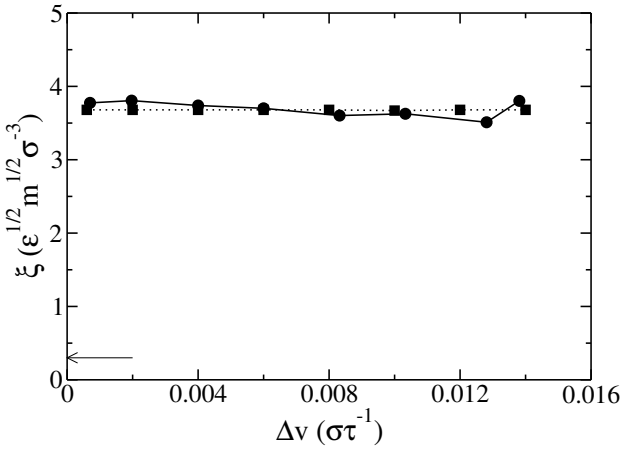


Figure 2.7: The friction coefficient of sliding monolayers, as a function of the slip velocity. Slip velocities were calculated from Eq. (2.7) (squares) and from the average displacements in Fig. 2.6 (circles). The arrow denotes the effective friction coefficient $\xi'$ of a slab of $t_5$ molecules with the same thickness as the bilayer (see text for details).

independent of the slip velocity.

We end this section with a discussion of structural properties of a bilayer under a parallel shear deformation. Figure 2.8 shows the distribution of longitudinal angles $\phi$ of the end-to-end vectors $\mathbf{r}_{15}$ of the amphiphiles, *i. e.*, the orientation of the molecule in the plane of the bilayer. In the quiescent box this distribution is homogeneous, as expected for a bilayer in the liquid-crystalline or fluid $L_\alpha$ phase. The sheared system, on the other hand, reveals maxima at $\phi = 0$ and $\pi$ rad, indicative of a propensity to tilt along the shear direction. A distribution of the tilt angles, defined as the angle $\theta$ between the $z$ axis and the projection of $\mathbf{r}_{15}$ on the $xz$ plane, is presented in Fig. 2.9. The two peaks of the distribution, corresponding to the upper and lower monolayer, lie at 0 and $\pi$ rad in the quiescent box, and shift by $\Delta\theta$ under shear. This average tilt is proportional to the slip velocity and the overall shear rate. The length distribution of the end-to-end vectors is not affected by the shear flow.

It is interesting to note that for overall parallel shear rates beyond $0.05\,\tau^{-1}$, which corresponds to a slip velocity of about $11{\cdot}10^{-3}\sigma/\tau$, the bilayer becomes unstable. We observed

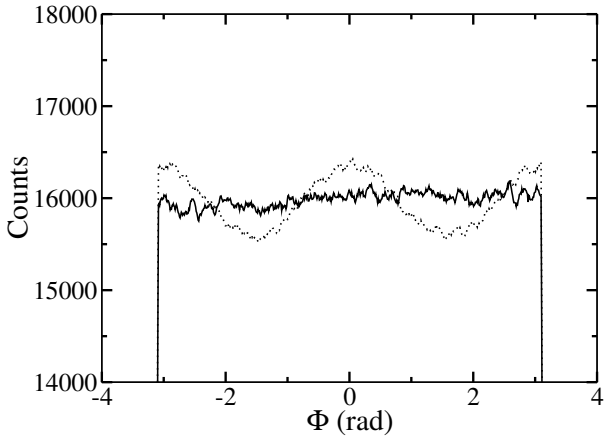


Figure 2.8: Histogram of the orientation of amphiphilic molecules in the plane of the bilayer. The solid line refers to a quiescent system, the dotted line to a parallel shear rate of $0.05\tau^{-1}$.

pronounced undulations of the bilayer, amphiphiles piling up to form buds, and the creation of transmembrane pores. Eventually the bilayer is torn apart. A further discussion of these phenomena will be presented elsewhere.

## 2.4 Discussion and Conclusions

The results of the preceding section show that non-equilibrium coarse grained simulations can be used to study the flow characteristics of an amphiphilic bilayer, to wit, the bilayer viscosity $\eta_s$ for co-planar shear deformations and the friction coefficient $\xi$ between sliding monolayers. Both are obtained by placing the simulation box under a shear flow, with vorticity oriented perpendicular and parallel to the bilayer, respectively. The shear force acting on the bilayer is then easily obtained by subtracting the shear force on the solvent from the total shear force.

The common experimental method to obtain a surface viscosity is to measure the diffusion coefficient $D$ of a tracer particle, a cylinder of radius $a$ with a length equal to the bilayer thickness $h_s$. Assuming the bulk viscosity $\eta_w$ of the surrounding solvent is much smaller (but

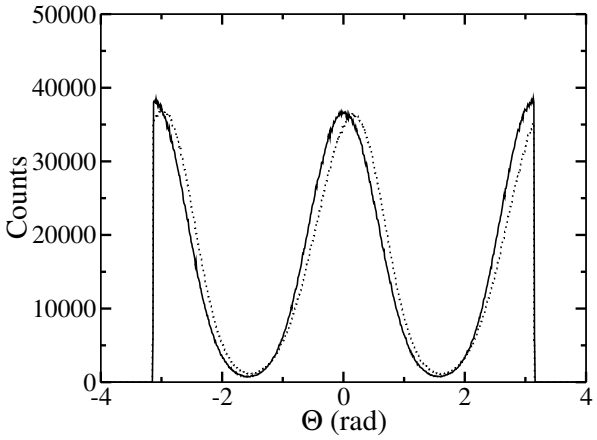


Figure 2.9: Probability distribution of the tilt of the amphiphiles in the flow direction. The solid line refers to a quiescent system, the dotted line to a parallel shear rate of $0.05\tau^{-1}$.

not zero) than that of the bilayer, Saffman [18] derived that

$$D = \frac{k_B T}{4\pi\eta_s}\left[\ln\left(\frac{\eta_s}{a\eta_w}\right) - \gamma\right], \tag{2.8}$$

where $k_B$ is Boltzmann's constant and $\gamma \approx 0.577$ is Euler's constant. In case $\eta_s/h_s \ll \eta_w$, this equation also holds when the tracer particle sticks out of the bilayer. Assuming that Eq. (2.8) may be used even at the molecular level, we set $a$ equal to $\sigma$ and find $D = 1.3 \cdot 10^{-2}\sigma^2/\tau$. Both from a direct calculation of the mean square displacements of the amphiphiles in a quiescent bilayer, as well as from the spreading of the distributions in Fig. 2.6, we find $D = 1.8 \cdot 10^{-2}\sigma^2/\tau$. Using half the surface viscosity in Eq. (2.8), because the diffusing amphiphiles span only half the bilayer [15], we get the same result. This agreement must be considered to be a bit fortuitous, of course. First, we have assumed that the radius of the flexible amphiphile is equal to $\sigma$, and thus includes the first "solvation shell". Second, the diffusion coefficient calculated from the Saffman equation is relatively insensitive to the surface viscosity, as illustrated by the two calculated values of $D$.

It is tempting to relate the viscosity $\eta_s$ of the bilayer to the viscosity $\eta_b$ of a bulk liquid of like molecules, in this case chains of five tail particles, $t_5$. This connection appears fre-

quently in the literature [13, 20], and is given by $\eta_s' = \eta_b h_s$. Inserting numerical values yields $\eta_s' = 14\varepsilon^{1/2} m^{1/2} \sigma^{-1}$, which amounts to just over two thirds of the actual value of $\eta_s$. This difference is due to the lower degree of ordering in the liquid relative to the bilayer, where the amphiphiles are stretched, aligned and positioned in a near-planar configuration, and to the higher packing density in the bilayer made possible by this ordering. The effective friction coefficient of a slab of $t_5$ with the same thickness as the bilayer is readily shown to be given by $\xi' = \eta_b / h_s$ [13, 20]. The resulting value of $\xi' = 0.3\varepsilon^{1/2} m^{1/2} \sigma^{-3}$, indicated in Fig. 2.7 by an arrow, amounts to less than one tenth of the actual bilayer friction coefficient. Here again, the increased ordering in the bilayer relative to the liquid must have caused the difference, which is much more pronounced for $\xi$ than for $\eta_s$. Interestingly, on the basis of experimental data for the friction coefficient, Evans and Yeung and co-workers [13, 14] also arrived at a mismatch by one order of magnitude.

We end with a brief comparison of our numerical results with experimental data. Whereas the model amphiphile possesses only one relatively short tail, experiments have concentrated on phosphatidylcholine PC lipids with two longer tails of typically 18 carbons. It is to be expected, therefore, that the latter yield considerably higher surface viscosities and friction coefficients than the model amphiphiles, even if friction and random forces had properly been included in the model. Reported surface viscosities for lipid bilayers [13, 15, 19] are of the order of $10^{-7}$ to $10^{-6}$ surface poise (1 sp is equivalent to $10^{-3}$ Pa m s), as compared to the $8.5 \cdot 10^{-10}$ sp found by the perpendicular shear simulations. Experimental friction coefficients are rare, with $1 \cdot 10^8$ N s m$^{-3}$ reported by Evans and Yeung [13] and $4.5 \cdot 10^8$ N s m$^{-3}$ by Raphael and Waugh [11]. Chizmadzhev *et al.* [20] assumed in their analysis that $\eta_b = \xi' h_s = \eta_w' / h_s$; from their value of $\eta_b$ we arrive at $2 \cdot 10^9$ N s m$^{-3}$ for $h_s = 4$ nm. The parallel shear simulations yield $1.4 \cdot 10^6$ N s m$^{-3}$. In both cases, the simulation results are two to three orders of magnitude lower than the experimental values. As already alluded to, this is a consequence of using a simplified coarse grained model, which does not discredit the proposed simulation method in any way.

# Bibliography

[1] S. A. Shkulipa, W. K. den Otter, and W. J. Briels. Surface viscosity, diffusion, and intermonolayer friction: simulating sheared amphiphilic bilayers. *Biophys. J.*, 89:823–829, 2005.

[2] W. M. Gelbart, A. Ben-Shaul, and D. Roux. *Micelles, Membranes, Microemulsions, and Monolayers*. Springer-Verlag Inc., New York, U. S. A., 1994.

[3] U. Seifert. Configurations of fluid membranes and vesicles. *Adv. in Phys.*, 46(1):13–137, 1997.

[4] W. Rawicz, K. C. Olbrich, T. McIntosh, D. Needham, and E. Evans. Effect of chain length and unsaturation on elasticity of lipid bilayers. *Biophys. J.*, 79:328–339, 2000.

[5] E. Evans and V. Heinrich. Dynamic strength of fluid membranes. *C. R. Physique*, 4:265–274, 2003.

[6] S. W. Marlow and P. D. Olmsted. The effect of shear flow on the helfrich interaction in lyotropic lamellar systems. *Eur. Phys. J. E*, 8:485–497, 2002.

[7] P. Sierro and D. Roux. Structure of a lamellar phase under shear. *Phys. Rev. Lett.*, 78:1496–1499, 1997.

[8] O. Diat, D. Roux, and F. Nallet. ”layering” effect in a sheared lyotropic lamellar phase. *Phys. Rev. E*, 51:3296–3299, 1995.

[9] P. Panizza, A. Colin, C. Coulon, and D. Roux. A dynamic study of onion phases under shear flow: size changes. *Eur. Phys. J. B*, 4:65–74, 1998.

[10] E. A. Evans and R. Skalak. *Mechanics and thermodynamics of biomembranes*. CRC Press, Boca Raton, FL, U. S. A., 1980.

[11] R. M. Raphael and R. E. Waugh. Accelerated interleaflet transport of phosphatidylcholine molecules in membranes under deformation. *Biophys. J.*, 71:1374–1388, 1996.

[12] A. Yeung and E. Evans. Unexpected dynamics in shape fluctuations of bilayer vesicles. *J. Phys. II France*, 5:1501–1523, 1995.

[13] E. Evans and A. Yeung. Hidden dynamics in rapid changes of bilayer shape. *Chem Phys. Lipids*, 73:39–56, 1994.

[14] E. Evans, A. Yeung, R. Waugh, and J. Song. Dynamic coupling and nonlocal curvature elasticity in bilayer membranes. *Springer Proceedings in Physics*, 66:148–153, 1992.

[15] R. E. Waugh. Surface viscosity measurements from large bilayer vesicle tether formation. experiments. *Biophys. J.*, 38:29–37, 1982.

[16] R. E. Waugh. Surface viscosity measurements from large bilayer vesicle tether formation. analysis. *Biophys. J.*, 38:19–27, 1982.

[17] F. S. Bates and G. H. Fredrickson. Block copolymer thermodynamics - theory and experiment. *Annu. Rev. Phys. Chem.*, 41:525–557, 1990.

[18] P. G. Saffman. Brownian motion in thin sheets of viscous fluid. *J. Fluid Mech*, 73:593–602, 1976.

[19] R. Dimova, C. Dietrich, A. Hadjiisky, K. Danov, and B. Pouligny. Falling ball viscosimetry of giant vesicle membranes: Finite-size effects. *Eur. Phys. J. B*, 12:589–598, 1999.

[20] Y. A. Chizmadzhev, D. A. Kumenko, P. I. Kuzmin, L. V. Chernomordik, J. Zimmerberg, and F. Cohen. Lipid flow through fusion pores connecting membranes of different tensions. *Biophys. J.*, 76:2951–2965, 1999.

[21] D. P. Tieleman, S. J. Marrink, and H. J. C. Berendsen. A computer perspective of membranes: molecular dynamics studies of lipid bilayer systems. *Biochimica et Biophysica Acta*, 1331:235–270, 1997.

[22] U. Essmann and M. L. Berkowitz. Dynamical properties of phospholipid bilayers from computer simulation. *Biophys. J.*, 76:2081–2089, 1999.

[23] R. D. Groot and K. L. Rabone. Mesoscopic simulation of cell membrane damage, morphology change and rupture by nonionic surfactants. *Biophys. J.*, 81:725–736, 2001.

[24] E. Lindahl and O. Edholm. Mesoscopic undulations and thickness fluctuations in lipid bilayers from molecular dynamics simulations. *Biophys. J.*, 79:426–433, 2000.

[25] M. Kranenburg, J. P. Nicolas, and B. Smit. Comparison of mesoscopic phospholipid-water models. *Phys. Chem. Chem. Phys.*, 108:4142–4151, 2004.

[26] S. J. Marrink, A. H. de Vries, and A. E. Mark. Coarse grained model for semiquantitative lipid simulations. *J. Phys. Chem.*, 108:750–760, 2004.

[27] R. Goetz, G. Gompper, and R. Lipowsky. Mobility and elasticity of self-assembled membranes. *Phys. Rev. Lett.*, 82:221–224, 1999.

[28] R. Goetz and R. Lipowsky. Computer simulations of bilayer membranes: Self-assembly and interfacial tension. *J. Chem. Phys.*, 108:7397–7409, 1998.

[29] W. K. den Otter, S. A. Shkulipa, and W. J. Briels. Buckling and persistence length of an amphiphilic worm from molecular dynamics simulations. *J. Chem. Phys.*, 119(4):2363–137, 2003.

[30] T. V. Tolpekina, W. K. den Otter, and W. J. Briels. Nucleation free energy of pore formation in an amphiphilic bilayer studied by molecular dynamics simulations. *J. Chem. Phys.*, 121(23):12060–12066, 2004.

[31] T. V. Tolpekina, W. K. den Otter, and W. J. Briels. Simulations of stable pores in membranes: System size dependence and line tension. *J. Chem. Phys.*, 121(16):8014–8020, 2004.

[32] R. L. C. Akkermans and W. J. Briels. Coarse-grained dynamics of one chain in a polymer melt. *J. Chem. Phys.*, 41:6409–6422, 2000.

[33] C. W. Gardiner. *Handbook of stochastic methods : for physics, chemistry and the natural sciences*. Springer-Verlag Inc., New York, U. S. A., 1985.

[34] J. T. Padding and W. J. Briels. Time and length scales of polymer melts studied by coarse-grained molecular dynamics simulations. *J. Chem. Phys.*, 117(2):925–943, 2002.

[35] W. Smith and T. R. Forester. Dlpoly2.0: A general-purpose parallel molecular dynamics simulation package. *J. Mol. Graphics*, 14:136–141, 1996.

[36] M. P. Allen and D. J. Tildesley. *Computer Simulation of Liquids*. Oxford University Press, Oxford, U. K., 1987.

[37] A. W. Lees and S. F. Edwards. The computer study of transport processes under extreme conditions. *J. Phys. C*, 5:1921–1929, 1972.

[38] B. L. Holian. Evaluating shear viscosity: Power dissipated versus entropy produced. *J. Chem. Phys.*, 117:9567–9568, 2002.

[39] A. J. Queimada, S. E. Quinones-Cisneros, I. M. Marrucho, J. A. P. Coutinho, and E. H. Stenby. Viscosity and liquid density of asymmetric hydrocarbon mixtures. *International Journal of Thermophysics*, 24(5):1221–1239, 2003.

# 3 Thermal undulations of lipid bilayers relax by intermonolayer friction at sub-micrometer length scales

*The time correlation functions of the thermal undulations of a lipid membrane have been studied by molecular dynamics simulations of a coarse-grained bilayer model. We observe a double-exponential decay, with relaxation rates in good agreement with the theory by Seifert and Langer [Europhys. Lett.* ***23****, 71 (1993)]. Intermonolayer friction resulting from local velocity differences between the two monolayers is shown to be the dominant dissipative mechanism for fluctuations with wave lengths below* $\sim 0.1\mu m$. *

Biological membranes are amphiphilic bilayers composed of lipids interspersed with fatty acids, sterols and proteins. They serve to isolate the contents of the cell from the outside world and to separate compartments within the cell. Besides transmitting chemical stimuli by means of their proteins,[2] they offer the possibility of transporting material from one side to the other by simple diffusion,[3] through channels[3] or by budding and subsequent pinching off of the bud.[4] Obviously they provide mechanical support to their contents. The mechanical and thermodynamic properties of membranes have therefore been studied intensively through the past few decades.[5, 6, 7, 8] From a theoretical point of view it is attractive to attribute these properties to a mathematical surface, the neutral surface,[9] as for example in the celebrated Helfrich free energy:[10]

$$F = \int \left[2\kappa H^2 + \bar{\kappa}K + (k/2)(\phi/\phi_0 - 1)^2\right] da. \tag{3.1}$$

The integral is over the surface of the membrane, $H$ is the local mean curvature, $K$ the local

∗ The work described in this chapter previously appeared in Physical Review Letters **96**, 178302 (2006) [1].

Gaussian curvature and $\phi$ the local density. $\kappa$ and $\bar{\kappa}$ are the bending rigidity and saddle-splay modulus, respectively, $k$ is the compressibility modulus, and $\phi_0$ is the equilibrium density. In the sequel the Gaussian curvature plays no role and will be omitted.

In combination with the relevant hydrodynamic equations, the Helfrich free energy may be used to study the dynamics of membranes at large length scales. [11, 12, 13, 14, 15, 16, 17] In many cases of interest, however, small scale deformations of the membrane occur, which force the two monolayers to slip along oneanother[18] with velocity difference $\Delta v$, giving rise to an intermonolayer friction force per unit area $F_{\rm slip} = b\Delta v$, with friction coefficient $b$. This happens for example in erythrocytes as they wriggle through narrow passageways,[5] during the pulling of tethers by kinesine motor proteins,[19] in cleavage of cells during the last stage of cell division,[3] and in the formation of vesicles from existing membranes by budding.[4] Several experiments have been performed to measure the friction coefficient $b$. Evans and Yeung[20] and Raphael and Waugh[21] reported on tether pulling experiments, while Chizmadzhev *et al.*[22] induced slippage by pulling a bilayer through a toroidal fusion pore. Typical values of the friction coefficients obtained this way are $b = 10^8 - 10^9\,\mathrm{Ns/m^3}$ for a range of lipids bilayers.

The theory describing the dynamics of an undulating bilayer with slipping monolayers was first discussed by Seifert and Langer.[23, 24] Independently, one year later, Evans and Yeung[20, 25] published a similar theory for undulating vesicles, which has since been extended.[26, 27] To the best of our knowledge, only two papers so far on measurements of shape fluctuations have provided some, still inconclusive, support for these theories.[28, 29] Previous simulations of the dynamics of bilayer fluctuations have not been analysed with the appropriate equations.[30]

By ignoring peristaltic modes, i.e., by fixating the distance between the neutral surfaces of the two monolayers to a value of $2d$, the degrees of freedom of the bilayer reduce to three fields. One is the position $h(x,y)$ of the midsurface, i.e., the surface halfway the two monolayers. The other two fields are the two monolayer densities $\phi^{\pm}(x,y)$. It is convenient to use densities which are projected on the midsurface,[7, 23, 24] $\psi^{\pm} = \phi^{\pm}(1 \mp 2dH)$, since it is the difference of the velocities corresponding to these densities which determines the intermonolayer friction. This can be understood by noticing that a uniform bending of the bilayer should not result in any friction. Finally, we introduce the normalized density differ-

ence $\rho^{\Delta}(x,y) = (\psi^{+} - \psi^{-})/\phi_0$ and average density $\rho^{\Sigma}(x,y) = (\psi^{+} + \psi^{-})/\phi_0 - 1$, and notice that fluctuations of the latter are decoupled from those of the other degrees of freedom.[23] This leaves us with the coupled dynamics of two fields, $h(x,y)$ and $\rho^{\Delta}(x,y)$. After a Fourier transformation of the appropriate force balances, Seifert and Langer arrived at[7, 23, 24]

$$\frac{\partial}{\partial t}\begin{pmatrix} h_{\mathbf{q}} \\ \rho^{\Delta}_{\mathbf{q}} \end{pmatrix} = \begin{pmatrix} 1/4\eta q & 0 \\ 0 & q^2/4b \end{pmatrix} \begin{pmatrix} \tilde{\kappa}q^4 & -kq^2 d \\ -kq^2 d & k \end{pmatrix} \begin{pmatrix} h_{\mathbf{q}} \\ \rho^{\Delta}_{\mathbf{q}} \end{pmatrix}, \tag{3.2}$$

where $t$ is the time, $\tilde{\kappa} = \kappa + d^2 k$, and $\eta$ is the viscosity of the solvent surrounding the bilayer. The vectors represent the conformation of the bilayer in Fourier space, with $\mathbf{q}$ being the wave-vector of the Fourier components and $q$ its length. Modes with different wave-vectors are decoupled. The second matrix on the right hand side is the Hessian of the free energy of the bilayer expressed in the complex Fourier components $h_{\mathbf{q}}$ and $\rho^{\Delta}_{\mathbf{q}}$ of the fields $h(x,y)$ and $\rho^{\Delta}(x,y)$. The first matrix is called the mobility matrix. The final solution follows after diagonalization of the product of the two matrices.

We now invoke Onsager's regression hypothesis,[31] in combination with the above theory, to describe the dynamics of the fluctuations of a bilayer around its equilibrium state. The height-height time correlation function then reads[7]

$$\langle h_{\mathbf{q}}(t) h^{*}_{\mathbf{q}}(0)\rangle = A^{h}_{1} e^{-\gamma_1 t} + A^{h}_{2} e^{-\gamma_2 t}, \tag{3.3}$$

where the angular brackets denote a canonical average and the asterisk indicates a complex conjugate. $A^{h}_{1}$ and $A^{h}_{2}$ are two $q$-dependent amplitudes.[7] The relaxation rates $\gamma_1$ and $\gamma_2$ are the smallest and the largest eigenvalue, respectively, of the product of the two matrices in Eq. (3.2). Their dependence on the wavenumber $q$ is shown in Fig. 3.1, using particular values for the various parameters pertaining to our coarse-grained model, to be described below. The curves exhibit an avoided crossing around a critical wavenumber $q_c = \eta k/b\tilde{\kappa}$, similar to those found in phonon dispersion curves. Inspection of the corresponding eigenvectors[7, 23] reveals that the slow mode has bending character at low wavenumbers and slipping character at large wavenumbers, as indicated in the figure. The opposite holds true for the fast mode. The bending part of the slow mode behaves like $\gamma_1 = \kappa q^3/4\eta$ and that of the fast mode like $\gamma_2 = \tilde{\kappa} q^3/4\eta$. For the slipping branches one finds $\gamma_2 = kq^2/4b$ at small wavenumbers and $\gamma_1 = k\kappa q^2/4b\tilde{\kappa}$ at high wavenumbers. In the limit of zero thickness, $d = 0$, the avoided crossing disappears and the two bending parts merge into one line with $\gamma = \kappa q^3/4\eta$, also

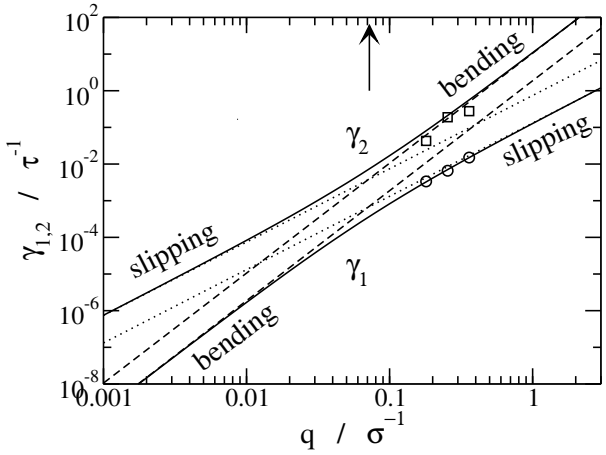


Figure 3.1: The slow $\gamma_1$ and fast $\gamma_2$ relaxation rates (solid lines) of an undulating bilayer as functions of the wavenumber $q$, calculated using the parameters of the coarse-grained model. The slipping branches scale as $q^2$ and are damped by intermonolayer friction, the bending branches scale as $q^3$ and relax through viscous dissipation by the solvent. Dashed and dotted lines denote extrapolations of the limiting regimes at low and high $q$; the vertical distance between each set of parallel lines is $\log(\tilde{\kappa}/\kappa)$. The arrow indicates the cross-over wave-number $q_c$ where the relaxation characters of the slow and fast modes are gradually exchanged. Circles and squares mark the relaxation rates obtained by fitting the simulated height correlation functions of Fig. 3.2

described by the older theories, [11, 12, 13, 14] while the slipping parts merge into one line with $\gamma = kq^2/4b$, not treated in the older theories.

Simulations[32, 33] were done using a simple coarse grained model,[34] in which the amphiphiles are represented by short chains of one head particle and four tail particles, connected by harmonic springs and a bending potential. The solvent consists of loose particles. Non-bonded interactions between particles are of the Lennard-Jones type, $\phi_{\mathrm{LJ}} = 4\varepsilon[(r/\sigma)^{-6} - (r/\sigma)^{-12}]$, except for a purely repulsive potential $\phi_{\mathrm{rep}} = \varepsilon[r/(1.05\sigma)]^{-9}$ modelling the hydrophobic interactions. A Nosé-Hoover thermostat was used to maintain a temperature of $1.35\varepsilon/k_B$. Indicative translations of simulation results to experimental values are

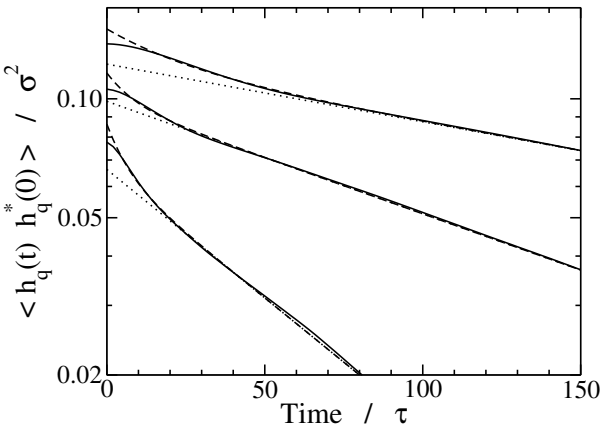


Figure 3.2: Time correlation functions of the Fourier components of the height of a thermally fluctuating bilayer (solid lines), for the three smallest wavenumbers commensurable with the box dimension, $q_1 = 0.18\sigma^{-1}$ (top), $q_2 = 0.25\sigma^{-1}$ (middle, multiplied by 2.5) and $q_3 = 0.36\sigma^{-1}$ (bottom, multiplied by 8). The dashed lines are double exponential fits, excluding the transient part of the simulation data; the dotted straight lines show the contributions of the slow modes to these fits.

obtained by using[34] $\varepsilon = 2\,\mathrm{kJ/mol}$, $\sigma = 1/3\,\mathrm{nm}$ and the particle mass $m = 36\,\mathrm{a.u.}$, which imply a unit of time $\tau = 1.4\,\mathrm{ps}$. This particular model is one of the best-studied coarse grained models available, with previous simulations focusing on its bending rigidity,[35, 36, 37] apparent[34] and intrinsic[37] compressibility, edge energy,[38] and the free energy profile of pore formation.[39] It is the first model for which the surface viscosity and the intermonolayer friction have been established, using non-equilibrium simulations.[40] As expected for a simple coarse grained model with a single short tail, its dynamical properties turned out to be some two orders of magnitude faster than the experimental data on amphiphiles with two longer tails. In combination with its inherent simplicity, this makes the model particularly appealing for exploratory studies like the current study on the importance of intermonolayer friction on the thermal undulations of a bilayer. Figure 3.1 was calculated using $k = 11\varepsilon\sigma^{-2}$, $\kappa = 7.5\varepsilon$, $b = 3.7\varepsilon^{1/2}m^{1/2}\sigma^{-3}$, $\eta = 1.0\varepsilon^{1/2}m^{1/2}\sigma^{-2}$ and an estimated $d = t/4$ for a bilayer

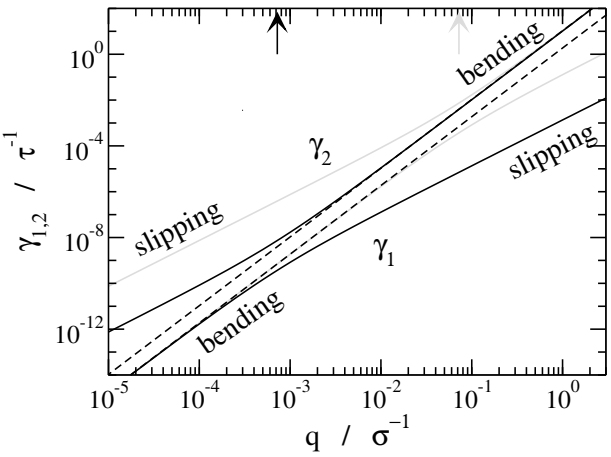


Figure 3.3: The relaxation rates of the coarse grained model before (grey) and after (black) a 100-fold increase of the intermonolayer friction, to bring this parameter on a par with experimental values. Changing $b$ does not affect the relaxation rates of the bending branches, whose limits are indicated by dashed lines. The rates of the slipping branches, however, are reduced by a factor of 100, and the cross-over wavenumber (arrows) is reduced accordingly. Atomistic and coarse grained simulations live in the top-right corner of the plot, as these systems typically contain $10^3$ lipids, corresponding to $q \sim 0.1\sigma^{-1}$, with simulation times usually of the order of $10^4\tau$.

of thickness $t = 7\sigma$.

The simulated system comprised a 1152 amphiphile bilayer and 10,800 solvent particles at a number density of $2/3\sigma^3$ in a periodic simulation box. The area of the square $xy$ ground plane of the box, oriented parallel to the bilayer, was adjusted till the average pressures parallel and perpendicular to the bilayer were equal, establishing a tension-less state.

In Fig. 3.2 we present the calculated time dependent height autocorrelation functions for the three longest wavelengths commensurable with the dimensions of the simulation box. For each of these wave numbers, $q_1 = 0.18\sigma^{-1}$, $q_2 = 0.25\sigma^{-1}$ and $q_3 = 0.36\sigma^{-1}$, there are two allowed wave vectors, which were both used to produce the averaged curves shown in the figure. The dashed lines are the best representations of the data using two exponentially

decaying terms. As usual, because of time reversal symmetry, the early parts of the curves do not follow the macroscopic theory[31] and must be deleted from the fitting procedure. At the lowest wave number two regimes can clearly be discerned, while with increasing wave number the first regime becomes too short to be measured accurately. The second, slow regime in all cases extends over large enough time intervals to allow a precise measurement of the corresponding characteristic times $\gamma_1^{-1}$. The results are represented in Fig. 3.1 by circles, and agree perfectly well with the rates predicted by the theory of Seifert and Langer. Also shown in Fig. 3.1 are the calculated fast relaxation rates $\gamma_2$. Given the difficulties with determining their values, they agree fairly well with the theoretical predictions. These results provide strong evidence for the validity of the theory by Seifert and Langer. [23, 24]

As is clear from Fig. 3.1, the slowest relaxations at the wavenumbers studied in this paper have mainly slipping character. The main shortcoming of the model used in our simulations is a value of $b$ which is smaller than typical experimental values by a factor of about 100. A drawing of the dispersion curves with this larger value of $b$, and otherwise the same parameters as used before, is depicted in Fig. 3.3. The bending parts of the plot remain unchanged, while the slipping parts move downwards along the vertical axis since in the latter regimes $\gamma_{1,2} \propto b^{-1}$. As a result, the critical wavenumber moves to lower values as well. Using realistic values for all membrane parameters we obtain $q_c \approx 0.01\,\mathrm{nm}^{-1}$, indicating that the relaxation of membrane fluctuations at length scales below $\sim 0.1\mu$m is dominated by intermonolayer friction. Note that many experiments[15, 41, 42] probe wavenumbers at larger length scales, and therefore sample undulations which mainly relax through energy dissipation by the viscous solvent.

We draw one more conclusion from the above discussion, concerning particle based simulations of bilayers. In simulations of systems with realistic values for the intermonolayer friction coefficient, the longest relaxation time will often be too long to be sampled sufficiently well, even if one chooses small systems to exploit their relatively small relaxation times. Since the usual way to measure the bending rigidity[30, 35, 36, 43] assumes that all fluctuations are fully sampled, such calculations, when applied to atomistic simulations, must be met with care.

The main results of this paper are a confirmation of the theory by Seifert and Langer describing the relaxation dynamics of undulations in lipid bilayers, and the conclusion, illus-

trated by the presented molecular dynamics simulations, that at length scales below $\sim 0.1\mu$m the relaxations are dominated by intermonolayer friction.

# Bibliography

[1] S. A. Shkulipa, W. K. den Otter, and W. J. Briels. Thermal undulations of lipid bilayers relax by intermonolayer friction at submicrometer length scale. *Phys. Rev. Lett.*, 96:178302, 2006.

[2] L. Stryer. *Biochemistry*. W. H. Freeman and Comp., New York, NY, 4 edition, 1995.

[3] W. M. Becker and D. W. Deamer. *The world of the cell*. Benjamin/Cummings Publishing Company, Redwood City, CA, 1991.

[4] J. S. Bonifacino and B. S. Glick. *Cell*, 116:153, 2004.

[5] E. A. Evans and R. Skalak. *Mechanics and thermodynamics of biomembranes*. CRC Press, Boca Raton, FL, 1980.

[6] W. M. Gelbart, A. Ben-Shaul, and D. Roux. *Micelles, membranes, microemulsions, and monolayers*. Springer-Verlag Inc., New York, NY, 1994.

[7] U. Seifert. Configurations of fluid membranes and vesicles. *Adv. in Phys.*, 46(1):13–137, 1997.

[8] D. Boal. *Mechanics of the cell*. Cambridge University Press, Cambridge, U.K., 2002.

[9] S. A. Safran. *Statistical mechanics of surfaces, interfaces and membranes*. Addison-Wesley, Reading, MA, 1994.

[10] W. Helfrich. *Z. Naturforsch. C*, 28:693, 1973.

[11] L. Kramer. Theory of light scattering from fluctuations of membranes and monolayers. *J. Chem. Phys.*, 55:2097–2105, 1971.

[12] F. Brochard and J. F. Lennon. *J. Phys. (Paris)*, 11:1035, 1975.

[13] S. T. Milner and S. A. Safran. Dynamical fluctuations of droplet microemulsions and vesicles. *Phys. Rev. A*, 36:4371–4379, 1987.

[14] R. Granek. From semi-flexible polymers to membranes: anomolous diffusion and reptation. *J. Phys. II France*, 7:1761–1788, 1997.

[15] T. M. Bayerl. Collective membrane motions. *Curr. Opin. Colloid Interface Sci*, 5:232–236, 2000.

[16] L. C. L. Lin and F. L. H. Brown. Brownian dynamics in fourier space: membrane simulations over long length and time scales. *Phys. Rev. Lett.*, 93:256001, 2004.

[17] L. C. L. Lin and F. L. H. Brown. Dynamic simulations of membranes with cytoskeletal interactions. *Phys. Rev. E*, 72:011910, 2005.

[18] E. Evans, A. Yeung, R. Waugh, and J. Song. Dynamic coupling and nonlocal curvature elasticity in bilayer membranes. *Springer Proceedings in Physics*, 66:148–153, 1992.

[19] G. Koster, M. VanDuijn, B. Hofs, and M. Dogterom. Membrane tube formation from giant vesicles by dynamic association of motor proteins. *Proc. Nat. Acad. Sci. USA*, 100:15583–15588, 2003.

[20] E. Evans and A. Yeung. Hidden dynamics in rapid changes of bilayer shape. *Chem. Phys. Lipids*, 73:39–56, 1994.

[21] R. M. Raphael and R. E. Waugh. Accelerated interleaflet transport of phosphatidylcholine molecules in membranes under deformation. *Biophys. J.*, 71:1374–1388, 1996.

[22] Y. A. Chizmadzhev, D. A. Kumenko, P. I. Kuzmin, L. V. Chernomordik, J. Zimmerberg, and F. Cohen. Lipid flow through fusion pores connecting membranes of different tensions. *Biophys. J.*, 76:2951–2965, 1999.

[23] U. Seifert and S. A. Langer. Viscous modes of fluid bilayer membranes. *Europhys. Lett.*, 23:71–76, 1993.

[24] U. Seifert and S. A. Langer. Hydrodynamics of membranes: the bilayer aspect and adhesion. *Biophys. Chem.*, 49:13–22, 1994.

[25] A. Yeung and E. Evans. Unexpected dynamics in shape fluctuations of bilayer vesicles. *J. Phys. II France*, 5:1501–1523, 1995.

[26] I. Bivas, P. Méléard, I. Mircheva, and P. Bothorel. Thermal shape fluctuations of a quasi spherical lipid vesicle when the mutual displacements of its monolayers are taken into account. *Colloids Surf. A*, 157:21–33, 1999.

[27] L. Miao, M. A. Lomholt, and J. Kleis. Dynamics of shape fluctuations of quasi-spherical vesicles revisited. *Eur. Phys J. E*, 9:143–160, 2002.

[28] W. Pfeiffer, S. König, J. F. Legrand, T. Bayerl, D. Richter, and E. Sackmann. Neutron spin echo study of membrane undulations in lipid multibilayers. *Europhys. Lett.*, 23:457–462, 1993.

[29] T. Pott and Méléard. The dynamics of vesicle thermal fluctuations is controlled by intermonolayer friction. *Europhys. Lett.*, 59:87–93, 2002.

[30] E. Lindahl and O. Edholm. Mesoscopic undulations and thickness fluctuations in lipid bilayers from molecular dynamics simulations. *Biophys. J.*, 79:426–433, 2000.

[31] D. Chandler. *Introduction to modern statistical mechanics*. Oxford University Press, New York, NY, 1987.

[32] D. Frenkel and B. Smit. *Understanding Molecular Simulation*. Academic Press, San Diego, CA, 1996.

[33] M. P. Allen and D. J. Tildesley. *Computer simulation of liquids*. Oxford University Press, Oxford, U. K., 1987.

[34] R. Goetz and R. Lipowsky. Computer simulations of bilayer membranes: Self-assembly and interfacial tension. *J. Chem. Phys.*, 108:7397–7409, 1998.

[35] R. Goetz, G. Gompper, and R. Lipowsky. Mobility and elasticity of self-assembled membranes. *Phys. Rev. Lett.*, 82:221–224, 1999.

[36] W. K. den Otter and W. J. Briels. The bending rigidity of an amphiphilic bilayer from equilibrium and nonequilibrium molecular dynamics. *J. Chem. Phys.*, 118:4712, 2003.

[37] W. K. den Otter. Area compressibility and buckling of amphiphilic bilayers in molecular dynamics simulations. *J. Chem. Phys.*, 123:214906, 2005.

[38] T. V. Tolpekina, W. K. den Otter, and W. J. Briels. Simulations of stable pores in membranes: System size dependence and line tension. *J. Chem. Phys.*, 121(16):8014–8020, 2004.

[39] T. V. Tolpekina, W. K. den Otter, and W. J. Briels. Nucleation free energy of pore formation in an amphiphilic bilayer studied by molecular dynamics simulations. *J. Chem. Phys.*, 121(23):12060–12066, 2004.

[40] S. A. Shkulipa, W. K. den Otter, and W. J. Briels. Surface viscosity, diffusion, and intermoloayer friction: simulating sheared amphiphilic bilayers. *Biophys. J.*, 89:823, 2005.

[41] É. Freyssingeas, D. Roux, and F. Nallet. Quasi-elastic light scattering study of highly swollen lamellar and "sponge" phases. *J. Phys. II France*, 7:913–929, 1997.

[42] G. Althoff, D. Frezzato, G Kothe, G. J. Moro, M. Vilfan, I. Vilfan, O. Stauch, and R. Schubert. Transverse nuclear spin relaxation induced by shape fluctuations in membrane vesicles. theory and experiments. *Mol. Cryst. Liq. Cryst.*, 394:93–106, 2003.

[43] S. J. Marrink and A. E. Mark. Effect of undulations on surface tension in simulated bilayers. *J. Phys. Chem. B*, 105:6122–6127, 2001.

# 4 Molecular dynamics simulations of thermal undulations of lipid bilayers in the tension-less state and under stress

*The relaxation processes of height undulations and density fluctuations in a membrane have been studied by molecular dynamics simulations of a coarse-grained amphiphilic bilayer model. We observe a double exponential decay in their time correlations, with relaxation rates in good quantitative agreement with the theory by Seifert and Langer [Europhys. Lett.* ***23****, 71 (1993)]. Intermonolayer friction due to slippage between the two monolayers is shown to be the dominant dissipative mechanism at the high wavenumbers, $q > 10\mu m^{-1}$, typically encountered in computer simulations. We briefly discuss the ramifications of the slow undulatory relaxation process for the calculation of bending rigidities from the static undulation structure factors. The relaxation rates are sensitive to the surface tension, and at high elongations an oscillatory contribution is observed in the time correlation of the undulations.*

## 4.1 Introduction

Membranes are of vital importance to biological cells, by providing mechanical support, hosting proteins, compartimentalizing the cell and acting as semipermeable barriers between the cell and its environment.[1, 2] This feat is achieved by lipids, i.e., molecules with a hydrophilic head group and one or two hydrophobic tails, which self-assemble into bilayered membranes when dissolved in an aqueous liquid. An interplay of non-covalent interactions, between the amphiphilic lipids and with the solvent, makes these bilayers stable, yet flexible

and dynamical. The twinned nature of a bilayer is important if biological reasons require the inside of the membrane to differ from its outside, which seems to be the case in many membranes.

The mechanical and thermodynamical properties of membranes are well described by the Helfrich theory,[3, 4] which regards both bilayers and monolayers as single smoothly undulating surfaces with free energies consisting of bending and elastic contributions. The motion of a bilayer under these internal forces is damped through energy dissipation by shear forces, within the bilayer but predominately in the solvent. Combining the Helfrich theory for the membrane with the Stokes approximation for the low Reynolds number hydrodynamical flow of the solvent, an excited undulation with wavenumber $q$ in a tension-less membrane is found to decay exponentially with a relaxation rate $\Gamma = \kappa q^3/4\eta$, where $\kappa$ is the bending rigidity of the membrane and $\eta$ the viscosity of the solvent. [5, 6, 7, 8] Following Onsager's regression hypothesis,[9] the same rate also governs the Brownian or thermal undulations of a membrane, which were already observed several centuries ago as the 'flickering' of a red blood cell under an optical microscope.[6] Numerous experiments have confirmed this scaling law for $\Gamma$, including video microscopy of individual giant unilamellar vesicles, [10, 11] scattering experiments on highly diluted lamellar and sponge phases, [12, 13] and spin relaxation measurements of vesicle solutions.[14]

A decade ago, Evans *et al.*[15] emphasised the existence of a hitherto 'hidden' dissipative process, resulting from friction forces between the two leaflets of a bilayer as they slip past one another. This process is of importance in all shape deformations of bilayers, but especially so for rapid changes which allow the density distributions of the leaflets little time to accommodate. Slippage is readily induced in experiments by forcing the membrane lipids to flow through a region of high local curvature, e.g., by pulling a tether from a vesicle,[15, 16] by the spontaneous retraction of this tether,[17] or by using a fusion pore to connect two bilayers under distinct tensions.[18] In computer simulations, slippage has been brought about by exposing a bilayer and the surrounding solvent to a parallel shear flow.[19] It is to be expected that friction also plays a role in biological processes, like the conformational changes of erythrocytes as they travel around the body,[1] the cleavage of an animal cell during the later stages of cell division,[2] and the budding of membranes to form vesicles.[20] Typical values for the intermonolayer friction coefficient $b$, defined as the proportionality constant between

the slip velocity and the friction force per unit area, are of the order of $(1-10)\cdot 10^8\,\mathrm{Ns/m^3}$. [16, 18, 21, 22]

Interestingly, theoretical considerations have shown that the effects of intermonolayer friction are also relevant at the small slip velocities occurring during the thermal undulations of a bilayer. Seifert and Langer[23, 24] derived the equations of motion for a planar bilayer, explicitly treating the bilayer as two coupled monolayers, yielding two exponentially decaying relaxation processes with $\gamma_1$ and $\gamma_2$ as the slow and fast relaxation rates, respectively. For low wave numbers, the aforementioned solvent-dominated mechanism was recovered as the slow relaxation process, $\gamma_1 = \Gamma \propto q^3$, with the fast relaxation scaling as $\gamma_2 \propto q^2$. In this paper, the focus will be on the high and intermediate wave number regime, as this covers the length scales attainable in computer simulations of atomistic and coarse grained bilayer models.[25] The theory of Seifert and Langer predicts for this case that the slow relaxation process results from energy dissipation by intermonolayer friction, $\gamma_1 \propto q^2$, while the fast rate now scales as $\gamma_2 \propto q^3$ – a more detailed discussion of these dissipative mechanisms will be given in the theory section. Experiments supporting this theory are sparse, however. Spin-echo measurements on a dense lamellar stack of bilayers, interspersed by water layers of $\sim$10 Å thickness, seem to favour the predicted quadratic dispersion relation at high $q$ values, although the confirmation of theory is not clear-cut in this particular set-up.[23, 26, 27] Other high-wavenumber studies, like atomistic molecular dynamics (MD) simulations[28] and neutron spin-echo experiments on semi-dilute lamellar phases,[29] have been fitted with the conventional relaxation rate $\Gamma \propto q^3$, which according to the current theory should hold true only for the low $q$, solvent-dominated relaxation process.

Evans and Yeung[16, 30] derived equations of motion for axially symmetric bilayer configurations, in order to study both the pulling of a tether from a vesicle and the thermal undulations of a vesicle. A related theory specifically aimed at the latter case has been put forward by Bivas *et al.*[31]. Like for planar bilayers, a double exponential decay is predicted, where again for large wave numbers the slow relaxation is dominated by intermonolayer friction. The video microscopy experiments by Pott and Méléard[22] provided the first (and to the best of our knowledge also the only) confirmation of the existence of two relaxation processes in vesicles. A quantitative analyses, however, yielded intermonolayer friction coefficients exceeding previous measurements by one or two orders of magnitude, depending

on the theoretical model used. Miao *et al.*[32] argued that this deviation might be diminished by a re-interpretation of the elastic modulus, whose apparent value decreases drastically with increasing length scales.[33, 34, 35, 36] An oscillatory component in the experimental relaxation data, clearly visible against the small amplitude of the slow decay process, has not been explained yet.

The experimental evidence for current theories on the thermal motion of a tensionless membrane, and the alleged prominent role played herein by the phenomenological friction coefficient, is therefore indicative but not conclusive. In this paper, we use molecular dynamics simulations of a planar coarse grained bilayer to validate the theory. In Section 4.2 we recapitulate the main points of the theory, while the bilayer model and the applied analysis routines are briefly introduced and motivated in Section 6.3. Our simulation results are presented in Section 4.4, followed by an extensive discussion and summary in Section 5.6.

## 4.2 Theory

The equations of motion for a bilayer with friction forces between its two monolayers were first derived in the early 1990s by Seifert and Langer[23, 24] for a near-planar membrane and independently by Evans and Yeung[16, 30] for an axially symmetric configuration. In this section we present a concise overview of the major steps in the first of these, to provide the necessary background information and to highlight several points which will turn out to be of importance in the numerical analysis, culminating in two autocorrelation functions that can be compared against our simulation results.

Conforming to Seifert and Langer, we write the free energy $F$ of a bilayer as a sum of two terms, expressing the contributions of each of the two monolayers. The free energy of each monolayer is next written as an integral of the Helfrich free energy densities $f^{\pm}$ along the corresponding so-called neutral surfaces $S^{\pm}$,

$$F = \int f^{+}(h^{+}, \phi^{+})\, dS^{+} + \int f^{-}(h^{-}, \phi^{-})\, dS^{-}. \tag{4.1}$$

Here $h^{\pm}$ is the height above the ground plane of the upper (+) and lower (-) monolayer, and $\phi^{\pm}$ is the corresponding surface number density of amphiphiles. It is our aim in this section, again in conformity with Seifert and Langer, to rewrite the above free energy as an integral

over a single surface $S$, for which we choose the midplane of the bilayer, i.e., the surface with height $h = (h^+ + h^-)/2$:

$$F = \int f(h, \psi^+, \psi^-)\, dS, \tag{4.2}$$

where $\psi^\pm$ are projected densities defined below. The reason for doing this is two-fold. First, on bending bilayers, not only will both monolayers bend, but besides this one monolayer will expand while the other gets compressed. Yet we want to attribute the total free energy cost of this process to a bending term in the free energy of the bilayer. Secondly, because intermonolayer friction is associated with motion at the midsurface, it will be convenient to have available densities $\psi^\pm$ at this surface.

### 4.2.1 Statics

In the Helfrich model[3, 4] the free energy surface density $f$ of a curved monolayer is expressed as the sum of a bending term and a density term, which are decoupled by definition if the curvature $H$ and the density $\phi$ are defined relative to the so-called neutral surface of the monolayer. In the case of a bilayer, this applies to each of the two monolayers independently:

$$f^\pm = \frac{\kappa_m}{2}(2H^\pm)^2 + \frac{k_m}{2}\left(\frac{\phi^\pm}{\phi_0} - 1\right)^2. \tag{4.3}$$

The superscripts + and − refer to the upper and lower monolayer, respectively, of a symmetric bilayer membrane with zero spontaneous curvature. The bending rigidity $\kappa_m$ and elastic modulus $k_m$ are material properties of one monolayer, as is the equilibrium density $\phi_0$. Using the Monge representation[4] for the heights $h^\pm(\mathbf{x})$ of the nearly flat neutral surfaces, with $\mathbf{x} = (x, y)$ denoting the two Cartesian directions parallel to the bilayer, the mean curvatures of the monolayers are readily calculated as $H^\pm = \frac{1}{2}\nabla^2_{\mathbf{x}} h^\pm$. The saddle-splay free energy resulting from the Gaussian curvature has been ignored in Eq. (6.1) because this term is constant by the Gauss-Bonnett theorem. The free energy of the bilayer is obtained by integrating $f^+$ and $f^-$ over the corresponding neutral surfaces and adding the results, see Eq. (6.4). Instead of using two neutral surfaces, it is much more convenient to refer all quantities to just one surface, for which the midsurface of the bilayer $h(\mathbf{x})$, with mean curvature $H = \frac{1}{2}\nabla^2_{\mathbf{x}} h$, is conveniently chosen. If the two neutral surfaces are at a fixed distance $d$ from the midsurface, measured parallel to the normal, then $H^\pm = H(1 \pm 2Hd)$ to first order[4] in $d$. By summing the bending

free energies of the two monolayers, we find that the bending free energy of the bilayer equals $\kappa_m(2H)^2$ to lowest order in $H$, and so has a bilayer bending rigidity equal to twice the monolayer value, $\kappa = 2\kappa_m$. Next, we define monolayer densities $\psi^{\pm}(\mathbf{x})$ also relative to the midsurface. Area changes incurred during projections of particle positions onto the midplane, due to the curvatures of the involved surfaces, are accounted for by[4] $\psi^{\pm} = \phi^{\pm}(1 \mp 2Hd)$. Since we are interested in fluctuations, it is convenient to introduce $\rho^{\Delta} = (\psi^{+} - \psi^{-})/2\phi_0$ and $\rho^{\Sigma} = (\psi^{+} + \psi^{-})/2\phi_0 - 1$. The elastic energy density of the bilayer then reads

$$f_{\text{elas}} = f^{+}_{\text{elas}} + f^{-}_{\text{elas}} \approx k_m(\rho^{\Sigma})^2 + k_m(\rho^{\Delta})^2 + 4k_m\rho^{\Delta}Hd + k_m 4d^2H^2 \tag{4.4}$$

to lowest order in the three fields. Since intermonolayer frictions are induced by fluctuations of $\rho^{\Delta}$, and coupling terms between $\rho^{\Sigma}$ and $\rho^{\Delta}$ are absent in the free energy, the dynamics of $\rho^{\Sigma}$ is decoupled from that of $\rho^{\Delta}$ and $H$.

For nearly flat bilayers the integration of $f = f^{+} + f^{-}$ over the midsurface is readily achieved by using Fourier transformations along the $xy$ plane. For the undulations we write $h(\mathbf{x}) = \sum_{\mathbf{q}} h_{\mathbf{q}} \exp(i\mathbf{q}\cdot\mathbf{x})$, where for real $h(\mathbf{x})$ the complex coefficients are related by $h_{\mathbf{q}} = h^{*}_{-\mathbf{q}}$, with the asterisk denoting complex conjugation. Similar expressions apply to the densities. These transformations turn the bilayer free energy surface density into a summation over independent modes, $f = \sum_{\mathbf{q}} f_{\mathbf{q}}$. For a single mode along the $x$ axis with wave number $q$, on which we shall henceforth concentrate for notational convenience, the free energy takes the form

$$f_q = \frac{1}{2} \begin{pmatrix} h_q \\ \rho^{\Delta}_q \\ \rho^{\Sigma}_q \end{pmatrix}^{T} \begin{pmatrix} \tilde{\kappa}q^4 & -2k_m q^2 d & 0 \\ -2k_m q^2 d & 2k_m & 0 \\ 0 & 0 & 2k_m \end{pmatrix} \begin{pmatrix} h_q \\ \rho^{\Delta}_q \\ \rho^{\Sigma}_q \end{pmatrix}^{*}, \tag{4.5}$$

where $\tilde{\kappa} = \kappa + 2k_m d^2$ is an effective bending rigidity.

The structure of the energy matrix $\mathbf{E}_q$ in the above expression is a consequence of the chosen variables. In terms of the normalised densities relative to the monolayer neutral planes, $\pi^{\pm} = \phi^{\pm}/\phi_0 - 1$ or the corresponding $\Delta\rho_{\phi}$ and $\pi^{\Sigma}$, the energy matrix would have been diagonal. Although these fields are advantageous when describing the thermodynamics of the bilayer, they are less appealing in a study on bilayer dynamics. Of course, both choices agree on free energy changes going with conformational fluctuations, be it with different interpretations of the bending and elastic contributions. If, for example, an initially flat bilayer is

uniformly bent into a cylinder with curvature radius $R = 1/(2H)$, the unprojected densities become $\pi^{\pm} = \pm d/R$ and acquire an elastic free energy of $2k_m d^2(2H)^2$ per unit of area, on top of the bending energy of $2\kappa_m(2H)^2$. The projected density fluctuations $\rho^{\Delta}$ and $\rho^{\Sigma}$, on the other hand, remain unchanged while the bending-induced elastic energies are implicitly accounted for by the augmented bending rigidity $\tilde{\kappa}$.

We conclude this section with three minor points. (i) As already noticed above, the bending and density terms in Eq. (4.5) are not fully decoupled: the presence of the two off-diagonal elements in $\mathbf{E}_q$ shows that a mixed contribution remains which accounts for elastic energy contributions in the bending of an asymmetric, $\rho^{\Delta} \neq 0$, bilayer. (ii) The structure factors of a tensionless bilayer are known to scale as $\langle |h_q|^2 \rangle = k_B T/\kappa q^4$, which has amply been confirmed by simulations. [28, 37, 38, 39, 40] By applying the equipartition theorem to Eq. (4.5),

$$\left\langle \begin{pmatrix} h_q \\ \rho_q^{\Delta} \\ \rho_q^{\Sigma} \end{pmatrix}^T \begin{pmatrix} h_q \\ \rho_q^{\Delta} \\ \rho_q^{\Sigma} \end{pmatrix}^* \right\rangle = k_B T \begin{pmatrix} 1/\kappa q^4 & d/\kappa q^2 & 0 \\ d/\kappa q^2 & \tilde{\kappa}/2k_m\kappa & 0 \\ 0 & 0 & 1/2k_m \end{pmatrix}, \tag{4.6}$$

one finds that this scaling law still holds. Note that the right hand sides of Eqs. (4.5) and (4.6) apply to a membrane of unit area; for a bilayer of total area $A$ the free energy gains a factor $A$ and the expectation values acquire an extra factor of $A^{-1}$. (iii) Had we endowed the monolayers with a spontaneous curvature, $c_0^{\pm}$, the bending free energies would have read $f_{\text{bend}}^{\pm} = (\kappa_m/2)(2H^{\pm} - c_0^{\pm})^2$, where $c_0^{\pm} = \pm c_0$ due to the opposite orientations of the two identical monolayers. The bilayer then still has no spontaneous curvature, while its bending rigidity would have been $\kappa = 2\kappa_m(1 - 2c_0 d)$. The remainder of the above analysis is unchanged, and offers no opportunity of determining $\kappa_m$ and $c_0$ independently.

### 4.2.2 Dynamics

Seifert and Langer[23, 24] and Evans and Yeung[16] solved the equations of motion of a bilayer using the Stokes approximation, i.e., by neglecting inertial forces and balancing driving forces with friction forces.

For the solvent at either side of the bilayer, the Stokes or creeping flow conditions read

$$\eta \nabla_{\mathbf{x}}^2 \mathbf{u}^{\pm} = \nabla_{\mathbf{x}} p^{\pm}, \tag{4.7}$$

$$\nabla_{\mathbf{x}} \cdot \mathbf{u}^{\pm} = \mathbf{0}, \tag{4.8}$$

with $\mathbf{u}^{\pm}(\mathbf{x})$ and $p^{\pm}(\mathbf{x})$ being the flow and pressure fields at $\mathbf{x} = (x, y, z)$, respectively, and $\eta$ the viscosity of the solvent. At the bilayer, which for convenience is treated as a flat boundary at $z = 0$, the two flow fields are matched by a continuous normal velocity, which obviously equals the normal velocity of the bilayer, $u_z^{\pm}(\mathbf{x}, 0) = \dot{h}(\mathbf{x})$. However, if the two monolayers are allowed to slip, the tangental velocities are discontinuous. Assuming stick boundary conditions at the solvent-bilayer interfaces, which was shown to be a realistic approximation in our earlier simulations of bilayers under a parallel shear flow, [19] one arrives at $\mathbf{u}^{\pm}(\mathbf{x}, 0) = \mathbf{v}^{\pm}(\mathbf{x})$, with $\mathbf{v}^{\pm}$ the lateral velocities of the two monolayers. The resulting flow field in the solvent can be expressed as a sum of waves which are oscillatory along the bilayer plane and exponentially decaying with the normal distance to the bilayer. [23] The stress tensors $\mathbf{T}^{\pm}$ in the liquid follow, as usual, as the sum of the hydrostatic pressure and shear terms.

The equations of motion of the bilayer read[23]

$$\frac{\delta f}{\delta h} = T_{zz}^{+} - T_{zz}^{-}, \tag{4.9}$$

$$\nabla_{\mathbf{x}} \left( \frac{\delta f}{\delta \rho^{\Delta}} \right) = \eta_s \nabla_{\mathbf{x}}^2 \left( \mathbf{v}^{+} - \mathbf{v}^{-} \right) + \left( \mathbf{T}^{+} + \mathbf{T}^{-} \right) \cdot \hat{\mathbf{e}}_z - 2b \left( \mathbf{v}^{+} - \mathbf{v}^{-} \right), \tag{4.10}$$

$$\frac{\partial \rho^{\Delta}}{\partial t} \approx -\frac{1}{2} \nabla_{\mathbf{x}} \cdot \left( \mathbf{v}^{+} - \mathbf{v}^{-} \right). \tag{4.11}$$

These equations, together with those of the liquid phases, form a complete set. In particular, no continuity equation for $\rho^{\Sigma}$ is needed, since $\rho^{\Sigma}$ does not occur in any of the above equations, nor in the free energy derivatives $\delta f / \delta h$ and $\delta f / \delta \rho^{\Delta}$, see Eq. (4.4).

The first of the above equations is obtained by balancing all normal forces, i.e., the forces within the bilayer and the difference between the liquid stresses at either side of the bilayer.[23] The left hand side denotes the change of surface free energy density upon a locally homogeneous bending of the surface. Expressing the free energy density in terms of the projected densities $\rho^{\Delta}$ and $\rho^{\Sigma}$, which remain constant during a homogeneous bending, this change can simply be calculated as the functional derivative $\delta f / \delta h$. After a Fourier transformation, the derivative $\partial f / \partial h_q^*$ is readily evaluated from Eq. (4.5), while introduction of the

solvent flow field reduces the two terms on the right hand side to $T_{zz}^{\pm} = \mp 2\eta q \dot{h}_q$. One thus arrives at the equation of motion for $h_q$.

Equation (4.10) is obtained by subtracting the tangental force balances of the upper and lower monolayers.[23] The first term on the right hand side describes viscous forces within the monolayers, slowing down the flow fields $\mathbf{v}^{\pm}$ of the amphiphiles, with $\eta_s$ the surface shear viscosity.[19, 41]. In the second term on the right hand side one recognises shear forces acting on each of the monolayers, exerted by the liquid above and below the membrane, again under the assumption that stick boundary conditions apply. As discussed by Evans and Yeung,[16] for thermally undulating bilayers at wave lengths exceeding the bilayer thickness, these first two force contributions on the right hand side are negligible compared to the third term and they are henceforth ignored. The last term on the right hand side gives a phenomenological expression for the shear force between two sliding monolayers, with $b$ denoting the friction parameter. The left hand side describes lateral forces within the monolayer resulting from gradients in the surface pressure, which in turn are caused by variations in the densities.

The last equation, Eq. (4.11), is the difference between the mass conservation equations of the two monolayers. In principle the density difference can also relax by 'flip-flops',[16] the exchanging of amphiphiles between the two monolayers, but such events are rare in the current simulations. Inserting the Fourier transform of Eq. (4.11) into the right hand side of the Fourier transform of Eq. (4.10), one obtains the equation of motion for $\rho_q^{\Delta}$.

Combining the results of the above steps, Seifert and Langer[23, 24] arrived at a coupled set of equations of motion for the height and the projected density difference,

$$\frac{\partial}{\partial t}\begin{pmatrix} h_q \\ \rho_q^{\Delta} \end{pmatrix} = -\begin{pmatrix} \tilde{\kappa}q^3/4\eta & -k_m q d/2\eta \\ -k_m q^4 d/2b & k_m q^2/2b \end{pmatrix}\begin{pmatrix} h_q \\ \rho_q^{\Delta} \end{pmatrix} \equiv -\mathbf{M}_q \begin{pmatrix} h_q \\ \rho_q^{\Delta} \end{pmatrix}. \quad (4.12)$$

Modes with different wave vectors evolve independently. The two relaxation rates $\gamma_{1,2}$ of this coupled set, where $\gamma_1 < \gamma_2$ for all $q$, are readily obtained by solving the characteristic equation of the matrix $\mathbf{M}_q$. Figure 4.1 shows these eigenvalues as functions of $q$, using the parameters of the bilayer model simulated here. By Taylor expanding the exact expressions, one recovers the two limiting regimes of the plot,

$$\gamma_1(q) \approx \begin{cases} \frac{\kappa}{4\eta}q^3 & q \ll q_c \\ \frac{k_m \kappa}{2b\tilde{\kappa}}q^2 & q \gg q_c \end{cases} \qquad \gamma_2(q) \approx \begin{cases} \frac{k_m}{2b}q^2 & q \ll q_c \\ \frac{\tilde{\kappa}}{4\eta}q^3 & q \gg q_c \end{cases}, \quad (4.13)$$

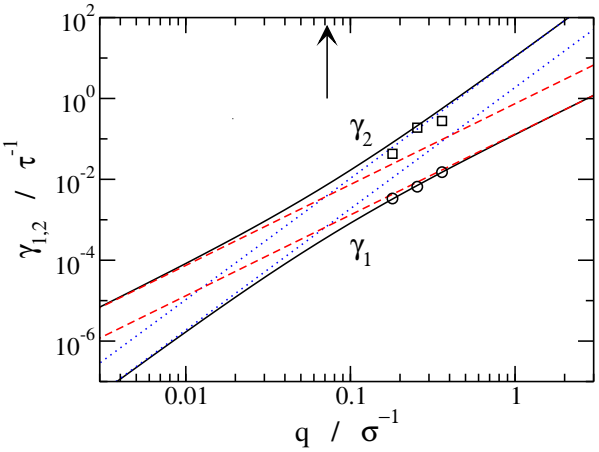


Figure 4.1: The two relaxation rates of a bilayer membrane as functions of the wave number. Solid lines represent the theory of Seifert and Langer, using the static and dynamic properties of the current CG model, dashed and dotted lines indicate the limiting regimes of Eq. (4.13), and the arrow marks the cross-over wave number $q_c$. Circles and squares denote the relaxation rates obtained by fitting the time correlations of the simulated undulations with a double-exponential function, see Fig. 4.5. An enlargement of the simulated slow relaxation rates $\gamma_1$ is presented in Fig. 4.8.

where $q_c = 2\eta k_m / b\tilde{\kappa}$ is the cross-over wave number. The eigenvectors $\mathbf{V}_{1,2}(q)$ corresponding to these eigenvalues reveal the physical characters of the two relaxation processes. At low $q$ the slow first mode describes bending relaxations slowed down by viscous dissipation in the liquid, in agreement with the classical results for a monolayer membrane,[5, 6] i.e. $\gamma_1 = \Gamma$, while the fast second mode represents diffusional relaxation of density difference variations, damped by friction between the monolayers. In the neighbourhood of $q_c$ the two eigenvectors of $\mathbf{M}_q$ gradually exchange their characters. For the high $q$ regime in which we are interested here, the slow first mode describes a density relaxation process damped by intermonolayer friction, and the fast second mode a viscously damped bending relaxation. Note that the eigenvalues of Eq. (4.13) are not simply exchanged upon crossing $q_c$, but acquire a factor of $\tilde{\kappa}/\kappa$ or its inverse. For $q \ll q_c$ the density equilibrates much faster than the undulations and

$\kappa$ acts as the bending rigidity, while at $q \gg q_c$ the density relaxes slower than the undulations and $\tilde{\kappa}$ becomes the effective bending rigidity. Because of computational limits on the maximum accessible bilayer dimensions, and hence the lowest attainable values of $q$, computer simulations of bilayer models with molecular details necessarily live in the latter regime, at best approaching $q_c$ from above.[25]

Evans and Yeung[16] derived, in their study of axially symmetric vesicles and tethers, equations of motion which are essentially identical to the above expressions. Instead of density fields, these authors used dilation fields, $\alpha^{\pm} = a^{\pm}/a_0 - 1$ with $a^{\pm}$ the area per molecule and $a_0$ its equilibrium value. The focus on curved, rather than on nearly flat surfaces, introduces a number of additional higher order curvature contributions in the normal force balance. By using the approximation $\alpha^+ - \alpha^- \approx -2\Delta\rho_\phi$ for small $\alpha^{\pm}$, and keeping only lowest order terms in $h$ and $\rho^\Delta$, one recovers the preceding equations of motion.

Having established the macroscopic equations of motion of the bilayer, the Onsager regression hypothesis[9] is finally invoked to describe the autocorrelations of thermal fluctuations around equilibrium, [27]

$$\langle h_q(t)h_q^*(0)\rangle = \langle h_q h_q^*\rangle \left[A_1^h e^{-\gamma_1 t} + A_2^h e^{-\gamma_2 t}\right], \tag{4.14}$$

$$\langle \rho_q^\Delta(t)\rho_q^{\Delta *}(0)\rangle = \langle \rho_q^\Delta \rho_q^{\Delta *}\rangle \left[A_1^\rho e^{-\gamma_1 t} + A_2^\rho e^{-\gamma_2 t}\right]. \tag{4.15}$$

The weight factors $A_1^h$ through $A_2^\rho$ are compiled by combining $\mathbf{E}_q^{-1}$ with the matrix $\mathbf{V}_q$ of eigenvectors of $\mathbf{M}_q$,

$$A_i^\alpha = \frac{1}{(E^{-1})_{\alpha\alpha}} V_{\alpha i} \sum_\beta (E^{-1})_{\alpha\beta} V_{\beta i}, \tag{4.16}$$

where $\{\alpha,\beta\} \in \{h,\rho^\Delta\}$ denote the components of the vectors and matrices, and $i \in \{1,2\}$ an ordinal number; the $q$ dependence has been dropped here for convenience. In Fig. 4.2 the four amplitudes are plotted against wave number for the bilayer model studied here, showing that the first exponential, with the largest relaxation time, has the largest amplitude. The short relaxation time and relatively small amplitude of the second exponential will complicate the detection of this mode in the simulations.

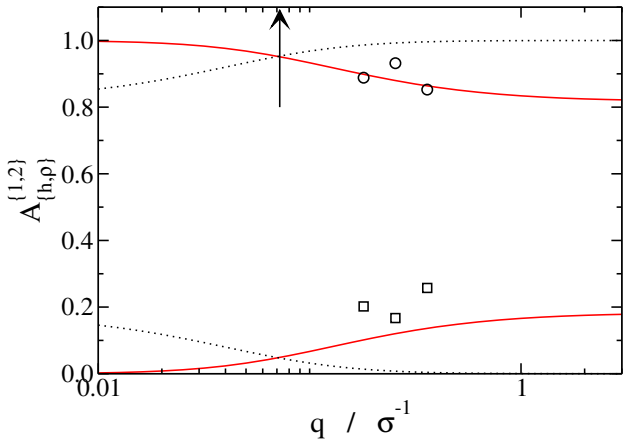


Figure 4.2: The amplitudes $A$ of the contributions of the slow (1, top) and fast (2, bottom) relaxation processes to the relaxation of the height ($h$, solid) and projected density difference ($\rho^{\Delta}$, dotted) time correlations, as calculated using Eq. (4.16). Circles and squares denote amplitudes $A_h^{1,2}$ obtained by fitting the auto correlations of the simulated undulations with a double-exponential function, see Fig. 4.5. The cross-over wavenumber $q_c$ is marked with an arrow.

## 4.3 Simulation details

The membrane and solvent are simulated [42, 43] using a coarse-grained model introduced by Goetz and Lipowsky.[44] An amphiphile is represented as a chain of one head ($h$) and four tail ($t$) particles, the solvent as loose water ($w$) particles. The non-bonded interactions are of the Lennard-Jones type, $\Phi_{\mathrm{LJ}} = 4\varepsilon[(r/\sigma)^{-12} - (r/\sigma)^{-6}]$, except for the repulsive hydrophobic interaction, $\Phi_{\mathrm{rep}} = \varepsilon(r/1.05\sigma)^{-9}$, between tail and water or head particles. All non-bonded interactions are implemented in a shifted-force fashion, hence the energy and force terminate smoothly at the cut-off distance of $2.5\sigma$. Within the amphiphiles, the particles are held together by bond interactions $\Phi_{\mathrm{bond}}(l) = 5000\varepsilon\sigma^{-2}(l-\sigma)^2$ while a bending potential straightens the molecule, $\Phi_{\mathrm{angle}}(\phi) = 2\varepsilon[1-\cos(\phi)]$, with no dihedral potential. All particles have the same mass $m$, and their number density is fixed at $\frac{2}{3}\sigma^{-3}$. The equations of motion are integrated in DL_POLY[45] using Verlet's leap-frog algorithm with a time step of $\tau/500$, where $\tau = \sqrt{m\sigma^2/\varepsilon}$ is the unit of time. A Nosé-Hoover thermostat with a relaxation time of $0.4\tau$ is employed to maintain a temperature $T = 1.35\varepsilon/k_B$. For comparison with experimental data, Goetz and Lipowsky[44] identified the tail and water particles with a $(CH_2)_3$ unit and two water molecules, respectively, yielding $\varepsilon = 2\,\mathrm{kJ/mol}$, $\sigma = 1/3\,\mathrm{nm}$ and $m = 36\,\mathrm{a.u.}$ and hence $T = 325\,\mathrm{K}$. A series of simulations with this simple CG model have revealed that its area per molecule, elastic modulus, bending rigidity [34, 37, 38, 44] and edge energy[46, 47] lie within the range covered by experimental data and other simulation studies.

It should be emphasized, however, that this computationally attractive amphiphilic model, with its single short tail, was not designed to accurately represent any particular amphiphile, nor was any effort made to tune the force field parameters to the dynamics of a bilayer. Consequently, it turns out that the time evolution of this model bilayer is considerably quicker than that of experimental bilayers, which are usually comprised of amphiphiles with two long tails. In a previous study[19] with this model we obtained for a quiescent bilayer an in-plane amphiphilic diffusion coefficient of $D = 1.8\sigma^2/\tau$ or $1.4{\cdot}10^{-5}\,\mathrm{cm^2/s}$, as compared to typical experimental values[48, 49] of $(1-25)\cdot 10^{-8}\,\mathrm{cm^2/s}$. Simulations of bilayers under perpendicular and parallel shear flows[19] yielded, respectively, a surface viscosity of $\eta_s = 20\varepsilon^{1/2}m^{1/2}\sigma^{-1}$ or $8.5{\cdot}10^{-13}\,\mathrm{Pa\,m\,s}$ and an intermonolayer friction coefficient of $b = 3.7\varepsilon^{1/2}m^{1/2}\sigma^{-3}$ or $1.4{\cdot}10^{6}\,\mathrm{Ns/m^3}$. The converted values show that the dynamics of the

coarse grained model is two to three orders of magnitude faster than that of experimental bilayers, for which $\eta_s = (1-10)\cdot 10^{-10}\,\mathrm{Pa\,m\,s}$ and $b = (1-10)\cdot 10^{8}\,\mathrm{Ns/m^3}$ are typical. [16, 18, 21, 22, 41, 50] The viscosity of the solvent, $\eta = 1.0\varepsilon^{1/2}m^{1/2}\sigma^{-2}$ or $1.3\cdot 10^{-4}\,\mathrm{Pa\,s}$, is about a quarter of that of water at this temperature. Of course, the accelerated dynamics does not in any way alter the equations of motion of the bilayer, whose validity we want to put to the test here. From a simulations point of view, a fast model with a low $b$ is actually computationally attractive as it makes it easier to achieve a total run length that well exceeds the slowest relaxation time $\gamma_1^{-1} \propto b$. Introducing the model parameters into Eq. (4.13), we find that the smallest wave number commensurate with the box dimensions, $q \approx 0.18\sigma^{-1}$, is more than double the cross-over wavenumber $q_c = 0.07\sigma^{-1}$. The relaxation times at this wavenumber, which are the slowest relaxation times of the bilayer, are then estimated at $\gamma_1^{-1} \approx 230\tau$ and $\gamma_2^{-1} \approx 17\tau$, and lie within the capabilities of current simulations.

The simulated bilayer counts $N = 1152$ amphiphiles and lies parallel to the square ground plane of the periodic box with sides $L_\parallel$. Surrounding the bilayer are 10 800 solvent particles, making the box height $L_\perp$ sufficiently large for the pressure tensor to become isotropic near the middle of the solvent layer.[44] Because Eq. (6.1) is based on the assumption that the monolayer densities are free to relax to their equilibrium value, $\langle\phi^{\pm}\rangle = \phi_0$, the bilayer must be prepared in a tension-less state. We therefore varied the box dimensions, at constant total volume, to nullify the surface tension $\tau_s = L_\perp(p_\perp - p_\parallel)$, with $p_\perp$ and $p_\parallel$ the pressures on the box faces perpendicular and parallel to the bilayer respectively. A calculation of the structure factors, to be discussed below, independently confirms that the bilayer is indeed tension-less for $L_\parallel = 34.9\sigma$. In order to test for system size dependencies, a limited number of simulations were ran with a 2048 amphiphile tension-less bilayer surrounded by 19 200 solvent particles.

The positions $\mathbf{x}_i = (\mathbf{x}_i, z_i)$ of the $N_a$ amphiphilic particles in the simulated bilayer do not constitute a smooth bilayer plane $h(\mathbf{x})$, nor smooth density distributions, and some manipulations are required to extract the appropriate Fourier coefficients from these coordinates. One route is provided by a direct Fourier transformation of the particle coordinates,[38]

$$h_{\mathbf{q}} = \frac{1}{N_a}\sum_{i=1}^{N_a} z_i e^{-\mathbf{q}\cdot\mathbf{x}_i}. \tag{4.17}$$

This approach can only be applied with confidence when the particles are distributed evenly along the groundplane, a condition that is met here as the undulations and the density fluc-

tuations are relatively minor for a small tension-less patch of bilayer. The corresponding expression for the monolayer densities reads

$$\phi_{\mathbf{q}}^{\pm} = \frac{1}{L_{\parallel}^2} \sum_{i=1}^{N_a^{\pm}} e^{-\mathbf{q}\cdot\mathbf{x}_i}. \tag{4.18}$$

Note that this expression, being based on the approximate bilayer area $L_{\parallel}^2$, neglects variations in the local surface area resulting from the undulations of the membrane. The curvature corrections required for the subsequent conversion into $\psi_{\mathbf{q}}^{\pm}$ are not readily implemented either. Although both omitted contributions to $\psi_{\mathbf{q}}^{\pm}$ are expected to be relatively small, as the total curved surface area of the bilayer exceeds the ground plane area only by a modest 2.5% in our simulations,[34] their neglect in a density *difference* calculation has far greater consequences. We return to the merits and demerits of Eq. (4.18) in Section 4.4.2.

To include the aforementioned small but vital contributions in the Fourier transformations, we divided the $xy$-plane into $M \times M$ square grid cells, identifiable by their integer coordinates $\mathbf{m} = (m_x, m_y)$. The height $h_{\mathbf{m}}$ of the bilayer in the $\mathbf{m}^{th}$ cell was calculated as the average $z$ coordinate of all amphiphilic particles in that cell, and a straightforward Fourier transformation yielded $h_{\mathbf{q}}$. The monolayer densities $\phi_{\mathbf{m}}^{\pm}$ were obtained by dividing the counted number of particles per cell by the monolayer area per cell $a_{\mathbf{m}}^{\pm}$. Because the areas that follow from triangulation of the heights $h_{\mathbf{m}}$ are out of phase with the cell boundaries used in the particle counts, we made use of an auxiliary set of heights $h'_{\mathbf{m}}$ calculated on a grid that was shifted relative to the primary grid by half a cell size in the $x$ and $y$ directions. In order to arrive at $\psi_{\mathbf{m}}^{\pm}$, several steps were made. The equilibrium monolayer density $\phi_0$ was obtained as the total number of amphiphilic particles divided by the averaged sum of all areas $a_{\mathbf{m}}^{+}$ and $a_{\mathbf{m}}^{-}$. Next, the heights $h_{\mathbf{m}}$ were analysed by a 9-points numerical differentiation scheme[51] to establish the mean curvature $H_{\mathbf{m}}$ per cell. The projection of the densities furthermore require the distance $d$ between the midsurface of the bilayer and the neutral surfaces of the monolayers. Since there is no readily available technique for establishing $d$, we assumed this distance to be equal to half the monolayer thickness, i.e., a quarter of the bilayer thickness. Using the average cross-membrane head-to-head distance as a measure for the bilayer thickness, we arrive at $d = 1.75\sigma$. Finally, the grid of projected densities is Fourier transformed and analysed. Of course, periodic boundary conditions were used throughout these calculations. The assignment of the amphiphiles to the two monolayers was redetermined every timestep,

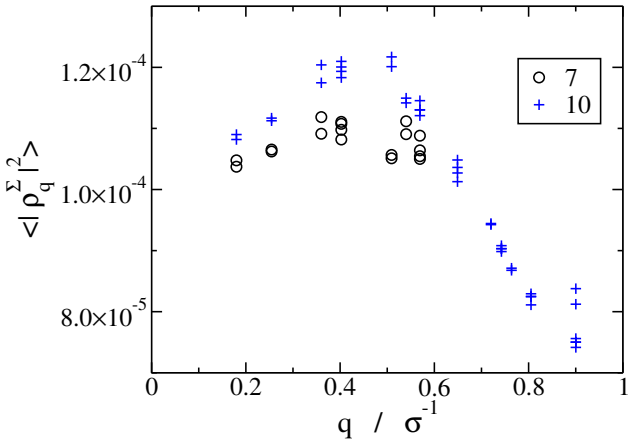


Figure 4.3: Structure factors of the projected sum density fluctuation $\rho^{\Sigma}$ as a function of the wave number, calculated by subdividing the ground plane of the simulations box into $M^2 = 49$ (circles) or 100 (pluses) grid cells.

to correct for the rare exchanges of amphiphiles between the layers, by using a clustering routine[42] based on the distances between the head particles.

## 4.4 Results

### 4.4.1 Statics

The main objectives in this subsection are to establish a proper grid size for the Fourier transformations and to assess the impact of the grid procedure, where possible by comparison against previous off-lattice calculations. We also determine the density compressibility of the monolayers.

While smaller grid cells (i.e., larger $M$) allow one to probe smaller length scales, the concomitant reduction in the number of particles per cell increases the impact of statistical noise on the data. Figure 4.3 shows the sum density structure factors $\langle|\rho_q^{\Sigma}|^2\rangle$ for $M = 7$ and $M = 10$, with on average 59 or 29 amphiphilic particles per cell, respectively. In the

low wavenumber regime that we are interested in here, the two data sets are levelling off at about the same value, in agreement with the prediction of Eq. (4.6). The weak $M$ dependence in this graph probably results from the Fourier transformation of grid-based averages,[34] compounded with noise introduced by the assignment of the particles to the grid cells. The dynamical sum density structure factors, to be discussed in the next section, are also very similar for $M = 7$ and 10, suggesting that both gridsizes are acceptable for our purposes. Introducing the extrapolated value at low $q$ of $\langle|\rho_q^{\Sigma}|^2\rangle \approx 1 \cdot 10^{-4}$ into Eq. (4.6), we obtain a monolayer compressibility of $k_m \approx 5.5\varepsilon\sigma^{-2}$ or about 160 mJ/m$^2$. Additional simulations with a 2048 amphiphile bilayer, in order to reach a lower $q$, confirmed this value of $k_m$.

By increasing the number of grid cells, the range of accessible wavenumbers becomes larger and a decaying tail develops which is attributed to protrusions,[52] i.e., amphiphiles sticking out of the smoothly undulating bilayer shape. At the same time, the local maximum near $q \approx 0.5\sigma^{-1}$ becomes more pronounced. Similar plots, with varying degree of prominence of the local maximum, have been reported by a number of authors[28, 39, 40] for the thickness or peristaltic modes of a bilayer, which for a nearly incompressible bilayer are strongly related to the sum density modes.

The compressibility can also be derived from the probability distribution $P(\phi_{\mathbf{m}}^{\pm})$ of the monolayer densities per grid cell. Following Eq. (6.1), the probability of finding a cell with a given curvature, density and area is proportional to the Boltzmann factor $\exp\left[\frac{-f(H_{\mathbf{m}},\phi_{\mathbf{m}}^{\pm})a_{\mathbf{m}}^{\pm}}{k_BT}\right]$. Since the variation in the cell areas is small relative to the fluctuations of the other two variables, it seems reasonable to make the approximation $a_{\mathbf{m}}^{\pm} = \langle a_{\mathbf{m}}^{\pm}\rangle$. Using the independence of bending and elastic free energies, one then arrives at

$$P(\phi_{\mathbf{m}}^{\pm}) \propto \exp\left[-\frac{1}{k_BT}\frac{k_m}{2\phi_0^2}\left(\phi_{\mathbf{m}}^{\pm}-\phi_0\right)^2\langle a_{\mathbf{m}}^{\pm}\rangle\right]. \tag{4.19}$$

Fitting the histogram presented in Fig. 4.4 with this Gaussian yields $k_m = 5.5\sigma\varepsilon^{-2}$, in agreement with the above calculated value.

Simulation studies of the mechanical properties of bilayers are usually aimed at the calculation of the bilayer area compressibility, [28, 37, 38, 39, 40, 44] $K_A = a_0 d\tau_s/da$. Several studies[38, 39] have revealed that the traditional expression for the area, $a = 2L_{\|}^2/N$, results in a system-size ($N$) dependent effective area compressibility, $K_{A\|}$, due to the neglect of the excess surface area stored in the undulations, and alternative calculation methods have been

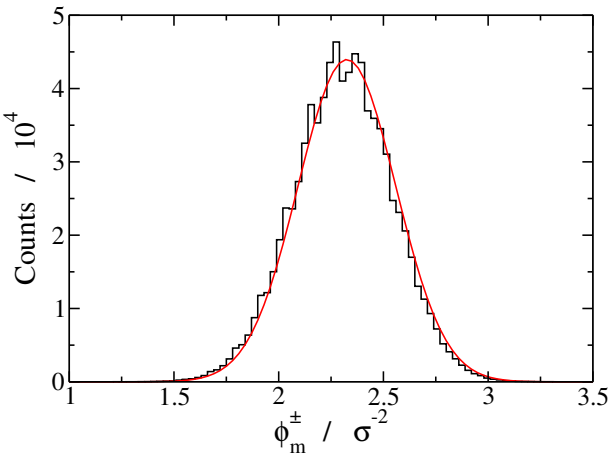


Figure 4.4: Probability distribution of the monolayer densities per grid cell, calculated using $M^2 = 49$ grid cells. The smooth line is a fit with the Gaussian of Eq. (4.19).

proposed.[34] This effect is also encountered in experiments, [33, 35, 36] where for large tension-less vesicles the effective area compressibility approaches zero. It is reassuring then to find that the two employed system sizes yield matching estimates for $k_m$. For small undulations around equilibrium one readily shows $K_A = 2k_m$, hence the above results correspond to $K_A = 11\varepsilon\sigma^{-2}$. This value well exceeds the effective elastic modulus $K_{A\|} = 7.6\varepsilon\sigma^{-2}$ of the 1152 amphiphile bilayer, but does not quite reach the previously reported value of $K_A \approx 13\varepsilon\sigma^{-2}$ for this CG model. [34]

Miao *et al.*[32] suggested that the effective compressibility, rather then the intrinsic compressibility, should enter the equations of motion of the bilayer, Eq. (4.12). The slow relaxation rate $\gamma_1$ of our model changes by a mere 10% when inserting the aforementioned extremes of the compressibility; a similar impact is also achieved by a 10% variation of the distance $d$. Given the uncertainty in the determination of the latter, it is obvious that the current simulations do not permit definitive conclusions as to which compressibility should be used.

For completeness, we note that the bending rigidity of the bilayer is readily derived by a Fourier transformation of the height undulations of the bilayer, [37] using either the grid-

based approach or the direct transformation of Eq. (4.17). The structure factors are observed to decay as $q^{-4}$ for wavenumbers upto about $0.5\sigma^{-1}$, in good agreement with the prediction of Eq. (4.6) for a tensionless state, followed by a slower decay at higher wavenumbers due to protrusions. We refer the reader to Fig. 4 of Ref.[34] for a plot made by direct Fourier transformation; the grid-based results are very similar, but truncated in $q$-space due to the chosen grid size $M$. The bending rigidity is established at $7\varepsilon$, which amounts to just over $5k_BT$.

As a final consistency test, we have calculated the remaining diagonal element of Eq. (4.6), i.e., the density difference structure factors. By averaging over the lowest wavenumbers in the 1152 and 2048 amphiphile systems, we find $k_m\kappa/\tilde{\kappa} = 0.92\varepsilon\sigma^{-2}$ and $1.03\varepsilon\sigma^{-2}$, respectively, with a standard deviation of 15%. These values compare well with the value of $0.95\varepsilon\sigma^{-2}$ obtained from a direct calculation of $k_m\kappa/\tilde{\kappa}$ using the aforementioned values of $\kappa$ and $k_m$ in combination with $d = 1.75\sigma$. Note that this result should not be interpreted as a confirmation of the assumed distance $d$ between midsurface and neutral surface because the mathematical manipulations leading from Eq. (6.1) to Eq. (4.6), aside from a few truncated Taylor expansions, hold true for any chosen value of $d$. Having validated the evaluations of the Fourier transforms $h_q$ and $\rho_q^{\Delta}$, we now proceed to study the dynamics of the bilayer.

### 4.4.2 Dynamics

The shear viscosity of a liquid is routinely calculated in molecular dynamics simulations from the off-diagonal elements of the stress tensor in a simulation box exposed to a simple shear flow.[42] A similar approach can be used to determine the rheological properties of the bilayer, to wit, the in-plane or surface shear viscosity and the intermonolayer friction coefficient, by imposing perpendicular and parallel shear flows, respectively, on the bilayer and the surrounding solvent.[19] The resulting numerical values have been mentioned already in Section 6.3. In combination with the static properties discussed in the previous subsection, they enabled us to calculate the theoretical relaxation rates and amplitudes depicted in Figs. 4.1 and 4.2. We have now arrived at the point where we can put these predictions to the test, by comparing them against actual simulation results.

The time correlations of the height undulations are depicted in Fig. 4.5 for the six smallest wavevectors matching the box dimensions. In view of the expected scaling behaviour at long

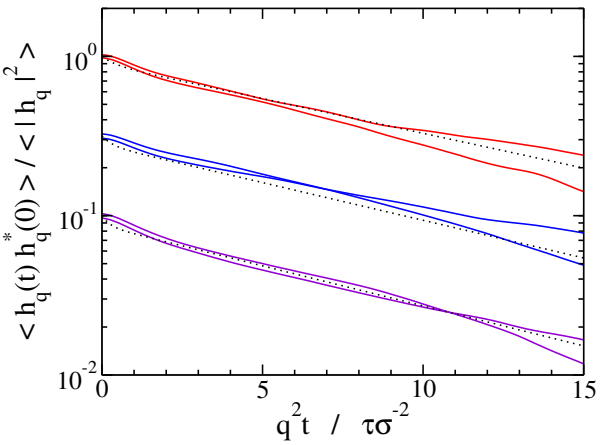


Figure 4.5: Normalised undulation auto correlation functions (solid) for the six smallest wave vectors commensurate with the box dimensions, i.e., $q = 0.18\sigma^{-1}$ (top), $0.25\sigma^{-1}$ (middle, shifted down by half a decade) and $0.36\sigma^{-1}$ (bottom, shifted down by one decade). The dotted lines are calculated by Eq. (5.8), using the exact relaxation rates and amplitudes of Figs. 4.1 and 4.2, respectively.

times, see Eq. (4.13), we have scaled the time axis by $q^2$. The linear-log plot shows that the resulting lines are all running reasonably parallel, thus confirming that the decay rate of the slow relaxation process scales nearly quadratically with the wave number. Similar slopes are also displayed by the theoretical curves (dotted lines) calculated by Eq. (5.8), using the exact relaxation rates and amplitudes, implying that the simulated decay rates closely match the $\gamma_1$ derived for the slow relaxation mechanism. Furthermore, the overall good agreement between theory and simulation, with the largest relative deviation occurring for the two wavevectors running diagonally through the box, also lends support to Eq. (4.16) for the amplitude $A_1^h$. For the chosen wavenumbers, the decay of the undulations is thus seen to be dominated by intermonolayer friction.

The enlargement of Fig. 4.5 in Fig. 4.6 shows that, unlike the long time behaviour, the simulated decay on the short $\gamma_2^{-1}$ time scale deviates from the predicted decay. An initial deviation is not entirely unexpected, however, because Onsager's regression hypothesis is known

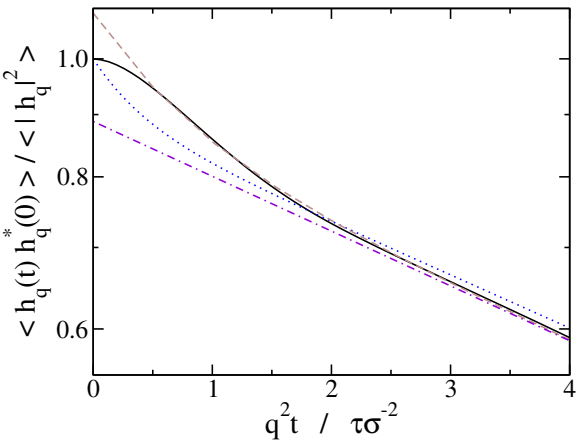


Figure 4.6: The short-time behaviour of the time correlation of the undulations (solid), averaged over the two wave vectors with the smallest wave number matching the box dimensions, $q = 0.18\sigma^{-1}$. A double exponential fit is shown as a dashed line, with the slow mode of this fit represented by the linear dash-dotted line. The dotted line is the theoretical prediction, Eq. (5.8).

not to hold on transient time scales.[9] Using time reversal symmetry, one readily proves that the initial slope of the time correlation function must be zero, as is indeed observed for the simulation data, and hence some time must elapse before the theoretical double exponential decay can set in. But the fast mode of Eq. (5.8) has nearly completed its decay to zero by the time theory and simulation coalesce, after some 20 to 50 $\tau$ depending on $q$. By fitting the time correlations directly with double exponential functions, using the two relaxation rates and two amplitudes as fit parameters, it nevertheless is possible to make a rough estimate of the fast relaxation rate. In Fig. 4.1 we see that the fast rates compare surprisingly well with theory; as discussed before, the agreement for the slow mode is very pleasing. The fitted amplitudes for the slow modes are in line with the numerical values of $A_1^h$, see Fig. 4.2, while it is obvious from the fit of Fig. 4.6 that the amplitudes of the fast process overestimate $A_2^h$.

The Fourier coefficients of the undulations were calculated twice, using both the direct method of Eq. (4.17) and the more involved grid-based method outlined in Section 6.3, but we

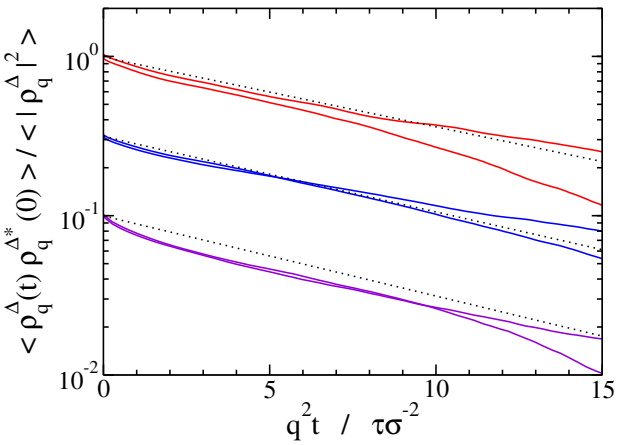


Figure 4.7: Simulated (solid) and theoretical (dotted) time correlation functions of the projected density difference. See also Fig. 4.5.

found no significant differences between the two. On the other hand, the density difference time correlation proved much more sensitive to the details of the calculation. The simplest approach is to treat the bilayer as a flat plane with lateral density variations, i.e., ignoring the undulations altogether, in which case $\rho_q^{\Delta} = (\phi_q^+ - \phi_q^-)/2\phi_0$ with $\phi_q^{\pm}$ given by the direct Fourier transformation of Eq. (4.18). The resulting time correlations, however, show little resemblance to the theoretical predictions of Eq. (4.15) and rapidly drop by nearly two orders of magnitude before being engulfed in the background noise. Relaxation times obtained by fitting these transient decays range between 4 and 12 $\tau$, and although of the same order as $\gamma_2^{-1}$, they do not support any scaling law in $q$.

In order to make a fair comparison with theory, we have analysed the data again using the elaborate grid method outlined in Section 6.3. The ensuing time correlations are plotted in Fig. 4.7 for $M = 7$, were the time axis is again scaled by $q^2$; increasing $M$ to 10 hardly affects the plot. The slowly exponentially decaying lines run nearly parallel to oneanother for all six wavevectors, and their slopes are in good agreement with the predicted relaxation rate $\gamma_1$. The fast initial decay by some 10%, and its non-zero initial slope, are probably due to the strict, yet fairly arbitrary assignment of the amphiphilic particles to the grid cells. In

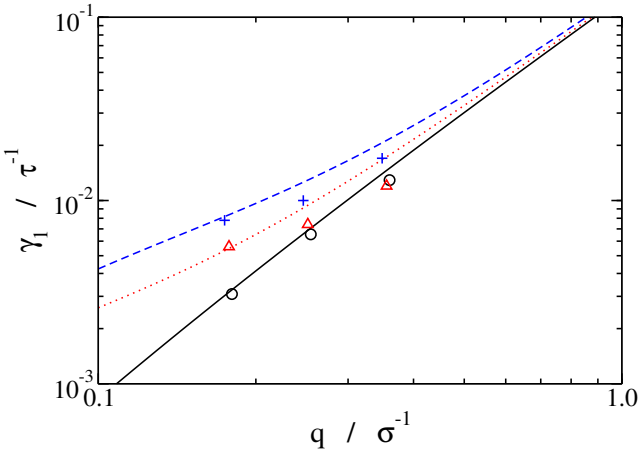


Figure 4.8: The slow relaxation rates $\gamma_1$ of a tension-less bilayer (solid line and circles), of a bilayer under 2.6% stretch (dotted line and triangles) and of a bilayer under 6.7% stretch (dashed line and pluses), as functions of the wave number. The lines are calculated using the theory described in the appendix, the markers are obtained by fitting the simulated time correlations of the undulations for the three smallest wave numbers.

summary, both the undulations and the density difference relax with the anticipated slow rate $\gamma_1$, but because of the necessity of an intricate grid-based calculation in the latter case, we recommend using the undulations when establishing the relaxation rates.

### 4.4.3 Stretched bilayers

Simulations of stretched membranes indicate that the slow relaxation rate is fairly sensitive to the surface tension. Upon increasing the ground plane area of the box by some 2.6%, exposing the bilayer to a tension of $\tau_s = 0.21\varepsilon/\sigma^3$, the relaxation rate $\gamma_1$ of the smallest wavenumber rises by about two-thirds. At an even higher 6.7% elongation, corresponding to $\tau_s = 0.54\varepsilon/\sigma^3$, the rate has increased to nearly 2.5 times its original value. A possible explanation for the increase of $\gamma_1$ might be that the tension alters the structure of the bilayer, for instance by reducing the undulations or the extent of interdigitation of the opposing tails, which in turn could reduce the intermonolayer friction coefficient. A direct measurement

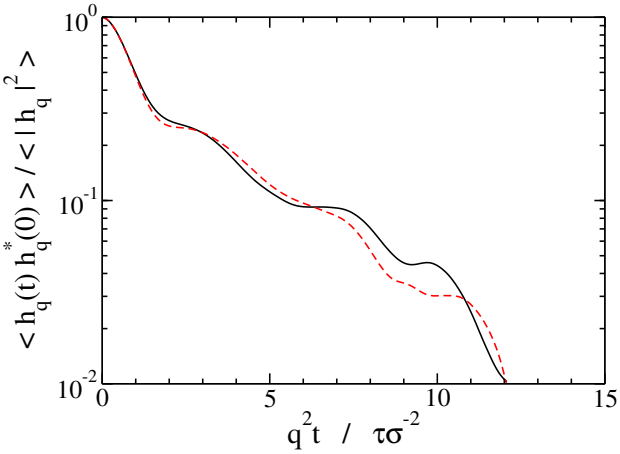


Figure 4.9: Normalised undulation auto correlation functions for the two smallest wave vectors commensurate with the box dimensions, $q = 0.17\sigma^{-1}$, for a bilayer stretched by 6.7%. A clear oscillatory contribution is visible, which is not observed for the tensionless bilayer of Figs. 4.5 and 4.6.

of $b$ by simulations of stretched bilayers under parallel shear[19] showed that this is not the case. The inclusion of a small surface tension in the derivation of Section 4.2 is fairly straightforward, though a bit laborious – we have deferred this derivation to the appendix. After these modifications, the predicted tension-dependent relaxation rates $\gamma_l$ are again in reasonable agreement with the simulation results, especially for the lowest wave number, as illustrated by Fig. 4.8. Interestingly, the simulated time correlations at the highest tension display a small oscillatory component superimposed on the slow decay, see Fig. 4.9, similar to that observed by Pott and Méléard[22] for undulating tense vesicles. To eliminate thermal noise as a possible source of the oscillations, this simulation was extended to $10^5\,\tau$ ($\gamma_l t_{\mathrm{simu}} \approx 500$), but the fluctuations persisted. An oscillation is of course not captured by the current linear equations of motion, but requires an extension of the theory to higher order.

## 4.5 Discussion and conclusions

We have performed molecular dynamics simulations of thermally fluctuating tension-less and stretched bilayers, using a coarse grained amphiphilic model. The time correlations of the undulations and of the monolayer density difference were found, see Figs. 4.5 and 4.7, to agree well with an intermonolayer friction dominated relaxation process, as predicted by Seifert and Langer[23, 24] for these relatively short length scales. We want to emphasize that the theoretical curves appearing in these plots are not fitted, but are calculated from elastic and dynamical properties established in independent equilibrium and non-equilibrium simulations. Only one parameter could not be determined beforehand, to wit, the distance $d$ between the neutral surface of the monolayers and the midsurface of the bilayer, which we judiciously choose to be half the monolayer thickness. Because of the good quantitative agreement, it is tempting now to extract a value for $d$ by fitting the theory to the simulated relaxation rates. The 3% higher value thus obtained confirms our choice, and lies well within the physically acceptable range. This result for a simple amphiphile of five similarly sized beads does, of course, not imply that the neutral surface will always lie in the middle of the monolayer. Furthermore, in actuality $d$ need not be a constant but is more likely to fluctuate with the peristaltic motions of the membrane. The indeterminacy of $d$ complicates the extraction of an intermonolayer friction coefficient from the relaxation rates, which might be alleviated by using[22] $b = \kappa k_m q^5/8\eta\gamma_1\gamma_2$ if both rates can be measured accurately for a tension-less membrane. Bilayers under tension are also well described by the theory, except for a small superimposed oscillatory contribution which still awaits an explanation.

Stacks of membranes posses an undulation mode whose relaxation rate[13, 23, 26] $\gamma_s \approx (\tilde{\kappa}/2\eta l)q^2$ is inversely proportional to the inter-membrane distance $l$. In order to be sure that our relaxation times are not unduly influenced by the periodicity of the simulation box in the direction perpendicular to the bilayer, we have also performed simulations of a 1152 amphiphile bilayer in a box with twice the original height, retaining the overall number density of $\frac{2}{3}\sigma^{-3}$. The relaxation rates differed slightly from those of the original box, but certainly not enough to support a $1/l$ dependence of $\gamma_1$ or $\gamma_2$. We conclude, therefore, that our simulated relaxation rates are those of a single freely floating membrane.

Having confirmed the theory on a simplified coarse-grained model, is it instructive to see what its implications are for a realistic membrane. Based on the typical experimen-

tal values[16, 35] $\kappa = 4 \cdot 10^{-20}\,\mathrm{J}$, $k = 250\,\mathrm{mN/m}$, $\eta = 10^{-3}\,\mathrm{Pa\,s}$, $b = 10^{8}\,\mathrm{Ns/m^3}$, and an estimated $d \approx 1\,\mathrm{nm}$, we expect a cross-over wavenumber of about $q_c = 8.6\mu\mathrm{m}^{-1}$. Since most experiments sample smaller wavenumbers, they are in the regime where the membrane predominantly relaxes through viscous dissipation in the solvent. This process is described by both the classical and the current theory, $\gamma_1 = \Gamma \propto q^3$ for $q \ll q_c$. Molecular dynamics simulations using a fully atomistic or a coarse grained model commonly encompass some 1000 amphiphiles, corresponding to[28] $q \approx 0.35\,\mathrm{nm}^{-1}$, and therefore relax mainly by intermonolayer friction. The relaxation times at this particular wavenumber are estimated at $\gamma_1^{-1} \approx 0.1\mu\mathrm{s}$ and $\gamma_2^{-1} \approx 0.3\,\mathrm{ns}$, where the former timescale exceeds most simulations to date. This leads us to conclude that the intermonolayer friction coefficient is best calculated by non-equilibrium simulations, i.e., by enforcing a velocity difference between the monolayers and measuring the corresponding friction force.[19] These driven simulations also have the advantage of not relying on an estimated value for $d$. We furthermore note that the scaling law for the structure factors, $\langle |h_q|^2 \rangle = k_B T / \kappa q^4$, as commonly used to determine the bending rigidity $\kappa$, only applies if the average is taken over a time scale well in excess of the slowest relaxation time $\gamma_1^{-1}$. This criterium is not easily met in simulations of bilayer patches large enough to display undulations, and consequently the calculated bending rigidity will often lie intermediate between the intrinsic bending rigidity $\kappa$ and the effective bending rigidity $\tilde{\kappa}$. In these cases, a free-energy calculation can be used to determine the bending rigidity.[38] An accurate estimate of the intermonolayer friction coefficient is therefore not only interesting by itself, as a key parameter in a study on bilayer dynamics, but also because of its indirect, and hitherto largely unappreciated, consequences for the calculation of bilayer bending rigidities, and possibly also other static properties, by molecular dynamics simulations.

## 4.6 Appendix: bilayer under stress

In this appendix, we outline the changes required to extend the theory of Section 4.2 to bilayers under tension. The main difference is in the free energy density of the stretched bilayer,[53] which will be derived here from the Helfrich theory, see Eq. (6.1). We start by

introducing $\bar{\phi} = N/(2A)$, the mean surface density of the monolayers for a bilayer with a total curved midsurface area $A$. Note that this area and $\bar{\phi}$ depend on the configuration $\{h_{\mathbf{q}}\}$ of the bilayer, while the average $\langle\bar{\phi}\rangle$ is a function of the box size $L_{\|}$ only, and hence of the tension. Since experimental bilayers will rupture when elongated by about 3%,[46, 54] we will assume that $\bar{\phi}$ is only slightly smaller than $\phi_0$. Repeating the steps of Section 4.2.1, the free energy density is then expressed as

$$f = \sum_{\mathbf{q}} f_{\mathbf{q}} + 2\frac{k_m}{2\phi_0^2}(\bar{\phi} - \phi_0)^2. \tag{4.20}$$

The $f_{\mathbf{q}}$, which are still given by Eq. (4.5) after redefining the projected sum density fluctuations as $\rho^{\Sigma} = (\psi^{+} + \psi^{-} - 2\bar{\phi})/\phi_0$, account for local density fluctuations around $\bar{\phi}$, while the last term in Eq. (4.20) results from the global reduction of the mean density from $\phi_0$ to $\bar{\phi}$ under stress. Next, we Taylor expand the latter term around the average $\langle\bar{\phi}\rangle$, and use a Hookean law for the tension, $\tau_s = k(\phi_0 - \langle\bar{\phi}\rangle)/\phi_0$, to arrive at the first step in

$$\frac{k}{2\phi_0^2}(\bar{\phi} - \phi_0)^2 \approx \tau_s\frac{\bar{\phi}}{\phi_0} + c_1(L_{\|}) \approx \tau_s\sum_{\mathbf{q}} q^2 h_{\mathbf{q}}^2 + c_2(L_{\|}). \tag{4.21}$$

In the second step, the area $A$ has been Taylor expanded to lowest order in the undulation amplitudes, and we made use of the approximation $A_0 \approx L_{\|}^2$ valid for small system sizes and small tensions. The $c_1$ and $c_2$ collect terms that are independent of the configuration; their contribution to the free energy may be neglected when analysing membranes with fixed $L_{\|}$. We thus see that the global elasticity term in Eq. (4.20) approximately reduces to an additional contribution $\tau_s q^2 h_{\mathbf{q}}^2$ for every $f_{\mathbf{q}}$. The implication for Eq. (4.5) is that the top-left element of the energy matrix $\mathbf{E}_q$ now reads $\tilde{\kappa}q^4 + \tau_s q^2$, while all other elements of that matrix remain unchanged.[53] Physically, these contributions express that increasing $h_{\mathbf{q}}$ enlarges the area of the membrane, which at fixed system size $N$ and fixed groundplane area $L_{\|}^2$ results in a change of the elastic energy. One readily verifies that the equipartition theorem now recovers the well-known dispersion relation $\langle|h_q|^2\rangle = k_B T/(\kappa q^4 + \tau_s q^2)$ for a membrane under tension.[28, 34, 55] Inserting this energy matrix into the otherwise unchanged equations of motion of Section 4.2.2, and proceeding along the lines of that section, one readily recovers the modified characteristic expression for the relaxation rates. At the wave numbers accessible by simulations, the surface tension is found to increases the relaxation rate $\gamma_1$ of the slow relaxation process, see Fig. 4.8. While the high $q$ limiting rate laws appearing in Eq. (4.13)

are not affected by the tension, the low $q$ limiting rate laws change into $\gamma_1 = (\tau/4\eta)q$ and $\gamma_2 = (k_m/4b)q^2$.

# Bibliography

[1] L. Stryer. *Biochemistry*. W. H. Freeman and Comp., New York, NY, 4 edition, 1995.

[2] W. M. Becker and D. W. Deamer. *The world of the cell*. Benjamin/Cummings Publishing Company, Redwood City, CA, 1991.

[3] W. Helfrich. *Z. Naturforsch. C*, 28:693, 1973.

[4] S. A. Safran. *Statistical Thermodynamics of Surfaces, Interfaces and Membranes*. Addison-Wesley, Reading, MA, 1994.

[5] L. Kramer. Theory of light scattering from fluctuations of membranes and monolayers. *J. Chem. Phys.*, 55:2097–2105, 1971.

[6] F. Brochard and J.F. Lennon. *J. Phys. (Paris)*, 11:1035, 1975.

[7] M. B. Schneider, J. T. Jenkins, and W. W. Webb. *J. Phys. (Paris)*, 45:1457, 1984.

[8] S. T. Milner and S. A. Safran. Dynamical fluctuations of droplet microemulsions and vesicles. *Phys. Rev. A*, 36:4371–4379, 1987.

[9] D. Chandler. *Introduction to modern statistical mechanics*. Oxford University Press, New York, NY, 1987.

[10] H. P. Duwe and E. Sackmann. Bending elasticity and thermal excitations of lipid bilayer vesicles: modulation by solutes. *Physica A*, 163:410–428, 1990.

[11] P. Méléard, M. D. Mitov, J. F. Faucon, and P. Bothorel. *Europhys. Lett.*, 11:355, 1990.

[12] A. G. Zilman and R. Granek. Undulations and dynamic structure factor of membranes. *Phys. Rev. Lett.*, 77:4788–4791, 1996.

[13] É. Freyssingeas, D. Roux, and F. Nallet. Quasi-elastic light scattering study of highly swollen lamellar and "sponge" phases. *J. Phys. II France*, 7:913–929, 1997.

[14] G. Althoff, D. Frezzato, G Kothe, G. J. Moro, M. Vilfan, I. Vilfan, O. Stauch, and R. Schubert. Transverse nuclear spin relaxation induced by shape fluctuations in membrane vesicles. theory and experiments. *Mol. Cryst. Liq. Cryst.*, 394:93–106, 2003.

[15] E. Evans, A. Yeung, R. Waugh, and J. Song. Dynamic coupling and nonlocal curvature elasticity in bilayer membranes. *Springer Proceedings in Physics*, 66:148–153, 1992.

[16] E. Evans and A. Yeung. Hidden dynamics in rapid changes of bilayer shape. *Chem Phys. Lipids*, 73:39–56, 1994.

[17] R. Dimova, U. Seifert, B. Pouligny, S. Förster, and H. G. Döbereiner. Hyperviscous diblock copolymer vesicles. *Euro. Phys. J. E*, 7:241–250, 2002.

[18] Y. A. Chizmadzhev, D. A. Kumenko, P. I. Kuzmin, L. V. Chernomordik, J. Zimmerberg, and F. Cohen. Lipid flow through fusion pores connecting membranes of different tensions. *Biophys. J.*, 76:2951–2965, 1999.

[19] S. A. Shkulipa, W. K. den Otter, and W. J. Briels. Surface viscosity, diffusion, and intermonolayer friction: simulating sheared amphiphilic bilayers. *Biophys. J.*, 89:823–829, 2005.

[20] J.S. Bonifacino and B.S. Glick. *Cell*, 116:153, 2004.

[21] R. Merkel, E. Sackmann, and E. Evans. *J. Phys. (Paris)*, 50:1535, 1989.

[22] T. Pott and P. Méléard. The dynamics of vesicle thermal fluctuations is controlled by intermonolayer friction. *Europhys. Lett.*, 59:87–93, 2002.

[23] U. Seifert and S. A. Langer. Viscous modes of fluid bilayer membranes. *Europhys. Lett.*, 23:71–76, 1993.

[24] U. Seifert and S. A. Langer. Hydrodynamics of membranes: the bilayer aspect and adhesion. *Biophys. Chem.*, 49:13–22, 1994.

[25] S. A. Shkulipa, W. K. den Otter, and W. J. Briels. Thermal undulations of lipid bilayers relax by intermonolayer friction at submicrometer length scales. *Phys. Rev. Lett.*, 96:178302, 2006.

[26] W. Pfeiffer, S. König, J. F. Legrand, T. Bayerl, D. Richter, and E. Sackmann. Neutron spin echo study of membrane undulations in lipid multibilayers. *Europhys. Lett.*, 23:457–462, 1993.

[27] U. Seifert. Configurations of fluid membranes and vesicles. *Adv. in Phys.*, 46:13–137, 1997.

[28] E. Lindahl and O. Edholm. Mesoscopic undulations and thickness fluctuations in lipid bilayers from molecular dynamics simulations. *Biophys. J.*, 79:426–433, 2000.

[29] T. Takeda, Y. Kawabata, H. Seto, S. Komura, S.K. Ghosh, M. Nagao, and D. Okuhara. Neutron spin-echo investigations of membrane undulations in complex fluids involving amphiphiles. *J. Phys. Chem. Solids*, 60:1375–1377, 1999.

[30] A. Yeung and E. Evans. Unexpected dynamics in shape fluctuations of bilayer vesicles. *J. Phys. II France*, 5:1501–1523, 1995.

[31] I. Bivas, P. Méléard, I Mircheva, and P. Bothorel. Thermal shape fluctuations of a quasi spherical lipd vesicle when the mutual displacements of its monolayers are taken into account. *Colloids and Surfaces A*, 157:21–33, 1999.

[32] L. Miao, M. A. Lomholt, and J. Kleis. Dynamics of shape fluctuations of quasi-spherical vesicles revisited. *Euro. Phys. J. E*, 9:143–160, 2002.

[33] J. B. Fournier, A. Ajdari, and L. Peliti. *Phys. Rev. Lett.*, 86:4970, 2001.

[34] W. K. den Otter. Area compressibility and buckling of amphiphilic bilayers in molecular dynamics simulations. *J. Chem. Phys.*, 123:214906, 2005.

[35] W. Rawicz, K. C. Olbrich, T. McIntosh, D. Needham, and Evans E. *Biophys. J.*, 79:328, 2000.

[36] J. R. Henriksen and J. H. Ipsen. *Euro. Phys. J. E*, 14:149, 2004.

[37] R. Goetz, G. Gompper, and R. Lipowsky. Mobility and elasticity of self-assembled membranes. *Phys. Rev. Lett.*, 82:221, 1999.

[38] W. K. den Otter and W. J. Briels. The bending rigidity of an amphiphilic bilyer from equilibrium and nonequilibrium molecular dynamics. *J. Chem. Phys.*, 118:4712, 2003.

[39] S.J. Marrink and A. E. Mark. Effect of undulations on surface tension in simulated bilayers. *J. Phys. Chem. B*, 105:6122, 2001.

[40] G. Brannigan and F.L.H. Brown. A consistent model for thermal fluctuations and protein-induced deformations in lipid bilayers. *Biophys. J.*, 90:1501–1520, 2006.

[41] R. E. Waugh. Surface viscosity measurements from large bilayer vesicle tether formation. experiments. *Biophys. J.*, 38:29–37, 1982.

[42] M. P. Allen and D. J. Tildesley. *Computer Simulation of Liquids*. Oxford University Press, Oxford, U. K., 1987.

[43] D. Frenkel and B. Smit. *Understanding molecular simulations. From algorithms to applications*. Academic press, San Diego, CA, 2002.

[44] R. Goetz and R. Lipowsky. Computer simulations of bilayer membranes: Self-assembly and interfacial tension. *J. Chem. Phys.*, 108:7397–7409, 1998.

[45] W. Smith and T. R. Forester. Dlpoly2.0: A general-purpose parallel molecular dynamics simulation package. *J. Mol. Graphics*, 14:136–141, 1996.

[46] T. V. Tolpekina, W. K. den Otter, and W. J. Briels. Simulations of stable pores in membranes: System size dependence and line tension. *J. Chem. Phys.*, 121:8014–8020, 2004.

[47] T. V. Tolpekina, W. K. den Otter, and W. J. Briels. Nucleation free energy of pore formation in an amphiphilic bilayer studied by molecular dynamics simulations. *J. Chem. Phys.*, 121:12060–12066, 2004.

[48] W. L. C. Vaz, R. M. Clegg, and D. Hallmann. Translational diffusion of lipids in liquid crystalline phase phosphatidylcholine multibilayers. a comparison of experiment with theory. *Biochemistry*, 24:781–786, 1985.

[49] A. Filippov, G. Orädd, and G. Lindblom. The effect of cholesterol on the lateral diffusion of phospholipids in oriented bilayers. *Biophys. J.*, 84:3079–3086, 2003.

[50] R. Dimova, C. Dietrich, A. Hadjiisky, K. Danov, and B. Pouligny. Falling ball viscosimetry of giant vesicle membranes: finite-size effects. *Eur. Phys. J. B*, 12:589–598, 1999.

[51] M. Abramowitz and I. A. Stegun. *Handbook of mathematical functions*. Dover publications, New York, N. Y., 1979.

[52] R. Lipowsky and S. Grotehans. Renormalization of hydration forces by collective protrusion modes. *Biophys. Chem.*, 49:27–37, 1994.

[53] M. Kraus and U. Seifert. Relaxation modes of an adhering bilayer membrane. *J. Phys. II France*, 55:1117–1134, 1994.

[54] E. Evans, V. Heinrich, F. Ludwig, and W. Rawicz. Dynamic tension spectroscopy and strength of biomembranes. *Biophys. J.*, 85:2342–2350, 2003.

[55] W. Helfrich and R. M. Servuss. *Nuovo Cimento*, 3 D:137, 1984.

# 5 The influence of lipid architecture on the intermonolayer friction and shear viscosity of bilayer membranes

*The resistance of bilayer membranes against flow can be characterized by a surface viscosity for in-plane shear deformations, and an intermonolayer friction coefficient for slip between the two leaflets of the bilayer. We have used equilibrium and non-equilibrium molecular dynamics simulations to study both parameters for a variety of coarse-grained model lipids. The single-tail lipid model of the previous chapter is extended with pairwise friction and random forces to fine-tune its dynamical properties, but this modification proves only moderately successful. Double-tailed lipids are therefore simulated using another, recently introduced coarse-grained model. For lipids with two identical tails, the surface shear viscosity rises rapidly with tail length, while the intermonolayer friction coefficient is less sensitive to the tail length. Interdigitation of lipid tails across the bilayer midsurface, as observed for lipids with two distinct tails, strongly enhances the intermonolayer friction coefficient, but leaves the surface viscosity unaltered. The systematic underestimation of the experimental surface viscosity and intermonolayer friction, observed for all analysed lipid models, is attributed to the deficiency of coarse-grained models to accurately describe the interactions between close-packed alkanes.*

## 5.1 Introduction

Membranes play a vital role in living cells, where they act as semi-permeable barriers, host numerous proteins, and provide mechanical strength while retaining a high degree of flexibility. [1, 2, 3] Membranes consist of lipids, i.e., biological amphiphiles, which cluster into locally planar bilayered structures under a combination of hydrophobic and hydrophilic interactions. In the absence of covalent bonds between the lipids, a bilayer behaves as a two-dimensional liquid characterised by a surface shear viscosity $\eta_s$. Relative motion between the two leaflets of a bilayer is opposed by a friction force; the ratio between the force per unit area and the slip velocity is known as the intermonolayer friction coefficient $b$. Living cells actively control the flow characteristics of their membranes by changing the mixture of lipids and cholesterol present in the membrane. Here we are interested in how the flow properties of homogeneous bilayers are related to their constituent lipids.

Current experiments to measure surface shear viscosities of membranes are all based on the theoretical work of Saffman,[4] who derived an expression for the translational diffusion coefficient of a tracer particle confined to a membrane, i.e., a geometry-specific analogue of the familiar Stokes-Einstein relation. Most viscosity measurement employ membrane-bound proteins[5, 6] as the diffusing tracer particle, while recently latex spheres have been used.[7, 8] Typical surface shear viscosities reported in the literature lie in the range of $10^{-7}$ to $10^{-6}$ surface poise (where 1 SP = $10^{-3}$ Pa m s). The best-studied tracer particles, however, are the lipids constituting the bilayer, [5, 9, 10, 11, 12, 13] but their lateral diffusion coefficients $D$ are rarely converted into surface viscosities because these tracers are considered too small for Saffman's continuum hydrodynamics model to hold true, and because lipids are strongly affected by microdomain formation within the membrane. Fluorescence after photobleaching (FRAP) experiments[12] indicate that the saturated symmetric phosphatidylcholine (PC) lipids DLPC, [1] DMPC and DPPC have surprisingly similar diffusion coefficients at 50°C, despite varying in tail length from 12 to 16 carbon atoms, while the diffusion coefficient of the asymmetric POPC is lower by about one-third. In nuclear magnetic resonance (NMR)

1 *Abbreviations used*: DLPC = dilauroylphospatidylcholine (diC12:0), DMPC = dimyristoylphospatidylcholine (diC14:0), DPPC = dipalmitoylphospatidylcholine (diC16:0), DSPC = distearoylphospatidylcholine (diC18:0), POPC = 1-palmitoyl-2-oleoylphospatidylcholine (C16:0/C18:$1_{c9}$), DOPC = dioleoylphospatidylcholine (diC18:$1_{c9}$), SOPC = 1-stearoyl-2-oleoylphospatidylcholine (C18:0/$1_{c9}$) and CHOL = cholesterol.

measurements,[10] however, the lipids DMPC, POPC and DOPC were found to posses nearly identical diffusion coefficients, suggesting a remarkable insensitivity to both tail length and saturation. A recent NMR study[9] reports a decrease in the lateral diffusion with increasing tail length, for monounsaturated lipids with tails of up to 22 carbons. Addition of cholesterol, which is known to increase the ordering of the lipids and to induce domain formation, slows the lateral diffusion down, as does a reduction in the temperature. The surface viscosity, for which much fewer data are available, is expected to follow trends reverse to those of the diffusion coefficient, i.e., $\eta_s$ declines where $D$ rises and vice versa.

The intermonolayer friction coefficient, whose existence first came to prominence a decade ago, [14, 15, 16, 17, 18] has been measured by a number of techniques. In the experiments described by Evans and Yeung[14] and by Chizmadzhev *et al.*,[19] a mechanical force is used to pull the bilayer through a region of extremely high local curvature, causing the monolayers to slip past oneanother. Merkel *et al.*[20] fixed the bottom monolayer of a membrane to a glass substrate and deduced a friction coefficient from the diffusion of tracer lipids in the top monolayer. Pfeiffer *et al.*[21] and Pott and Méléard[22] derived friction coefficients from the decay rates of thermal undulations of bilayers and vesicles, respectively, but the interpretation of these experiments proved to be complicated. These experiments yield a typical range of $10^8$ to $10^9$ Pa m$^{-1}$ s for the intermonolayer friction coefficient. The relation between intermonolayer friction and lipid architecture has hardly been explored. Here again, cholesterol has been found to slow down the dynamics; the intermonolayer friction coefficient of SM/CHOL (in a 1:1 mixture) is nearly an order higher than those of SOPC/CHOL and MOPC/CHOL. [23] It is our expectation that $b$ is strongly affected by interdigitation, i.e., long lipid tails whose ends cross the bilayer midsurface and protrude among the tails of the opposing bilayer leaflet. [24, 25, 26]

Computer simulations have provided a wealth of detailed information on membranes,[27, 28] but there are few studies focusing on the flow properties of bilayers. A number of authors have reported lipid diffusion coefficients, [29, 30, 31, 32] also in relationship to tail length,[33, 34] but these have not been related to the surface shear viscosity. The exponential relaxation of thermal undulations[35] and the relative Brownian motion of monolayers[34] are, in principle, connected to the intermonolayer friction. The first direct calculations of $\eta_s$ and $b$ have been reported only recently, using bilayers under shear[36] and at equilibrium.[36,

37] Here we extend our previous studies by using a series of coarse-grained model lipids to explore the relationship between lipid architecture and bilayer flow behaviour.

The outline of this paper is as follows: The techniques used to calculate surface viscosities and intermonolayer frictions from both equilibrium and non-equilibrium molecular dynamics simulations are described in the next section. Simulations with the single-tail lipid model by Goetz and Lipowsky,[31] and an amended version thereof, are presented in Section 5.3. The dynamics obtained with the double-tail lipid model by Marrink *et al.*[32] is analysed in Section 5.4, with the tail lengths of the latter model being varied in Section 5.5. We end with a discussion and summary of the results in Section 5.6.

## 5.2 Theory

The aim of this section is to provide a brief introduction to the key parameters in the static and dynamic description of membranes, and to describe the simulation techniques that we have used to calculate these parameters.

### 5.2.1 Static properties

In the analytical continuum description of a membrane, the configuration of a near-planar bilayer is conveniently described, in the Monge representation, by the elevation $u(\mathbf{x})$ of the midsurface of the bilayer relative to a flat reference plane for any point $\mathbf{x}$ on this plane. The free energy of the bilayer is then given by the Helfrich theory,[2, 38, 39]

$$F[u] = 2\kappa \int H^2(\mathbf{x})\, d\mathbf{x} + \frac{K_A}{2} A_0 \left( \frac{A[u] - A_0}{A_0} \right)^2 . \tag{5.1}$$

The first term on the r.h.s. yields the bending free energy, with bending rigidity $\kappa$ and mean curvature $H = \frac{1}{2}\nabla^2 u$. An additional bending contribution from the Gaussian curvature has been ignored here, as this term is constant in the current set-up. The second term on the r.h.s. describes the global elastic energy, where $A$ is the area of the midsurface, $A_0$ the equilibrium area and $K_A$ the bilayer elastic modulus. Note that at this level of description, which is the starting point for experimental and simulation studies on the mechanical properties of membranes, the twinned nature of the bilayer is irrelevant.

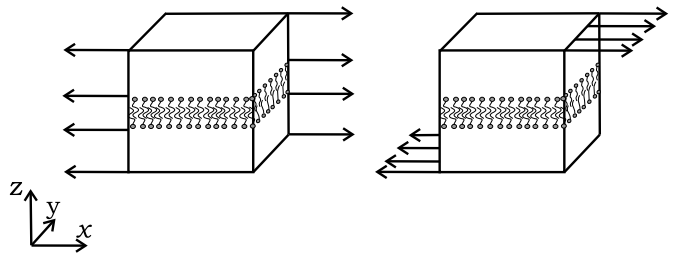


Figure 5.1: Cartoons of the simulation set-up of a bilayer under shear, with the arrows indicating the flow fields. A perpendicular shear flow (left) is used to determine the surface shear viscosity of the bilayer, a parallel shear flow (right) for the intermonolayer friction coefficient.

In our simulation set-up, see Fig. 5.1, the nearly flat bilayer is oriented parallel to the square $xy$ ground plane of a periodic simulation box with dimensions $L_\parallel \times L_\parallel \times L_\perp$. Differentiating the free energy with respect to the groundplane area $A_\parallel = L_\parallel^2$, at constant volume, one then arrives at

$$L_\perp \Delta p = \left(\frac{\partial F}{\partial A_\parallel}\right)_V \approx \frac{K_A}{A_0}(A_\parallel - A_0). \tag{5.2}$$

The l.h.s. is exact, with $\Delta p = p_{zz} - \frac{1}{2}(p_{xx} + p_{yy})$ and $\mathbf{p}$ the stress tensor. On the r.h.s. we have made the common assumptions that the area dependence of $F$ is dominated by the elastic term, and that $A[u] \approx A_\parallel$ for a nearly flat bilayer, although these approximations are to be regarded with care.[40] In the absence of externally imposed restraints, a freely floating bilayer of $N$ molecules will adapt a tensionless state where its average area equals the equilibrium area of $A_0 = Na_0/2$. We reproduce this state as closely as possible in our simulations, by varying the groundplane area of the box until $\Delta p = 0$.

Exploiting the periodicity of the simulation box, we next express the midsurface of the bilayer as a Fourier series,

$$u(\mathbf{x}) = \sum_{\mathbf{q}} h_q e^{i\mathbf{q}\cdot\mathbf{x}}, \tag{5.3}$$

where $\mathbf{q} = 2\pi\mathbf{n}/L_\parallel$ is a wave vector with integer vector $\mathbf{n} = (n_x, n_y)$. By noting that $h_q = u^*_{-\mathbf{q}}$ for a real function $u(\mathbf{x})$, with the asterisk denoting a complex conjugate, the summation can be reduced to two quadrants. Inserting this series into the Helfrich expression and using the

equipartition theorem, one readily recovers the structure factors[2]

$$S(\mathbf{q}) = \langle h_q h_q^* \rangle = \frac{k_B T}{\kappa A_\parallel} q^{-4} \tag{5.4}$$

for a bilayer in the tension-less state, with $T$ the temperature, $k_B$ Boltzmanns constant and the pointed brackets denoting a canonical average.

### 5.2.2 Surface viscosity

The surface shear viscosity of a bilayer is easiest established in molecular dynamics simulations by shearing the bilayer,[36] analogous to standard shear viscosity calculations for liquids.[41] A so-called perpendicular shear flow is imposed on the bilayer by applying Lees-Edwards sliding boundary conditions [41] along the $y$ direction, see Fig. 5.1, culminating in a linear flow field $\mathbf{v}(\mathbf{r}) = y\dot{\gamma}\hat{\mathbf{e}}_x$ in both the bilayer and the surrounding solvent. The surface viscosity is defined as the proportionality constant between the applied shear rate $\dot{\gamma}$ and the corresponding shear force acting per unit length of bilayer,

$$\eta_s \equiv \frac{F_{\text{shear}}^{\text{bilayer}}}{L_\parallel \dot{\gamma}} = \frac{\langle p_{xy} \rangle L_\perp L_\parallel - \eta_w \dot{\gamma}(L_\perp - h) L_\parallel}{L_\parallel \dot{\gamma}}. \tag{5.5}$$

The simulation algorithm readily provides the total force applied to shear the bilayer plus the solvent, by means of the off-diagonal stress tensor element $p_{xy}$ times the area $L_\parallel L_\perp$, but it does not yield the separate force contribution to shear the bilayer. In the last numerator of Eq. (5.5), therefore, we have explicitly calculated the shear force on the solvent, using the solvent viscosity $\eta_w$ and the bilayer thickness $h$, and subtracted this force from the total shear force to arrive at the desired bilayer force.

In simulations and experiments with quiescent membranes, the surface viscosity can also be deduced from the lateral diffusion coefficient of an embedded tracer particle, by means of the Saffman-Stokes-Einstein expression,[4]

$$D = \frac{k_B T}{4\pi\eta_s} \left[ \ln\left( \frac{\eta_s}{R\eta_w} \right) - 0.577\ldots \right]. \tag{5.6}$$

Here, the tracer particle is a mesoscopic cylinder of radius $R$, oriented parallel to the membrane normal, with a length exceeding the membrane thickness. The membrane is regarded as a single planar two-dimensional fluid, surrounded by solvent on either side.

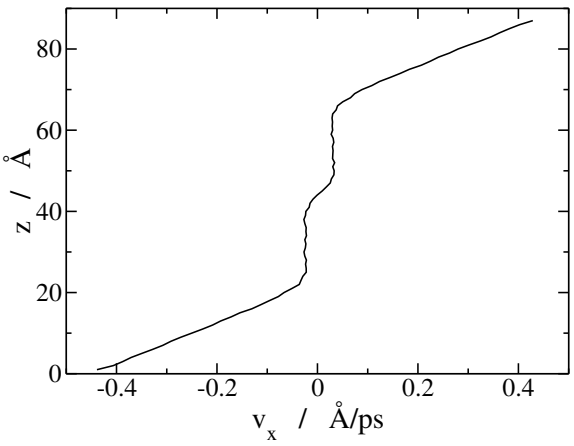


Figure 5.2: The velocity along the flow ($x$) direction, as a function of the height ($z$) in the simulation box, for a bilayer exposed to a parallel shear with an extremely high shear rate. The two monolayers, each about 20 Å thick, are seen to slide along one another with a velocity difference $2\Delta v$, while the solvent shows a linear flow field with shear rate $\dot{\gamma}_w$.

### 5.2.3 Intermonolayer friction

Shear simulations are also an attractive tool for inducing slip between the two leaflets of a bilayer, by using Lees-Ewards sliding boundary conditions along the $z$ direction to create a so-called parallel shear flow, see Fig. 5.1. The imposed periodic flow field, $\mathbf{v}(\mathbf{r}+L_\perp\hat{\mathbf{e}}_z) = \mathbf{v}(\mathbf{r})+L_\perp\dot{\gamma}\hat{\mathbf{e}}_x$, results in a non-linear velocity profile, depicted in Fig. 5.2, because the sheared system is non-homogeneous along the bilayer normal. In this graph, one readily recognizes the monolayers as two slabs of thickness $h/2$ moving with equal but opposing velocities $\pm\Delta v\hat{\mathbf{e}}_x$, resulting in friction forces $\mp F_{\text{friction}}\hat{\mathbf{e}}_x$ working at the midsurface of the bilayer. The solvent on either side of the membrane displays a linear profile with a shear rate $\dot{\gamma}_w$, which clearly is larger than the imposed rate $\dot{\gamma}$, from which the tangential solvent forces acting on the top and bottom monolayers are readily deduced by assuming stick boundaries at the interfaces. The intermonolayer friction coefficient is then calculated from

$$b \equiv \frac{2F_{\text{friction}}}{2A_{\|}\Delta v} = \frac{\eta_w\dot{\gamma}_w}{\Delta v}. \tag{5.7}$$

where the force balance on the bilayer has been used in the last step to equate the intermonolayer friction force to the solvent shear forces.

The velocity profile of Fig. 5.2 was obtained at a high shear rate of $\dot{\gamma} = 0.01\,\mathrm{ps}^{-1}$, to emphasize the slip velocity $\Delta v$ against a background of thermal noise. At the lower shear rates employed in most simulations it is nearly impossible to extract $\Delta v$ from the velocity profile. In those cases the slip velocity can be calculated from either the average distance travelled by an amphiphile $i$ along the flow direction over a time interval $t$, $\Delta v = \pm\langle x_i(t) - x_i(0)\rangle/t$, or from the shear rate in the solvent, $2\Delta v = \dot{\gamma} L_\perp - \dot{\gamma}_w(L_\perp - h)$. Note that the last expression assumes stick boundary conditions at the bilayer-solvent interfaces, hence the observed agreement between these two approaches justifies this assumption and thereby the last step in Eq. (5.7).

Intermonolayer friction not only rises to prominence in an external flow field, but in any deformation of the bilayer which causes the two monolayers to move relatively to one-another. Seifert and Langer[16, 17] and Evans and Yeung[14, 18] independently derived the coupled equations of motion for the undulations and the monolayer densities of bilayers in near-planar and axial-symmetric configurations, respectively. In these equations, which are valid in the creeping-flow limit, the driving forces derived from the bending and elastic free energies in a generalised Helfrich equation are opposed by dissipative forces due to surface viscosity, intermonolayer friction and solvent viscosity. The latter requires solving the velocity and pressure fields in the solvents above and below the membrane, subject to the boundary conditions set by the normal and lateral velocities of the bilayer (where, again, stick boundary conditions are assumed). We refer the interested reader to previous work [16, 17, 42] for the detailed analytical solution of this model, and directly proceed to the final result: the Fourier coefficients $h_q$ of the undulations relax independently to equilibrium by a double exponential decay. In combination with the Onsager regression hypothesis, the time correlation of a thermal undulation then reads

$$\langle h_q(t) h_q^*(0)\rangle = A_1 e^{-\gamma_1 t} + A_2 e^{-\gamma_2 t}. \tag{5.8}$$

The positive amplitudes $A_i$ are functions of the wave number, and obviously obey $A_1 + A_2 = S(q)$. The relaxation rates $\gamma_i$ converge to power-law behaviour on either side of a cross-over wavenumber $q_c = \eta K_A / b\tilde{\kappa}$, with $\tilde{\kappa} = \kappa + K_A d^2$ the effective bending rigidity and $d$, the distance between the bilayer midsurface and the monolayer neutral surfaces,[16, 42] approximately equal to half the monolayer thickness (hence, $d = h/4$). By inserting typical experi-

mental values one finds that $q_c \approx (0.5 - 5.0)\,\mu\mathrm{m}^{-1}$ lies well below the smallest wavenumbers encountered in membrane simulations with molecular detail, $q_{\min} = 2\pi/L_{\|} \approx 0.5\,\mathrm{nm}^{-1}$. We therefore expect in these simulations a slow relaxation process dominated by intermonolayer friction, $\gamma_1 = (K_A\kappa/4b\tilde{\kappa})q^2$, and a fast relaxation process through viscous dissipation in the solvent, $\gamma_2 = (\tilde{\kappa}/4\eta)q^3$. The double exponential decay has been observed in experiments on vesicles[22] and in simulations of planar membranes,[37, 42] where it proved sensitive to the surface tension. Note that for low wavenumbers, $q \ll q_c$, the scaling laws for the relaxation rates are exchanged, with $\tilde{\kappa}$ replaced by $\kappa$. The fast relaxation is now dominated by intermonolayer friction and the slow relaxation by solvent viscosity; the rate of the latter process has previously been derived for membranes without internal friction.[43, 44]

### 5.2.4 Coarse graining

Fully atomistic simulation models of membranes place a heavy burden on available computer resources and are therefore limited to small time and length scales. These drawbacks can be overcome by using a coarse grained (CG) simulation model, in which a number of atoms are grouped together into one interaction site, known as a CG particle. In the simplest and most-widespread implementations, the CG particles interact with their neighbours through pairwise-additive conservative forces, describing an effective average of the conservative forces acting between the atoms usurped in the particles. These smoothed potential forces are often the only forces included in a CG simulation, as is the case for the two CG lipid force fields applied here,[31, 32] because the conservative forces fully determine the thermodynamic properties of the system.

The eliminated fast motions of the atoms also give rise to friction and random forces at the level of the CG particles, turning the equation of motion of the CG particles into a non-deterministic Langevin-type equation.[45] In Brownian dynamics simulations these two additional forces are implemented as external forces, acting relative to a fixed background,[41] while in dissipative particle dynamics (DPD) they are specifically designed as pairwise-additive forces between the particles. [46, 47] The latter approach conserves local momentum, and hence hydrodynamic interactions appear naturally, which makes it our method of choice for the current shear simulations. In DPD, the force on particle $i$ is expressed as a sum

over neighbours $j$, each contributing

$$\mathbf{F}_{ij} = F_c(r_{ij})\hat{\mathbf{r}}_{ij} - \gamma_d\omega_d(r_{ij})(\mathbf{v}_{ij}\cdot\hat{\mathbf{r}}_{ij})\hat{\mathbf{r}}_{ij} + \sigma_r\omega_r(r_{ij})\theta_{ij}\hat{\mathbf{r}}_{ij}. \tag{5.9}$$

Here $\hat{\mathbf{r}}_{ij}$ is the unit vector pointing from $j$ to $i$, $r_{ij}$ the distance between the particles, and $\mathbf{v}_{ij}$ their velocity difference. The details of the conservative force $F_c$ will be specified below; although we follow the main structure of the DPD equations of motion, we do not copy the extremely soft pair potentials usually associated with DPD. We follow the conventional choice of a linearly declining random force, $\omega_r(r) = 1 - r/r_c$ upto the cutoff distance $r_c$, with strength $\sigma_r$. The parameters of the friction force then follow from the fluctuation-dissipation theorem,[46] $2k_BT\gamma_d\omega_d(r) = \sigma_r^2\omega_r^2(r)$, which clearly illustrates the combined operation of friction and random forces as a thermostat maintaining a temperature $T$ in the simulated system. In the last term of Eq. (5.9), the Markovian random numbers $\theta_{ij}(t)$ have zero average, unit standard deviation, are uncorrelated across particle pairs and are delta-correlated in time.

## 5.3 Single-tail lipid model

Goetz and Lipowsky[31] introduced a coarse-grained model in which an amphiphile is represented by a single head bead ($h$) attached to a string of four tail beads ($t$), immersed in a liquid of loose water beads ($w$). Interactions between like particles and the hydrophilic head-water interactions are modelled by a Lennard-Jones potential, $\Phi_{\mathrm{LJ}}(r) = 4\varepsilon[(\sigma/r)^{12} - (\sigma/r)^6]$, where the parameters $\varepsilon = 2\,\mathrm{kJ/mol}$ and $\sigma = 1/3\,\mathrm{nm}$ are tuned to roughly match a CG particle to two water molecules or three $CH_2$ units. The hydrophobic tail-water and tail-head interactions are modelled by a purely repulsive potential, $\Phi_{\mathrm{rep}}(r) = \varepsilon(1.05\sigma/r)^9$. The non-bonded forces are implemented in a shifted force fashion, ensuring a smooth truncation of both energy and force at a cut-off distance of $2.5\,\sigma$. Harmonic bond potentials, $\Phi_{\mathrm{bond}}(l) = 5000\varepsilon\sigma^{-2}(l-\sigma)^2$, are used to connect the particles within a molecule. Bending stiffness is introduced by an angle potential, $\Phi_{\mathrm{angle}}(\phi) = 2\varepsilon[1-\cos(\phi)]$; there are no dihedral potentials. All particles have the same mass $m$ of 36 a.u., at a fixed number density of 2 particles per $3\,\sigma^3$. In all simulations the temperature is maintained at $1.35\,\varepsilon/k_B = 325\,\mathrm{K}$, using either a Nosé-Hoover thermostat[41] or by the DPD thermostat of Section 5.2.4. All simulations were run with the DL_POLY_2.0 package,[48] tailored to our specifications, using the Verlet

leapfrog scheme with a time step of $\tau/500$, where $\tau = \sqrt{m\sigma^2/\varepsilon}$ is the implicitly defined unit of time. The thermodynamic properties previously obtained with this model, like the elastic modulus,[31, 40] bending rigidity[49, 50] and line tension coefficient,[51, 52] compare favourably with experimental data. Here we focus on the dynamical properties of the model, which were not taken into consideration by Goetz and Lipowsky[31] when they developed the model. It is therefore to be expected that the dynamics of this model, like that of many other CG models,[32] evolves quicker than that of experimental systems.

To ascertain the speed-up, we first performed simulations of the separate components of the model. Solvent exposed to shear rates ranging from 0.001 to $0.2\,\tau^{-1}$ behaved like a Newtonian liquid with a viscosity $\eta_w = 1.0\varepsilon^{1/2}m^{1/2}\sigma^{-2}$ or $1.3 \cdot 10^{-4}$ Pa s, which amounts to about one quarter of the experimental viscosity of water at this temperature.[53] The viscosity of a homogeneous liquid of chains of five tail particles, $t_5$, was found to be $\eta_{\text{tail}} \approx 2.1\varepsilon^{1/2}m^{1/2}\sigma^{-2}$, or about $1/8^{\text{th}}$ of the experimental viscosity of the corresponding *n*-pentadecane liquid.

The dynamical properties of bilayers constructed with this lipid model have previously been reported elsewhere;[36] here we briefly summarise the results to motivate the need for an amended model. A bilayer system was created by placing 1152 lipids on lattice positions and surrounding them by 10,800 randomly placed solvent particles. The box was equilibrated and rescaled to minimize the surface tension, until the tension-less state was reached, $\Delta p = 0$. Additional confirmation hereof was provided by the scaling exponent of almost -4 observed in a structure factor calculation, see Eq. (5.4). By applying perpendicular shear flows to this system, the surface shear viscosity of the bilayer was found to be about $20\,\varepsilon^{1/2}m^{1/2}\sigma^{-1}$, or $8.5 \cdot 10^{-13}$ Pa m s, for shear rates ranging from 0.01 to $0.1\,\tau^{-1}$. Simulations under parallel shear flow yielded an intermonolayer friction coefficient $b = 3.7\varepsilon^{1/2}m^{1/2}\sigma^{-3}$, or $1.4 \cdot 10^6$ Pa m$^{-1}$ s, for slip velocities upto $0.014\sigma/\tau$, while the bilayer became unstable at higher slip velocities. Note that both $\eta_s$ and $b$ underestimate experimental findings by some two to three orders of magnitude. Although this speed-up by coarse-grained models is convenient when developing and testing new simulation techniques, it is rather inconvenient if one aims at reproducing or even predicting experimental results. Hence, we want to remedy this situation by improving the employed simulation model.

In the Goetz-Lipowsky model only potential forces are used, while friction and random

forces, which naturally arise in a coarse-graining procedure, are ignored altogether. Here we are going to reinstate these forces, in order to improve the dynamical properties of the model – this addition leaves the thermodynamical properties of the system unaltered. By increasing the viscosities of the solvent and of the $t_5$ liquid to realistic values, we aspire to obtain improved values for the surface viscosity and intermonolayer friction of the bilayer. To this effect, we simulated the above described homogeneous systems again, using friction and random forces implemented in the pairwise fashion detailed in Section 5.2.4. The cut-off distance of the DPD forces was set equal to that of the conservative forces. Upon varying the DPD parameter $\sigma_r$, which implies changing $\gamma_d$ to maintain a constant temperature, the viscosity of the solvent showed a nearly quadratic dependence on $\sigma_r$, reaching the experimental viscosity of water for $\sigma_r = 210\,\varepsilon\tau^{1/2}/\sigma$. The $t_5$ viscosity revealed shear thinning, with a reduction of the viscosity by about 30% over the range $\dot{\gamma} \in (0.01 - 0.06)\,\tau^{-1}$. A friction parameter $\sigma_r = 350\,\varepsilon\tau^{1/2}/\sigma$ was needed to match the extrapolated viscosity at zero shear rate with the experimental viscosity. The friction and random forces are thus capable of raising the solvent and $t_5$ viscosities to the desired levels, albeit at the expense of a 30% increase in the computational effort per simulation step.

The two established values for $\sigma_r$ were carried over to the bilayer system – all lipid-lipid interactions were treated similarly to a $t-t$ interaction, while for solvent-lipid interactions the $\sigma_r$ of the more nimble solvent particles was used. In subsequent simulations under parallel and perpendicular shear, we found that the addition of friction and random forces did not quite have the impact we had hoped for. Despite the near ten-fold increase of the $t_5$ viscosity, the intermonolayer friction has merely quadrupled to $b = 14\varepsilon^{1/2}m^{1/2}\sigma^{-3}$, or $5.4 \cdot 10^6\,\mathrm{Pa\,m^{-1}\,s}$, and thus remains well below typical experimental values. The surface viscosity follows the $t_5$ viscosity more closely, rising by an order of magnitude to $\eta_s \approx 200\varepsilon^{1/2}m^{1/2}\sigma^{-1}$ or about $8.5 \cdot 10^{-12}\,\mathrm{Pa\,m\,s}$, which however still underestimates experimental values. Interestingly, the surface viscosity also inherited the shear thinning behaviour of the $t_5$ liquid, see Fig. 5.3. In the simulations under parallel shear, the maximum survivable slip velocity has diminished from $0.014\,\sigma/\tau$ under regular MD to $0.004\,\sigma/\tau$ with the DPD thermostat; beyond these rates the bilayer is torn apart and either disintegrates into small bilayer patches or recombines into a configuration perpendicular to the shear flow.

As we have seen, introducing friction and random forces does not suffice to recover the

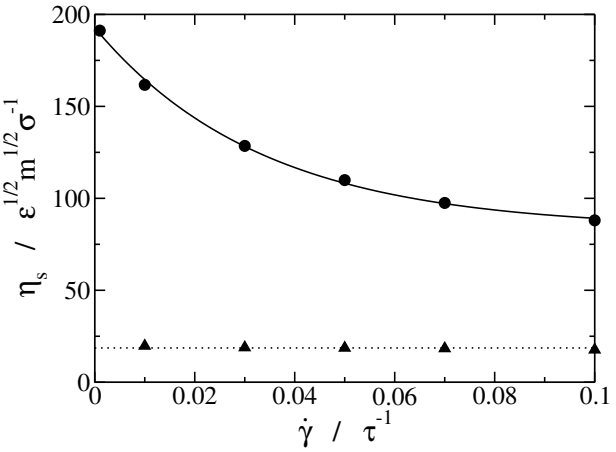


Figure 5.3: Surface shear viscosities obtained with the single-tail Goetz-Lipowsky model, before (triangles, dotted line) and after (circles, solid line) the introduction of pairwise-additive friction forces, as a function of the imposed perpendicular shear rate.

experimental values for the dynamical properties of the bilayer. We are therefore led to conclude that this single-tail CG representation is too simple to describe the dynamics of the double-tail lipids employed in the experiments. Hence, the next stage in our work is to change the architecture of the CG lipid to explicitly model two tails.

## 5.4 Double-tail lipid model

In this section on double-tailed lipids, we employ a CG model that was recently developed by Marrink *et al.*[32] to simulate DPPC and related amphiphiles. These authors chose a parameterisation in which groups of about four heavy atoms, and their attached hydrogens, are reduced to a single CG particle. Here we present a brief overview of the essentials of the model, referring the reader to the original work[32] for an extensive motivation of the parameters. The model discerns four major types of particles, representing groups of atoms with different properties: charged groups (*Q*), polar hydrophilic groups (*P*), weakly polar groups (*N*) and apolar hydrophobic groups (*C*). The latter two types are subdivided according to

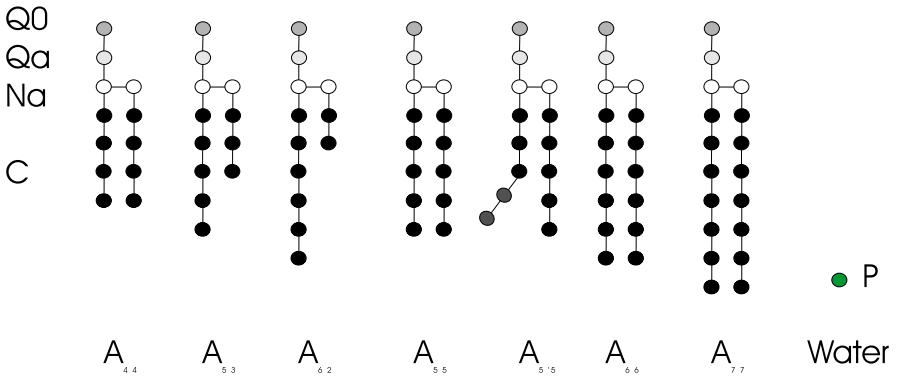


Figure 5.4: Cartoons of the double-tailed lipids simulated with the coarse-grained model by Marrink *et al.* Our short-hand notation is included below the lipids, the particle-type identification on the left and on the right.

their ability to act as a hydrogen bond acceptor (labeled $a$) or their inability to form hydrogen bonds (labeled 0). The head of a DPPC lipid (molecule $A_{44}$ in Fig. 5.4) is then represented by one $Q_0$ particle with charge $q = e$ for the choline group and one $Q_a$ particle with charge $q = -e$ for the phosphate group. The glycerol ester linkage is modelled by two particles of type $N_a$, while each $C_{16}H_{33}$ tail is reduced to a chain of four $C$ particles. Four water molecules are lumped into one bead of type $P$.

The non-bonded interactions between all particles, except bonded nearest neighbours, are described by a Lennard-Jones potential. The strength $\varepsilon_{ij}$ of the interaction can be read from Table 5.1; an effective radius $\sigma = 0.47\,\mathrm{nm}$ applies to all interactions. The LJ interactions are cut-off at a distance $r_c = 1.2\,\mathrm{nm}$, using a switch function to create a smooth shift to zero beyond 0.9 nm. Charged particles $i$ and $j$ also interact by a Coulombic potential, $\Phi_{\mathrm{el}}(r_{ij}) = q_i q_j/(4\pi\varepsilon_0\varepsilon_r r_{ij})$, which is screened by both a relative dielectric constant $\varepsilon_r = 20$ and a switch function running from $r = 0$ to $r_c$; here $\varepsilon_0$ denotes the dielectric constant of vacuum. Bonded interactions between covalently connected particles are discribed by a harmonic potential, $\Phi_{\mathrm{bond}}(l) = \frac{1}{2}K_{\mathrm{bond}}(l-\sigma)^2$, with $K_{\mathrm{bond}} = 1250\,\mathrm{kJ/mol\,nm^2}$. The bending stiffness of the tails is introduced by an angle potential, $\Phi_{\mathrm{angle}}(\theta) = \frac{1}{2}K_{\mathrm{angle}}[\cos(\theta) - \cos(\theta_0)]^2$, with $K_{\mathrm{angle}} = 25\,\mathrm{kJ/mol}$ and $\theta_0 = 180°$, while there is no dihedral potential. All particles have the same mass of $m = 72\,\mathrm{a.u.}$. The temperature was maintained at 323 K using a Nosé-Hoover

| | $P$ | $N_a$ | $C$ | $Q_0$ | $Q_a$ |
|---|---|---|---|---|---|
| $P$ | 5.0 | 3.4 | 1.8 | 5.0 | 5.0 |
| $N_a$ | 3.4 | 4.2 | 2.6 | 3.4 | 3.4 |
| $C$ | 1.8 | 2.6 | 3.4 | 1.8 | 1.8 |
| $Q_0$ | 5.0 | 3.4 | 1.8 | 3.4 | 3.4 |
| $Q_a$ | 5.0 | 3.4 | 1.8 | 3.4 | 3.4 |

Table 5.1: Lennard-Jones interaction parameters $\varepsilon_{ij}$ between the five particle types of the coarse-grained lipid model by Marrink *et al.[32]*

thermostat, and in some runs a Hoover barostat was invoked to establish a pressure of 1 bar. The Verlet leap-frog algorithm allows a maximum time step of 20 fs.

To determine the dynamical properties of the aqueous solvent, we prepared a cubic box containing 6072 $P$-type particles. By using a Hoover barostat and thermostat, at 1 bar and 323 K respectively, the specific weight of the solvent was found to converge to nearly 1 g/cm$^3$. The diffusion coefficient of the CG particles was established at $D^{\mathrm{CG}}_{\mathrm{water}} = 2. \cdot 10^{-5}$ cm$^2$/s, which lies very close to the experimentally measured value for a water molecule at these conditions, $D^{\mathrm{exp}}_{\mathrm{water}} = 2.3 \cdot 10^{-5}$ cm$^2$/s. Groot and Rabone[54] suggested that these diffusion coefficients are related by $D^{\mathrm{CG}}_{\mathrm{water}} = D^{\mathrm{exp}}_{\mathrm{water}}/k$, for a compound CG particle representing $k$ water molecules. By inserting the above numbers in this expression, with $k = 4$, Marrink *et al.*[32] concluded that the dynamics of the simulation is too fast by a factor of four. Similar speed-up factors were obtained by comparing the simulated molecular diffusion coefficients for liquids of tails ($C_n$ with $n \leq 5$) with the measured coefficients for the corresponding linear alkanes ($\mathrm{C}_{4n}\mathrm{H}_{8n+2}$), where $k = 1$. These authors subsequently accounted for this speed-up by simply scaling every nanosecond of simulation time into 4 ns of real time. Although the relation $D^{\mathrm{CG}}_{\mathrm{tail}} = D^{\mathrm{exp}}_{\mathrm{alkane}}$ should hold true for a coarse-grained molecule representing one real molecule ($k = 1$), the expression for the diffusion coefficient of a compound ($k > 1$) particle is less evident: correlations between the molecules constituting the CG particle seriously complicate the picture. Since the major purpose of the solvent particles is to provide a hydrophilic, compressible and viscous environment to the bilayer, it is more natural to match the viscosity rather than the diffusion coefficient of the solvent. Simulations under shear yield $\eta^{\mathrm{CG}}_{\mathrm{water}} \approx 7 \cdot 10^{-4}$ Pa s, independent of the applied shear rate. The close proximity to the experimental

value under the prevailing conditions,[53] $\eta^{\mathrm{exp}}_{\mathrm{water}} = 5.5 \cdot 10^{-4}\,\mathrm{Pa\,s}$, suggests that there is no need to introduce friction and random forces in the equations of motion of the CG solvent particles.

The dynamics of a box of $C_4$ tails, i.e. the CG equivalent of liquid *n*-hexadecane, was analysed using a cubic box of 1518 molecules, again at 1 bar and 323 K. The simulations yield a diffusion coefficient $D^{\mathrm{CG}}_{\mathrm{tail}} = 1.2 \cdot 10^{-5}\,\mathrm{cm^2/s}$ which is nearly twice as high as the $D^{\mathrm{exp}}_{\mathrm{alkane}} = 0.7 \cdot 10^{-5}\,\mathrm{cm^2/s}$ obtained by extrapolating[55] the available experimental data[55] to the current temperature. The simulated viscosity of $\eta^{\mathrm{CG}}_{\mathrm{tail}} = 8 \cdot 10^{-4}\,\mathrm{Pa\,s}$ is about half the experimental value,[56] $\eta^{\mathrm{exp}}_{\mathrm{alkane}} = 1.9 \cdot 10^{-3}\,\mathrm{Pa\,s}$. This inverse proportionality between $D$ and $\eta$ agrees with the Stokes-Einstein expression. Guided by these numbers, one would introduce friction and random forces between the lipid particles to scale their dynamics down by a factor of two. Since our expectations are that the double-tailed architecture will affect the flow properties by more than the factor of two that can be gained from the friction and random forces, we have abstained here from these additional forces. Our bilayer-solvent model is therefore identical to the model proposed by Marrink *et al.*,[32] except for the omission of the four-fold multiplication of the simulation time scale.

The starting configuration of the bilayer-solvent system was prepared by expanding a sample box, made available by Marrink,[57] to 256 $A_{44}$ amphiphiles and 3000 solvent particles. The system was equilibrated by a 100 ns simulation at constant temperature, $T = 323\,\mathrm{K}$, followed by a 100 ns simulation at constant temperature and pressure, $p = 1$ bar. As a final step in locating the equilibrium tensionless state, the tension-strain curve of the bilayer was calculated by varying the ground-plane area around the final area of the *NPT* simulation. The zero tension intercept of this curve, see Eq. (5.2), is reached at an area per amphiphile of $a_0 = 0.66\,\mathrm{nm^2}$, which is slightly higher than the $0.64\,\mathrm{nm^2}$ reported by Marrink *et al.*[32]. This difference, as well as other small differences, are attributed to slight deviations in the simulation setup, including a smaller time step, the rescaling of the ground plane area at constant volume rather than at constant normal pressure $p_{zz}$, and the use of distinct simulation packages.

The equilibration simulations yield two additional mechanical properties of the membrane, which will be needed lateron to analyse the autocorrelation of the thermal undulations. From the slope of the tension-strain curve follows an area compressibility $K_A = 370\,\mathrm{mN/m}$,

as compared to the 400 mN/m obtained by Marrink *et al.* from area fluctuations in a barostatted simulation. The structure factors of the undulations of the bilayer at $A = A_0$ closely adhere to the predicted scaling law, see Eq. (5.4), confirming that we have indeed reached a state with vanishing tension, but the bending modulus of $\kappa = 8 \cdot 10^{-20}$ J or $18 k_B T$ is twice the value reported by Marrink *et al.*. Since the current small bilayer patch allows only a few undulatory modes, the above steps were repeated with a bilayer of 6400 lipids to confirm our original value for $\kappa$. Another independent estimate of $\kappa$ is obtained by exploiting that the compressibility defined by Eq. (5.2) is an effective area compressibility which, due to the approximate area calculation, decreases with system size according to[40] $K_A^{\text{eff}} = \left[K_A^{-1} + (k_B T / 32\pi^3 \kappa^2) A_0(N)\right]^{-1}$, with $K_A$ the intrinsic compressibility defined by Eq. (6.1); this effect explains the lower compressibility, $K_A^{\text{eff}} = 220$ mN/m, observed for the 6400 lipid bilayer. By combining the effective compressibilities of our small and large systems, or the corresponding values reported by Marrink *et al.*, we arrive at a bending rigidity of about $12 \cdot 10^{-20}$ J, suggesting that our original value for $\kappa$ is plausible. Note that the $K_A$ obtained by this system-size correction differs by a mere 2% from the $K_A^{\text{eff}}$ of the smaller bilayer, but by some 40% from the $K_A^{\text{eff}}$ of the larger bilayer.

The dynamical properties of the bilayer were again calculated using the procedures outlined in Section 6.2. By applying perpendicular shear flows with shear rates $\dot{\gamma}$ ranging from 0.1 to 1 $\text{ns}^{-1}$, we obtained a fairly constant surface viscosity $\eta_s = 1.2 \cdot 10^{-11}$ Pa m s. This value compares well with that of the single-tail model after the addition of inter-particle frictions, but both are one to two orders below typical experimental values. Under parallel shear deformations, using the aforementioned range of shear rates to induce slip velocities between 0.01 and 0.25 nm/ns, we obtained an intermonolayer friction coefficient $b = 2.6 \cdot 10^6$ Pa $\text{m}^{-1}$ s. Again, this value is in close proximity to that of the single-tail model with inter-particle frictions, but both lie some two to three orders below experimental values. It therefore appears that coarse grained bilayer models are not capable of quantitatively reproducing the experimental dynamical properties of membranes, although they do an excellent job on many thermodynamic properties.

In the remainder of this section two equilibrium approaches for determining $\eta_s$ and $b$ will be applied, to validate the numerical results from the non-equilibrium simulations and to ascertain the possible impact of shear on these parameters. A discussion on the possible

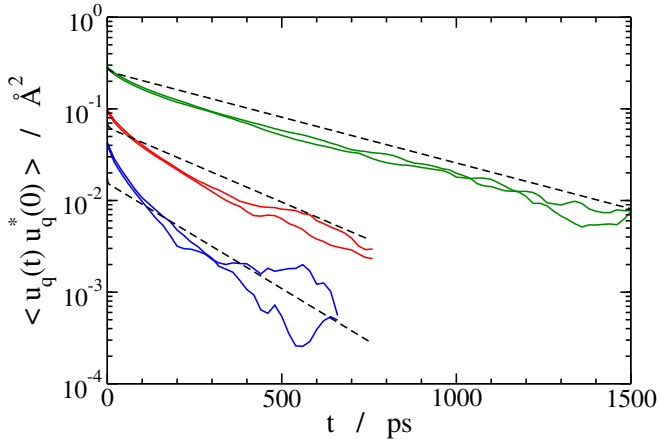


Figure 5.5: The autocorrelations (solid lines) of the thermal undulations of a bilayer of $A_{44}$ lipids, for the six smallest wave vectors commensurate with the box dimension, i.e., $q = 0.069\,\text{Å}^{-1}$ (top), $q = 0.097\,\text{Å}^{-1}$ (middle) and $q = 0.137\,\text{Å}^{-1}$ (bottom). Dashed lines indicate theoretical predictions by Eq. (5.8), where the amplitudes $A_i$ and relaxation rates $\gamma_i$ have been calculated using the intermonolayer friction coefficient determined in the parallel shear simulations.

sources of the discrepency between the experimental and simulated values of $\eta_s$ and $b$ will be postponed till Section 5.6.

An independent conformation of the aforementioned surface viscosity is provided by the satisfactory agreement between the lateral diffusion coefficient $D_{\text{msd}} = 1.5 \cdot 10^{-6}\,\text{cm}^2/\text{s}$ of a lipid in a quiescent bilayer, as determined from the mean square displacement, and the $D_{\text{Saffman}} = 1.4 \cdot 10^{-6}\,\text{cm}^2/\text{s}$ predicted by Saffman's theory. The latter number should be regarded with some care, however, as the simulation conditions do not adequately match the assumptions underlying the Saffman theory. In applying Eq. (5.6), we have approximated the floppy lipid by a rigid cylinder of radius $R = \sqrt{a_0/\pi}$, and regarded the bilayer as a continuum fluid on this length scale. Since the lipids span only one monolayer, rather than the entire bilayer, we followed previous experiments[6] and simulations[36] in substituting the membrane surface viscosity in Eq. (5.6) by the monolayer surface viscosity, $\eta_m = \eta_s/2$. Con-

sidering the assumptions made, the agreement between the two diffusion coefficients is very satisfactory indeed.

As described in Section 5.2.3, intermonolayer friction does not only manifest itself when the monolayers are forceably slided along oneanother, but also during the Brownian thermal undulations of a membrane. Figure 5.5 shows the time correlation functions of the three undulation modes $h_q$ with the smallest wavenumbers commensurate with the box dimensions, i.e. $q_1 = 2\pi/L_{\|} = 0.069\,\text{Å}^{-1}$, $q_2 = \sqrt{2}q_1$ and $q_3 = 2q_1$. We observe a clear exponential decay setting in after some 250 ps, especially for the smallest wavenumber. The slope of this decay agrees well with the slow relaxation rate $\gamma_1$ calculated from the theory of Seifert and Langer, plotted here as dashed lines, thus confirming the value of the intermonolayer friction coefficient. Only one parameter in this theory could not be determined a priori from an independent simulation, to wit the distance $d$ between the midsurface of the bilayer and the neutral surfaces of the monolayers.[39] We judiciously chose this distance to be equal to half the monolayer thickness, i.e., a quarter of the bilayer thickness, $d = h/4 \approx 1.1\,\text{nm}$, a choice which has worked out well in the past.[37, 42] In summary, we have seen that the dynamical properties calculated from non-equilibrium simulations are confirmed by the equilibrium simulations. The latter are more time consuming and less straightforward in their interpretation, hence we recommend the non-equilibrium simulations as the more practical methods.

## 5.5 Lipid architecture

In this section, the lengths of the hydrophobic tails in the Marrink model will be varied to investigate their influence on the dynamical properties of the bilayer. First to be discussed are asymmetric amphiphiles, whose distinct tails contain a combined total of 8 particles. Next are symmetric amphiphiles with elongated tails, and finally we briefly mention a lipid with one straight and one bend tail. Each simulated tension-less bilayer contains 256 identical lipids, and is surrounded by 3000 solvent particles. All tail particles are, as before, of the $A$ type.

The effect of asymmetric tail lengths was studied by comparing the reference $A_{44}$ lipid to its cousins $A_{53}$ and $A_{62}$, see Fig. 5.4. After equilibrating the membranes and exposing them to shear, we found that the three lipids yield nearly identical surface viscosities, which

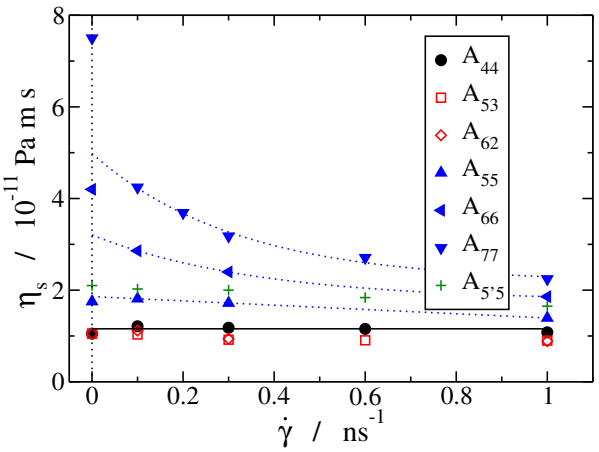


Figure 5.6: The surface shear viscosity as a function of the shear rate for the $A_{44}$ lipid (circles and solid line), two lipids with asymmetric tails (quadrangles), three lipids with extended tails (triangles and dotted lines), and the $A_{5'5}$ lipid (pluses). Viscosities obtained from the lipid lateral diffusion coefficients, by means of the Saffman theory, are plotted at $\dot{\gamma} = 0$.

in Fig. 5.6 are seen to be independent of the shear rate. The viscosities derived by means of the Saffman expression from the lateral diffusion coefficients of lipids in non-sheared bilayers, which are represented in the plot by the markers at $\dot{\gamma} = 0$, confirm this result. The intermonolayer friction, however, rises with increasing tail length difference, see Fig. 5.7. Because the equilibrium area $a_0$ and membrane thickness $h$ are only slightly different for the three lipids, we attribute this rise to the packing of the tails inside the hydrophobic core of the bilayer. The probability distributions of the amphiphilic particles along the normal to the membrane, as presented in Fig. 5.8 for the three lipids, indicate that the tails of the opposing leaflets are not interdigitated for the $A_{44}$ lipid. The long tails of the $A_{53}$ lipids interdigitate by about 1 particle with their counterparts from the opposing leaflet, and those of $A_{62}$ by about 3 particles. Note that the peaks of the particle distributions have shifted with increasing asymmetry, thereby reducing the actual number of interdigitating particles to less than the values of 2 and 4 which one would have expected for $A_{53}$ and $A_{62}$, respectively, on simple geometric grounds. Obviously, the enhanced number of inter-leaflet contacts created

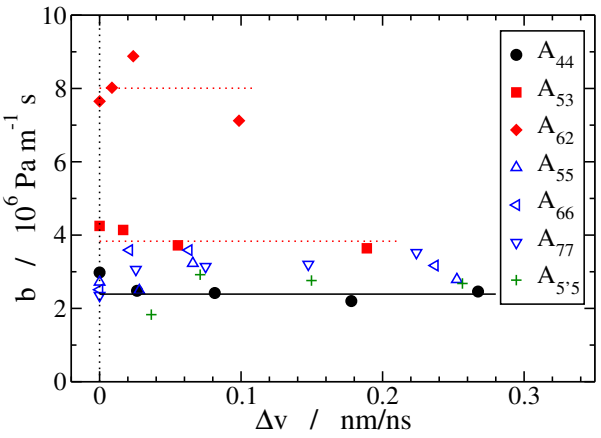


Figure 5.7: The intermonolayer friction coefficient as a function of the slip velocity for the $A_{44}$ lipid (circles and solid line), two lipids with asymmetric tails (quadrangles and dotted lines), three lipids with extended tails (triangles), and the $A_{5'5}$ lipid (pluses). Friction coefficients obtained from the relaxation rate $\gamma_1$ of the thermal undulations, by means of the theory by Seifert and Langer, are plotted at $\Delta v = 0$.

by interdigitation strengthens the interaction between the two monolayers and is responsible for the growth of the intermonolayer friction with increasing asymmetry. The intermonolayer friction coefficients were also deduced from the slow relaxation rates $\gamma_1$, see Eq. (5.8), of the thermal bilayer undulations with the smallest wavenumber, $q = 2\pi/L_{\|}$. The small differences between these friction coefficients, indicated in the graph by the markers at $\Delta v = 0$, and those calculated for the lowest slip velocity can be accounted for by several causes. In the Seifert-Langer theory, the idea of a smooth midsurface where the monolayers slide past oneanother becomes obscured with increasing tail asymmetry, and the assumption $d = h/4$ might be less well founded. Sampling deficiencies of the timecorrelation functions were minimized by prolonging the lengths of all simulations beyond $t_{\mathrm{simu}} \geq 50\gamma_1^{-1}$. In the shear simulations with the lowest shear rates it is difficult to extract an accurate slip velocity $\Delta v$ and solvent shear rate $\dot{\gamma}_w$, see Eq. (5.7), because the motions of the amphiphilic and solvent particles, respectively, are dominated by thermal noise rather than by the collective shear flow. Nevertheless, the

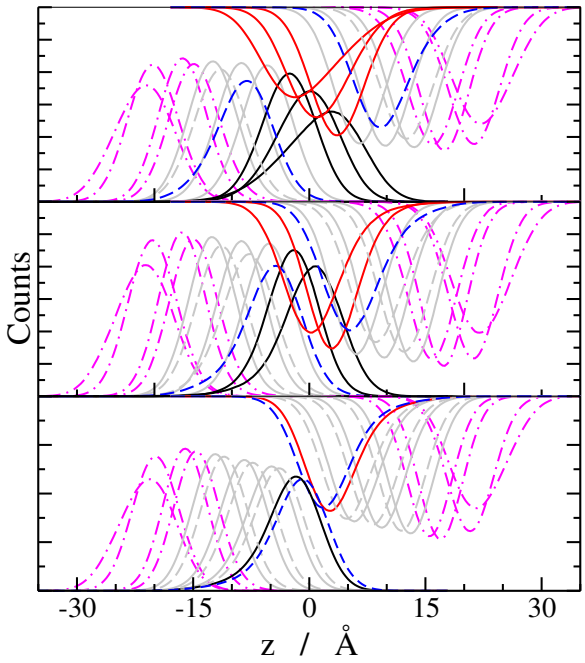


Figure 5.8: Probability distributions of the amphiphilic particles along the bilayer normal, for $A_{44}$ (bottom), $A_{55}$ (middle) and $A_{62}$ (top), with the particles of the first (long) tail as solid lines, the particles of the second (short) tail as dashed lines, and the head particles as dash-dotted lines. The terminal and interdigitating particles are marked by dark lines, while light lines are used for the remaining tail particles. The asymmetric lipids form a so-called partially interdigitated bilayer, in which a long tail packs end-to-end with a short tail from the opposing leaflet.

simulations clearly indicate that the intermonolayer friction coefficients are independent of the slip velocity.

In the simulations of symmetric lipids we compared the reference lipid $A_{44}$ against three lipids with longer tails: $A_{55}$, $A_{66}$ and $A_{77}$. Along this series of lipids, the equilibrium dimensions of the bilayer gradually grow according to $a_o = (0.655 + 0.009i)\,\mathrm{nm}^2$ and $h = (19 + 6i)$ Å, with $i$ the number of particles per tail. The ratios of bending rigidity to elastic modulus are well fitted by $(\kappa/K_A)^{1/2} = \alpha(h - h_0)$, with $\alpha = 0.16$ and $h_0 = 1.2\,\mathrm{nm}$, in good agreement with the $\alpha = 1/\sqrt{24}$ and $h_0 = 1\,\mathrm{nm}$ obtained by the experiments and theory of Rawicz *et al.*[58] Simulations under parallel shear revealed that the intermonolayer friction coefficients vary by less than 50% between the four lipids, see Fig. 5.7. Because both tails are of equal length, the monomer distributions along the bilayer normal are similar to that of the $A_{44}$ membrane discussed before, and there is no interdigitation of tails from opposing leaflets. The distributions of the extremal tail particles become wider with increasing tail length, and the distances between their peaks reduce, which suggests a slightly rougher interface and hence a higher intermonolayer friction for the longer tails. This trend is indeed observed at the slip velocity of 0.25 nm/ns, but curiously the friction coefficients obtained from the thermal undulations are sorted in the reverse order.

The surface shear viscosities of bilayers with symmetric lipids rises rapidly with increasing tail length, see Fig. 5.6, as is to be expected when the number of lateral interactions between neighbouring lipids increases. For the $A_{44}$ and $A_{55}$ lipids the surface viscosity is virtually shear-rate independent, and there is a good agreement between the results of equilibrium and non-equilibrium simulations. A pronounced shear-thinning is observed for bilayers with the longer $A_{66}$ and $A_{77}$ lipids. The shear-thinning is probably caused by the ordering of the lipids in the bilayer, and perhaps enhanced by flow-induced ordering, because the bulk tail liquids, $C_i$ with $4 \leq i \leq 7$, behave like Newtonian liquids over the same range of shear rates. Interestingly, the shear viscosities of these liquids are linear in the tail length, $\eta_{\mathrm{tail}} = (4i - 8) \cdot 10^{-4}\,\mathrm{Pa\,s}$. The lipids with long tails also reveal a discrepancy between the viscosities at low shear rates and those derived from diffusion coefficients by the Saffman theory, which indicates that the limits of this theory have been reached.

In our final lipid model, denoted as $A_{5'5}$, a mono-unsaturated tail is mimicked by reducing the equilibrium angle at the central particle of the tail to $\theta_0 = 130°$ and by stiffen-

ing the bending potential of this particular angle to $K_{\text{angle}} = 250\,\text{kJ/mol}$. The impact of the boomerang-shaped tail is modest; Figs. 5.6 and 5.7 show that the surface shear viscosity and the intermonolayer friction coefficient, respectively, have increased only slightly relative to its closest saturated counterpart, the $A_{55}$ lipid.

## 5.6 Discussion and conclusions

The flow properties of bilayer membranes have been studied, for a variety of coarse grained lipid models, using molecular dynamics simulations. Surface shear viscosities $\eta_s$ were calculated from simulations of bilayers exposed to a perpendicular shear, and from the lateral self-diffusion of the lipids by means of Saffman's theory. Intermonolayer friction coefficients $b$ were obtained from bilayers under parallel shear, and from the relaxation rates of thermally undulating bilayers using the theory by Seifert and Langer. The generally good quantitative agreement between the results of the equilibrium and non-equilibrium simulations is interpreted as support for the two aforementioned theories.

The single-tail coarse-grained lipid model by Goetz and Lipowsky has been extended here with pairwise additive friction and random forces, because the bilayer dynamics obtained with the original model was considerably faster than that of experimental bilayers. Although the model now reproduces the experimental viscosities of water and liquid alkanes, the slowing down of the bilayer dynamics is insufficient to recover quantitative agreement with experimental data. Interestingly, the surface shear viscosity and intermonolayer friction coefficient are of the same order of magnitude as those obtained with the double-tailed lipid model recently introduced by Marrink *et al.*. Our variations on the latter model, by changing the tail lengths and introducing asymmetry, achieve only a five-fold increase of $\eta_s$ and $b$. We are therefore led to believe that the reported values are generic for coarse-grained lipid models.

A layer of bulk liquid with viscosity $\eta_l$ and thickness $h$ is readily shown to posses a 'surface' shear viscosity $\eta_s = \eta_l h$ under perpendicular shear flow and a 'friction' coefficient $b = \eta_l/h$ under parallel shear flow, where in the latter case the velocity difference over the layer is interpreted as $2\Delta v$. By comparing the bilayers with symmetric lipids against these rules of thumb, we find that the low shear-rate results are adequately described by $\eta_s \approx$

$3\eta_{\text{tail}}h$ and $b \approx 12\eta_{\text{tail}}/h$, with $\eta_{\text{tail}}$ the viscosity of a bulk liquid of tails. The prefactors appearing in these expressions reflect that the bilayer is not a simple bulk liquid of tails, but that the lipids are ordered in a bilayer structure. Experimental data yield prefactors of the order of 100 to 1000, with the intermonolayer friction requiring a higher prefactor than the surface viscosity,[14] suggesting that the impact of ordering on $\eta_s$ and $b$ is considerably higher for real lipids than for the coarse-grained model lipids studied here. We suspect that these differences are caused by the weakness of coarse-grained models to accurately mimic the detailed interactions between alkanes, and hence their packing in dense phases. This is also illustrated by the viscosities of the bulk $C_i$ liquids, which we found to be linear in the length $i$ for chains of 4 to 7 particles. The experimental viscosities,[56] however, rise rapidly with increasing chain length, whilst $n$-tetracosane ($i = 6$) and longer linear alkanes are in a wax-like state at the simulation temperature of 323 K. In the ordered bilayer structure a similar transition is observed at an even lower tail length, with DPPC ($i = 4$) in the liquid-crystalline phase and DSPC ($i = 4.5$) in the gel phase at 323 K. The coarse-grained lipids, for which no chain-length induced transitions were observed, are apparently less sensitive to ordering and dense packing effects, which also explains their relatively low surface shear viscosity and intermonolayer friction coefficient. A quantitative reproduction of the flow properties of membranes by computer simulations probably requires an atomistically detailed model.

By varying the tail lengths of a double-tailed lipid, we observe two clear trends for the flow properties of bilayers. The intermonolayer friction coefficient is sensitive to the asymmetry of the tails, which roughens the interface between the two monolayers by interdigitation of the longer tails. The surface shear viscosity is modulated by the combined lengths of the two tails, and hardly varies with the asymmetry of the tails. In view of the above reservations on the accuracy of the CG model, it is not evident whether bilayers of real lipids will display similar behaviour. The experimental data at our disposal are inconclusive in this respect. Finally, we express the expectation that the current work inspires future experimental and simulation studies on the flow properties of bilayers in relation to their lipid composition.

# Bibliography

[1] W. M. Becker and D. W. Deamer. *The world of the cell*. Benjamin/Cummings Publishing Company, Redwood City, CA, 1991.

[2] U. Seifert. Configurations of fluid membranes and vesicles. *Adv. in Phys.*, 46:13–137, 1997.

[3] L. Stryer. *Biochemistry*. W. H. Freeman and Comp., New York, NY, 4 edition, 1995.

[4] P. G. Saffman. Brownian motion in thin sheets of viscous fluid. *J. Fluid Mech*, 73:593–602, 1976.

[5] M. J. Saxton and K. Jacobson. Single particle tracking: applications to membrane dynamics. *Ann. Rev. Biophys. Biomol. Struct.*, 26:373–399, 1997.

[6] R. E. Waugh. Surface viscosity measurements from large bilayer vesicle tether formation. experiments. *Biophys. J.*, 38:29–37, 1982.

[7] R. Dimova, C. Dietrich, A. Hadjiisky, K. Danov, and B. Pouligny. Falling ball viscosimetry of giant vesicle membranes: finite-size effects. *Eur. Phys. J. B*, 12:589–598, 1999.

[8] R. Dimova, B. Pouligny, and C. Dietrich. Pretransitional effects in dimyristoylphosphatidylcholine vesicle membranes: optical dynamometry study. *Biophys. J.*, 79:340–356, 2000.

[9] J. M. Dustman, R. S. Casas, H. A. Scheidt, N. V. Eldho, W. E. Teague, and K. Gawrisch. Lipid hydrocarbon chain dynamics and lateral diffusion in a polyunsaturated lipid matrix. *Biophys. J.*, 88:27a, 2005.

[10] A. Filippov, G. Orädd, and G. Lindblom. The effect of cholesterol on the lateral diffusion of phospholipids in oriented bilayers. *Biophys. J.*, 84:3079–3086, 2003.

[11] S. Ladha, Mackie A. R., L. J. Harvey, D. C. Clark, E. J. A. Lea, M. Brullemans, and H. Duclohier. Lateral diffusion in planar lipid bilayers: a fluorescene recovery after photobleaching investigation of its modulation by lipid composition, cholesterol, or alamethicin content and divalent cations. *Biophys. J.*, 71:1364–1373, 1996.

[12] W. L. C. Vaz, R. M. Clegg, and D. Hallmann. Translational diffusion of lipids in liquid crystalline phase phosphatidylcholine multibilayers. a comparison of experiment with theory. *Biochem.*, 24:781–786, 1985.

[13] K. Weisz, G. Gröbner, C. Mayer, J. Stohrer, and G. Kothe. Deuteron nuclear magnetic resonance study of the dynamic organization of phospholipid/cholesterol bilayer membranes: molecular properties and viscoelastic behavior. *Biochem.*, 31:1100–1112, 1992.

[14] E. Evans and A. Yeung. Hidden dynamics in rapid changes of bilayer shape. *Chem Phys. Lipids*, 73:39–56, 1994.

[15] E. Evans, A. Yeung, R. Waugh, and J. Song. Dynamic coupling and nonlocal curvature elasticity in bilayer membranes. *Springer Proceedings in Physics*, 66:148–153, 1992.

[16] U. Seifert and S. A. Langer. Viscous modes of fluid bilayer membranes. *Europhys. Lett.*, 23:71–76, 1993.

[17] U. Seifert and S. A. Langer. Hydrodynamics of membranes: the bilayer aspect and adhesion. *Biophys. Chem.*, 49:13–22, 1994.

[18] A. Yeung and E. Evans. Unexpected dynamics in shape fluctuations of bilayer vesicles. *J. Phys. II France*, 5:1501–1523, 1995.

[19] Y. A. Chizmadzhev, D. A. Kumenko, P. I. Kuzmin, L. V. Chernomordik, J. Zimmerberg, and F. Cohen. Lipid flow through fusion pores connecting membranes of different tensions. *Biophys. J.*, 76:2951–2965, 1999.

[20] R. Merkel, E. Sackmann, and E. Evans. *J. Phys. (Paris)*, 50:1535, 1989.

[21] W. Pfeiffer, S. König, J. F. Legrand, T. Bayerl, D. Richter, and E. Sackmann. Neutron spin echo study of membrane undulations in lipid multibilayers. *Europhys. Lett.*, 23:457–462, 1993.

[22] T. Pott and P. Méléard. The dynamics of vesicle thermal fluctuations is controlled by intermonolayer friction. *Europhys. Lett.*, 59:87–93, 2002.

[23] A. Yeung, private communication.

[24] K. M. W. Keough and P. J. Davis. Gel to liquid-crystalline phase transitions in water dispersions of saturated mixed-acid phosphatidylcholines. *Biochem.*, 18:1453–1459, 1979.

[25] I. W. Levin, T. E. Thompson, Y. Barenholz, and C. Huang. Two types of hydrocarbon chain interdigitation in sphingomyelin bilayers. *Biochem.*, 24:6282–6286, 1985.

[26] J. Mattai, P. K. Sripada, and G. G. Shipley. Mixed-chain phosphatidylcholine bilayers: structure and properties. *Biochem.*, 26:3287–3297, 1987.

[27] L. Saiz, S. Bandyopadhyay, and M. L. Klein. Towards an understanding of complex biological membranes from atomistic molecular dynamics simulations. *Biosci. Rep.*, 22:151, 2002.

[28] D. P. Tieleman, S. J. Marrink, and H. J. C. Berendsen. A computer perspective of membranes: Molecular dynamics studies of lipid bilayers systems. *Biochim. Biophys. Acta*, 1331:235–270, 1997.

[29] I. R. Cooke, K. Kremer, and M. Deserno. Tunable generic model for fluid bilayer membranes. *Phys. Rev. E*, 72:011506, 2005.

[30] S. E. Feller and R. W. Pastor. Constant surface tension simulations of lipid bilayers: the sensitivity of surface areas and compressibilities. *J. Chem. Phys.*, 111:1281–1287, 1999.

[31] R. Goetz and R. Lipowsky. Computer simulations of bilayer membranes: Self-assembly and interfacial tension. *J. Chem. Phys.*, 108:7397–7409, 1998.

[32] S.J. Marrink, A. H. de Vries, and A. E. Mark. Coarse grained model for semiquantative lipid simulations. *J. Phys. Chem. B*, 108:750, 2004.

[33] A. Imparato, J. C. Schillcock, and R. Lipowsky. Lateral and transverse diffusion in two-component bilayer membranes. *Euro. Phys. J. E*, 11:21–28, 2003.

[34] P. S. Niemelä, M. T. Hyvönen, and I. Vattulainen. influence of chain length and unsaturation on sphingomyelin bilayers. *Biophys. J.*, 90:851–863, 2006.

[35] E. Lindahl and O. Edholm. Mesoscopic undulations and thickness fluctuations in lipid bilayers from molecular dynamics simulations. *Biophys. J.*, 79:426–433, 2000.

[36] S. A. Shkulipa, W. K. den Otter, and W. J. Briels. Surface viscosity, diffusion, and intermonolayer friction: simulating sheared amphiphilic bilayers. *Biophys. J.*, 89:823–829, 2005.

[37] S. A. Shkulipa, W. K. den Otter, and W. J. Briels. Thermal undulations of lipid bilayers relax by intermonolayer friction at submicrometer length scales. *Phys. Rev. Lett.*, 96:178302, 2006.

[38] W. Helfrich. *Z. Naturforsch. C*, 28:693, 1973.

[39] S. A. Safran. *Statistical Thermodynamics of Surfaces, Interfaces and Membranes*. Addison-Wesley, Reading, MA, 1994.

[40] W. K. den Otter. Area compressibility and buckling of amphiphilic bilayers in molecular dynamics simulations. *J. Chem. Phys.*, 123:214906, 2005.

[41] M. P. Allen and D. J. Tildesley. *Computer Simulation of Liquids*. Oxford University Press, Oxford, U. K., 1987.

[42] S. A. Shkulipa, W. K. den Otter, and W. J. Briels. In preparation. *Journal*, Volume:Page, Year.

[43] F. Brochard and J.F. Lennon. *J. Phys. (Paris)*, 11:1035, 1975.

[44] L. Kramer. Theory of light scattering from fluctuations of membranes and monolayers. *J. Chem. Phys.*, 55:2097–2105, 1971.

[45] C. W. Gardiner. *Handbook of stochastic methods : for physics, chemistry and the natural sciences*. Springer-Verlag Inc., New York, NY, 1985.

[46] R. D. Groot and P. B. Warren. Dissipative particle dynamics: bridging the gap between atomistic and mesoscopic simulation. *J. Chem. Phys.*, 107:4423–4435, 1997.

[47] P. J. Hoogerbrugge and J. M. V. A. Koelman. Simulating microscopic hydrodynamic phenomena with dissipative particle dynamics. *Europhys. Lett.*, 19:155, 1992.

[48] W. Smith and T. R. Forester. Dlpoly2.0: A general-purpose parallel molecular dynamics simulation package. *J. Mol. Graphics*, 14:136–141, 1996.

[49] W. K. den Otter and W. J. Briels. The bending rigidity of an amphiphilic bilyer from equilibrium and nonequilibrium molecular dynamics. *J. Chem. Phys.*, 118:4712, 2003.

[50] R. Goetz, G. Gompper, and R. Lipowsky. Mobility and elasticity of self-assembled membranes. *Phys. Rev. Lett.*, 82:221, 1999.

[51] T. V. Tolpekina, W. K. den Otter, and W. J. Briels. Nucleation free energy of pore formation in an amphiphilic bilayer studied by molecular dynamics simulations. *J. Chem. Phys.*, 121:12060–12066, 2004.

[52] T. V. Tolpekina, W. K. den Otter, and W. J. Briels. Simulations of stable pores in membranes: System size dependence and line tension. *J. Chem. Phys.*, 121:8014–8020, 2004.

[53] R. C. Weast (chief editor). *CRC handbook of chemistry and physics*. CRC, Cleveland, OH, 50 edition, 1970.

[54] R. D. Groot and K. L. Rabone. Mesoscopic simulation of cell membrane damage, morphology change and rupture by nonionic surfactants. *Biophys. J.*, 81:725–736, 2001.

[55] P. S. Tofts, D. Lloyd, C. A. Clark, G. J. Barker, G. J. M. Parker, P. McConville, C. Baldock, and J. M. Pope. Test liquids for quantitative mri measurements of self-diffusion coefficient in vivo. *Magn. Reson. Med.*, 43:368–374, 2000.

[56] A. J. Queimada, S. E. Quiñones Cisneros, I. M. Marrucho, J. A. P. Coutinho, and E. H. Stenby. Viscosity and liquid density of asymmetric hydrocarbon mixtures. *Int. J Thermophys.*, 24:1221–1239, 2003.

[57]

[58] W. Rawicz, K. C. Olbrich, T. McIntosh, D. Needham, and Evans E. Effect of chain length and unsaturation on elasticity of lipid bilayers. *Biophys. J.*, 79:328–339, 2000.

# 6 Buckling and persistence length of an amphiphilic worm from molecular dynamics simulations

*A worm-like micelle of coarse-grained amphiphilic molecules is simulated with molecular dynamics. We demonstrate that our worm is inherently stable,* i. e. *it does not depend on periodic boundary conditions for its continued survival, which sets it apart from some, and perhaps even all, previously simulated worms. The worms are observed to buckle under sufficiently strong compression forces. The persistence length and bending rigidity follow from analysing the thermal undulations of a tensionless worm. System size dependencies of the elastic modulus of the worm, as reported for amphiphilic bilayers, are eliminated by explicitly calculating the arc length of the worm.* *

## 6.1 Introduction

Amphiphilic molecules in water spontaneously assemble into aggregates ranging from near-spherical micelles and cylindrical worm-like micelles to bilayers and vesicles.[2] This process is driven by a minimisation of the exposure to the water of the hydrophobic tails of the amphiphiles, by shielding them with the hydrophilic heads. The size and shape of the aggregates depend on a number of parameters, including the chemical composition of the amphiphile (charge and relative size of the head group, one or two tails, flexibility of the tails), the concentration and the presence of counter ions. No chemical bonds are formed within the aggregates, hence they behave as one dimensional (worm) or two dimensional

∗ The work described in this chapter previously appeared in J. Chem. Phys. **119**, 2363 (2003) [1].

(bilayer) liquids of amphiphiles, and they break up and regroup relatively easily.

Computer simulations have proven very useful in advancing our understanding of the properties of amphiphilic aggregates. Molecular dynamics simulations in full atomic splendour require a large number of atoms and a powerful computer; many simulations therefore resort to coarse grained models in which a molecule is represented by a small number of beads. [3] A number of such studies have concentrated on the spontaneous growth process. Randomly distributed surfactant molecules were observed to assemble into micelles, worms or bilayers, depending on their concentration. [4, 5] Because of their relevance as cell membranes in biological tissues, most simulation studies to date concern bilayers. [4, 6, 7, 8, 9, 10, 11, 12] Simulations of worms are exceedingly rare: they have been observed by a number of authors, [4, 5, 13, 14] and most were found to last for the course of the simulation in boxes with periodic boundary conditions, but no discussion of their mechanical properties exists.

This absence is all the more striking considering the widespread interest in industry in the rheological properties of solutions containing worm-like micelles.[15] In the oil producing industry, for instance, amphiphilic solutions are considered a viable and environmentally acceptable alternative for the currently used fracturing fluids.[16] The visco-elasticity of the solution is to a large extent determined by the mechanical properties of the worms, *i. e.* their bending rigidity and elastic modulus, and their capacity to break up under high tension and to reconnect under reduced tension conditions.[15] The ability to calculate these properties from the molecular structure of the amphiphile will make a significant contribution to the understanding of the viscoelastic properties of these fluids. These data can then be used as the input of a coarse model, in which the entire worm is regarded as a chain of beads connected by springs that allow for scission and recombination, from which the rheological properties are obtained. Although simulations of worms on this level have been discussed by a number of authors,[17, 18] it has never been tried to calculate the characteristic input parameters from the underlying molecular model.

In this contribution we calculate the mechanical properties of a coarse-grained model surfactant. The Helfrich model by which these properties are defined is discussed in Section 6.2. In Section 6.3 Lipowsky's model of the amphiphile is introduced. The problems that arise when using this parameter set for a worm-like micelle are discussed, and an expe-

dient is presented. The simulation results obtained with the modified potential are presented in Section 6.4, and discussed in Section 6.5.

## 6.2 Theory

A worm of $N$ molecules is oriented parallel to the $z$-axis of a periodic simulation box of height $L_\parallel$ and a square ground plane with sides $L_\perp$. Regarding the worm as a single smooth line, $(x(z), y(z), z)$, with $z$ the independent parameter, the local curvature at every point along the line is readily expressed in terms of the second derivatives of $x$ and $y$ with respect to $z$. The bending free energy then is proportional to the line integral of the squared curvature,

$$f_{bend}[x,y] = \frac{\kappa}{2}\int_0^{L_\parallel}\left(\frac{\partial^2 x}{\partial z^2}\right)^2 + \left(\frac{\partial^2 y}{\partial z^2}\right)^2 dz, \tag{6.1}$$

with $\kappa$ the bending rigidity. The undulations of the worm are conveniently expanded in a Fourier series,

$$x(z) = x_0 + \sum_{n\neq 0} c_{x,n}\exp[iq_n z], \tag{6.2}$$

with wave number $q_n = 2\pi n/L_\parallel$, and $n$ running over both positive and negative integers, but excluding zero. The realness of $x$ implies that $c_{x,-n} = c^*_{x,n}$. Similar expressions apply to $y(z)$ and $c_{y,n}$. Any deviation of the curve length $L$ from its equilibrium value $L_0$ also contributes to the free energy, with half the elastic modulus $K_L$ acting as the proportionality constant. To lowest order in the Fourier coefficients, the free energy of a given configuration thus reads in the Helfrich model as

$$f(\{c_{x,n}\},\{c_{y,n}\}) = \frac{16\pi^4\kappa}{L_\parallel^3}\sum_{n\geq 1}\left(|c_{x,n}|^2 + |c_{y,n}|^2\right)n^4 + \frac{K_L}{2L_0}(L-L_0)^2, \tag{6.3}$$

where the arc length $L$ still is a function of $L_\parallel$ and the Fourier coefficients. The total free energy $F$ of the worm follows by integrating over all possible configurations,

$$F = -k_B T \ln\left\{\int\int \exp(-\beta f[x,y])DxDy\right\}, \tag{6.4}$$

with Boltzmann's constant $k_B$, temperature $T$ and $\beta = 1/k_B T$. Unfortunately, this expression is too difficult for a direct evaluation, so an alternative route is needed to arrive at the desired mechanical properties of the worm.

Under elongation or compression, $|L - L_0| \gg 0$, the free energy $F$ is dominated by the elastic term. Neglecting the bending term altogether, the free energy change under a box deformation at constant volume, $V = L_\parallel L_\perp^2$, reads as

$$-\Delta p \frac{V}{L_\parallel} = \left(\frac{\partial F}{\partial L_\parallel}\right)_{N,V,T} \approx \frac{K_L}{L_0}(L - L_0)\frac{\partial L}{\partial L_\parallel}. \tag{6.5}$$

The left hand side follows from the usual thermodynamic definition of the pressure as a free energy derivative, with $\Delta p = p_{zz} - \frac{1}{2}(p_{xx} + p_{yy})$ and $p_{ij}$ the stress tensor. The worm is said to be in the tension-less state when $\Delta p = 0$, so $L = L_0$ and $L_\parallel = L_{\parallel 0}$. Under these conditions the stretching free energy vanishes in Eq. (6.3). As the remaining bending free energy is quadratic in its arguments, all modes are decoupled and so are the real and imaginary parts of their Fourier coefficients. The equipartition theorem then states that the structure factors of a tension-less worm scale as

$$S_x(n) = \left\langle |c_{x,n}|^2 \right\rangle = 2\left\langle \mathrm{Re}^2(c_{x,n}) \right\rangle = \frac{k_B T}{L_\parallel \kappa} q_n^{-4}. \tag{6.6}$$

Similar expressions hold for $S_y(n)$ and for the imaginary parts. An observation of Eqs. (6.5) and (6.6) in our simulations would validate the above derivation, and yield the desired mechanical properties. The first to succesfully use this kind of approach were Goetz, Gompper and Lipowsky[9] in their study of a bilayer. Note that in the case of bilayers it is standard practice to equate the area of the bilayer to the area of the ground plane of the simulation box. [4, 7, 9, 10, 11, 12] For the worm, this assumption would translate into $L = L_\parallel$ and

$$-\Delta p \frac{V}{L_\parallel} = \frac{K_L}{L_{\parallel 0}}(L_\parallel - L_{\parallel 0}). \tag{6.7}$$

We stress, however, the importance of distinguishing between $L$ and $L_\parallel$, for reasons that will become apparent below.

The average arc length of the tensionless worm follows from averaging the well-known expression for the length of a curve,

$$\begin{aligned} L_0 &= \left\langle \int_0^{L_{\parallel 0}} \left[1 + \left(\frac{\partial x}{\partial z}\right)^2 + \left(\frac{\partial y}{\partial z}\right)^2\right]^{1/2} dz \right\rangle \\ &\approx L_{\parallel 0} + \frac{4\pi^2}{L_{\parallel 0}} \sum_{n \geq 1} n^2 \left( \left\langle |c_{x,n}|^2 \right\rangle + \left\langle |c_{y,n}|^2 \right\rangle \right). \end{aligned} \tag{6.8}$$

In the last step we Taylor expanded the square root, inserted the Fourier expansions of $x(z)$ and $y(z)$, and integrated over $z$ using the orthogonality of the basis set. For the averages we now substitute Eq. (6.6). The resulting summation converges to

$$L_0 = L_{\|0} + L_{\|0}^2 \frac{k_B T}{12\kappa}, \tag{6.9}$$

in the (unphysical) limit of $n$ going to infinity.

## 6.3 Simulation details

The simulation model we used is based on the model of Goetz *et al.*[4, 9] An amphiphilic architecture is chosen in which the head is represented by a single bead ($h$) and the tail is reduced to four beads ($t$) representing roughly three $CH_2$ units each. The solvent consists of loose water beads ($w$) roughly representing two water molecules. Interactions between like particles, as well as the hydrophilic head-water interactions are modelled by a Lennard-Jones potenial, $\Phi_{ij}^{LJ}(r) = 4\varepsilon[(\sigma_{ij}/r)^{12} - (\sigma_{ij}/r)^6]$. The hydrophobic tail-water and tail-head interactions are modelled by a purely repulsive potential, $\Phi_{ij}^{rep}(r) = 4\varepsilon(1.05\sigma_{ij}/r)^9$. In the original parameter set all six diameters $\sigma_{ij}$ are identical to $\sigma$. The non-bonded forces are implemented in a shifted-force fashion, ensuring a smooth truncation of the energy and the force at the cut-off distance of $2.5\sigma_{ij}$. All particles have the same mass $m$. Consecutive beads in an amphiphile are held together by harmonic springs, $\Phi_{ij}^{bond}(r) = 5000\varepsilon\sigma^{-2}(r - \sigma_{ij})^2$, while there are no bending or dihedral potentials. A Nosé-Hoover thermostat maintains a temperature of $T = 1.35\varepsilon/k_B$, the density is fixed at 2 particles per $3\sigma^3$. The time step is $\tau/2000$, with $\tau = \sqrt{m\sigma^2/\varepsilon}$ the unit of time. Simulations were run using version 2.0 of the DL_POLY package.[19] A link to experimental values is achieved by $\sigma = 1/3$ nm, $\varepsilon = 2$ kJ/mol and $m = 36$ g/mol, in which case $T = 325$ K.[4] These conversion factors only serve as a rough indication, and are not meant to be definitive.

Using this parameter set, Goetz *et al.*[4] observed the spontaneous formation of worms from random solutions. We prepared a simulation box of a size comparable to theirs ($N = 90$, $L_\| = 12\sigma$ and $L_\perp = 18.2\sigma$) with the amphiphiles neatly arranged in a cylindrical configuration. After a prolonged equilibration, the worm-like structure proved to survive in a periodic box with fixed dimensions. We noticed, however, a considerable pressure difference $\Delta p$ between the parallel and perpendicular directions, indicating that the worm wanted to contract.

To reduce this line tension, we ran simulations with a modified Berendsen barostat[20] which scaled the box side $L_{\|}$ every time step by a factor proportional to the pressure difference. The two perpendicular sides $L_{\perp}$ were scaled simultaneously, keeping the total volume of the box fixed. During the relaxation the parallel axis gradually diminished, while the worm turned into a flattened worm, and eventually became a bilayer. Having observed this behaviour in a number of boxes with different sizes and concentrations, we concluded that the current parameter set is not able to form a stable worm. The formation of worm-like structures from random starting configurations in boxes of fixed dimensions, and the longevity of these structures, are an artefact of the periodic boundary conditions. On the basis of these results we speculate that other simulations in which worms have been observed may be hampered by the same problem. A related interesting discussion of boundary effects on the micelle to worm transition appears in Marrink *et al.*[5]

To stabilise the worm, we tapered the amphiphiles by increasing the size of the head groups, $\sigma_{hh}$, at constant $\sigma_{tt}$ and $\sigma_{ww}$. The combination rule $\sigma_{ij} = \sqrt{\sigma_{ii}\sigma_{jj}}$ was applied to interactions between unlike particles. Runs at several values of $\sigma_{hh}$ indicated that head particles with a volume of at least four times that of tail particles, *i. e.* $\sigma_{hh} = \sqrt[3]{4}\sigma$, are needed to yield an inherently stable worm. For a box of 90 amphiphiles and 2192 water particles, the manostated simulation then converged to a stable tension-less worm with $L_{\|} \approx 13.5\sigma$. As a further test, we ran simulations with non-periodic amphiphilic aggregates, *i. e.* aggregates which were terminated by caps or an edge because the box was too large to permit periodic structures. Starting configurations were made either by hand, or by self-assembly from a randomly dissolved box. In each case, we observed stable cylindrical structures for the potential with the enlarged head groups. The original amphiphiles, on the other hand, always formed flattened micelles and disk-like bilayers.

An alternative route to making cone-shaped amphiphiles would be to retain the original parameter set, but to increase the number of head particles. The linear $h_2t_4$ amphiphile is hardly more conical than the original $ht_4$, and therefore does not yield a stable worm either. But a "forked" $h_2t_4$ molecule, with both heads bonded to the first tail particle and to oneanother by the aforementioned $\Phi_{ij}^{bond}(r)$, does form stable worms. We have not pursued this type of molecule any further, though it would be interesting to investigate how this asymmetric head group affects the ordering and dynamics of amphiphiles within a worm.

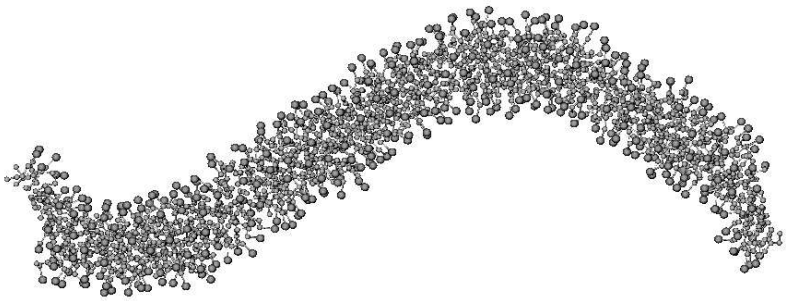

Figure 6.1: Snapshot of a micellar worm of 450 amphiphiles in the tension-less state. The surrounding solvent particles are not shown.

About two dozen simulation boxes were made, ranging from 90 upto 450 amphiphiles arranged in a cylindrical shape, with box lengths distributed around their anticipated equilibrium lengths. Each box had the same amphiphile to solvent ratio. The boxes were thoroughly equilibrated, followed by production runs of at least 10 million steps. A typical configuration is shown in Fig. 6.1. By evaluating the mean square displacements of some runs, we verified that the amphiphiles in these worm still move as in a two dimensional liquid confined to a cylindrical surface.

In order to apply Eq. (6.6) to the modes of an undulating worm, one needs to extract the Fourier coefficients from the particle coordinates $(x_i, y_i, z_i)$. We divided the box into $J$ slabs perpendicular to the $z$ axis, calculated the averaged coordinates $X_j = \langle x_i \rangle_j$ and $Y_j = \langle y_i \rangle_j$ of all amphiphilic particles (heads and tails) in the $j^{th}$ slab, and applied an inverse Fourier transform to the resulting $(X_j, Y_j, Z_j)$, with $Z_j = (j - \frac{1}{2})L_{\|}/J$ the equidistant centres of the slabs. The sum of the distances between these points served as our estimate of the arc length of the worm. The ensuing $S_x(n)$ and $L$ were verified to be virtually independent of the number of slabs over a range of $J$-s.

## 6.4 Results

As explained in Section 6.2, our first objectives are the elastic modulus and the tensionless state. Figure 6.2 shows the calculated pressure differences as a function of the box height.

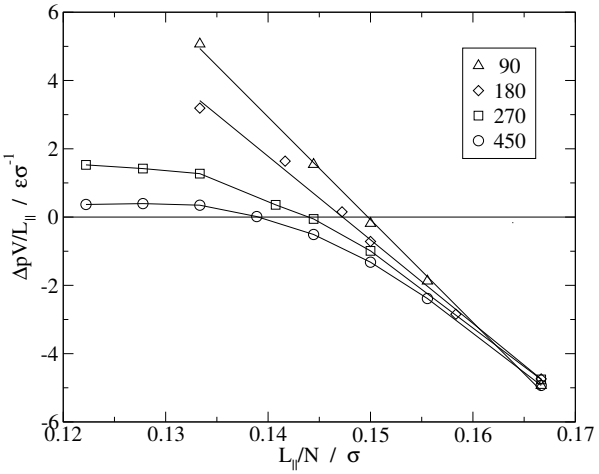


Figure 6.2: Pressure difference $\Delta p$ between the directions parallel and perpendicular to the worm, as a function of the height $L_{\|}$ of the simulation box, normalised by the number of amphiphiles $N$. Note how the pressures, *i. e.* the forces opposing compression, reach a maximum for the long worms.

The linear relationships observed for the smaller boxes of 90 and 180 amphiphiles agree with Eq. (6.7). But the different slopes and intercepts suggest that the elastic modulus $K_L$ and the average length per amphiphile $l_{\|0} = L_{\|0}/N$ decrease as the system size increases. Similar size dependencies have been reported for the elastic modulus and equilibrium area of bilayers, [11, 12] where an approximation analogous to $L = L_{\|}$ is used. Although a system size dependency of $K_L$ as defined by Eq. (6.7) does not come entirely unexpected, the undulations could for instance still play a minor role, the basic idea behind the Helfrich model is that the elastic modulus $K_L$ is truly constant. For bigger worms the pressure difference is no longer linear in the box height, but reaches a plateau under compression. Again, large bilayers behave in a similar fashion.[21] These findings clearly disagree with Eq. (6.7), and the question rises whether the assumptions made in the derivation of that expression are justified.

In Fig. 6.3 the arc length of the worm is plotted against the height of the box. Under elongation, the arc lengths of all worms are linear in the box height, with slopes approaching unity, $\partial L/\partial L_{\|} \approx 1$. The plot also shows that short worms are truly compressible, their

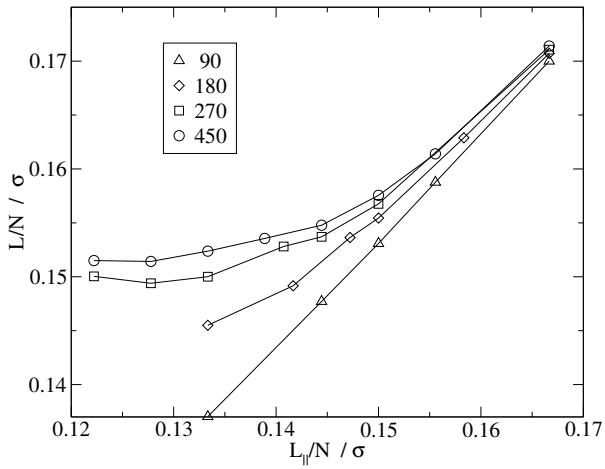


Figure 6.3: Average arc length of the worm versus the box height, for a number of system sizes. The long worms clearly buckle under compression, while the short worms behave almost elastically.

arc lengths steadily diminish with $L_{\|}$, while the arc lengths of the longer worms eventually stabilise. This constant length, the constant pressure, and the large undulations observed in snap shots of the system, all indicate that the longer worms buckle under compression. By plotting the pressure difference against the arc length in Fig. 6.4, we see that all data points, including those from the buckled worms, coalesce to a single straight line. From the slope of this line we obtained the elastic modulus $K_L = 46\varepsilon/\sigma$ or $4.6 \cdot 10^{-10}$ J/m and the equilibrium length per amphiphile $l_0 = 0.154\sigma$ or 0.51Å. Both are clearly independent of the system size, as predicted by the Helfrich model.

The structure factors of three tension-less worms are presented in Fig. 6.5. At low wave numbers the smallest box shows the start of the $q^{-4}$ regime predicted by Eq. (6.6), which becomes more pronounced in the larger boxes. The coalescence of three simulations onto a single curve indicates that the bending rigidity is essentially independent of the system size (on this length scale, at least). At large wave numbers the structure factors start sampling the local structure of the worm, rather than a smooth overall curvature, giving rise to a departure from theory. From the fit follows a bending rigidity of $\kappa = 52\varepsilon\sigma$ or $5.8 \cdot 10^{-29}$ J m. The

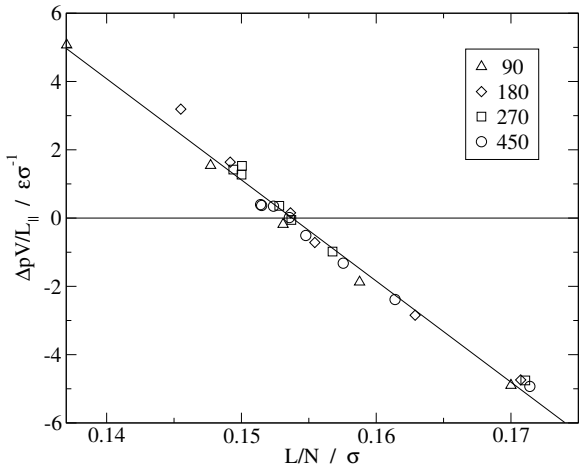


Figure 6.4: Pressure difference $\Delta p$ between the directions parallel and perpendicular to the worm, as a function of the arc length $L$ of the worm, normalised by the number of amphiphiles $N$.

corresponding persistence length[22] $L_p = \kappa/k_BT = 38\sigma$ or 130 Å lies at the lower end of the experimentally observed range of 150 Å to 1500 Å.[23] Note that these conversions of $\sigma$ and $\varepsilon$ to 'real' values are only an order of magnitude estimate. Figure 6.6 shows how this $\kappa$ also leads to a good agreement between the averaged actual curve length and the prediction of Eq. (6.9).

In the theory of elasticity it is derived that a homogeneous isotropic bar is straight under small compression forces, but buckles under the Euler force,[24] $F_E = \pi^2 EI/L_\parallel^2$. The product of Young's modulus $E$ and the second moment $I$ plays the role of the bending rigidity, $\kappa = EI$. This approximate result also follows from the Helfrich expression, under the assumptions that the arc length is constant, $L - L_\parallel \ll L_\parallel$, and there is just one mode with a wave length equal to twice $L_\parallel$. In a periodic system the box height corresponds to the full wave length of the first mode, hence the buckling force is four times bigger,

$$F_E = \frac{4\pi^2\kappa}{(L_\parallel/N)^2} N^{-2}. \tag{6.10}$$

In worm-like micelles curvature already plays an important role before the system buckles,

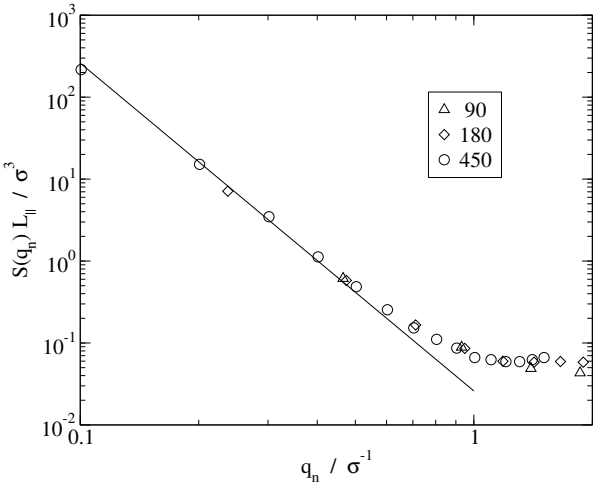


Figure 6.5: Structure factors of three worms in the tensionless state. The fit corresponds to Eq. (6.6).

unlike for rods. The structure factors of a simulated buckled worm still follow the tension-less distribution of Eq. (6.6) with the same $\kappa$, except for the first mode, whose average amplitude has increased. According to Fig. 6.3 the arc length is constant. This suggests that the above assumptions still hold, with the first mode bearing the brunt of the compression force. Figure 6.7 shows that the pressure difference on buckled worms with the same value of $L_{||}/N$ is indeed linear in $N^{-2}$. The proportionality constant is in good agreement with the prediction, which is surprising considering that the above derivation neglected the compressibility of the worm, the presence of other modes besides the first, and the perpetual fluctuations. Interestingly, the fit indicates that a worm of about 650 amphiphiles, or $L_0 \approx 2.7L_p$, already "buckles" under zero pressure. Also, for even longer worms the pressure difference will be negative over a very wide range (and possibly even the entire range) of values of $L_{||}$. This suggests, in our opinion, that beyond this length scale the worm effectively starts to behave as a (short) flexible polymer, with ends that attract oneanother at all distances for entropic reasons.[25]

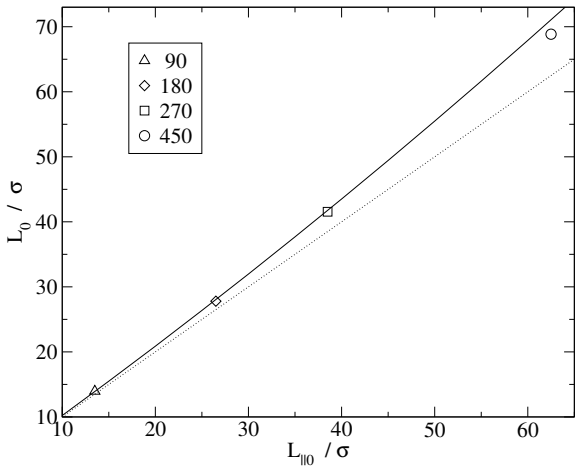


Figure 6.6: The equilibrium arc length as a function of the equilibrium box height. The continuous line shows the theoretical prediction of Eq. (6.9) using the bending rigidity from Fig. 6.5, the dotted line represents $L_0 = L_{\|0}$.

## 6.5 Discussion

A number of authors have observed the spontaneous emergence of worm-like micelles from initially randomly distributed amphiphilic solutions in simulations with periodic boundary conditions. On the basis of a detailed study of one of these worms, we argue that these observations by themselves are insufficient to support the conclusion that the parameter sets used are capable of forming worms. To distinguish between truly stable worms and thinly-pulled taut bilayers, one has to find a state of zero line tension, either by adjusting the dimensions of the periodic simulation box or by making a non-periodic worm (with two endcaps). We have shown that the parameter set used in the Lipowsky model meets these stability criteria only after a fourfold increase of the volume of the head particle.

The averaged thermally-excited structure factors of a tensionless worm in a periodic simulation box scale with the wave number according to $S \propto q^{-4}$, as predicted by the Helfrich model. From the proportionality constant the bending rigidity and persistence length are obtained. Under elongation stress the scaling exponent decreases rapidly, reaching -3.1 at

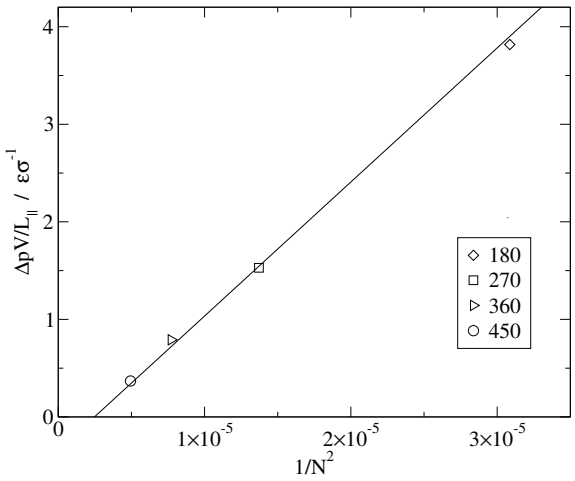


Figure 6.7: The pressure difference of buckled worms, at $L_{\|}/N = 0.122$. The slope is calculated from the prediction of Eq. (6.10), the intercept is fitted.

$L_{\|} = 1.08 L_{\|0}$ and -2.5 at $1.2 L_{\|0}$ (the Helfrich model predicts -2 for $\kappa = 0$), providing an additional test for the stability of the worm.

We observed pronounced differences between the worms response to elongation and compression. When stretched, the undulations of all modes decrease, the contour length increases, and the line tension becomes linear in the height of the simulation box. Under strong compression the undulations of only the first mode increase, while the contour length and the line tension reach a plateau value: the worm buckles. The transitions to these plateaus are very smooth, and their onset and heights vary with the system size. An extrapolation of the buckling pressure suggests that worms of several times the persistence length are always in a highly undulating crumpled or coil-like state. Despite these differences between compression and elongation, we find that both cases agree well with the Helfrich model, provided the length of the worm is properly calculated as the arc length, rather than approximated by the height of the simulation box. The elastic modulus, equilibrium length per amphiphile and the bending rigidity are all indepent of the system size.

# Bibliography

[1] W. K. den Otter, S. A. Shkulpa, and W. J. Briels. *J. Chem. Phys.*, 119:2363, 2003.

[2] W. M. Gelbart, A. Ben-Shaul, and D. Roux, editors. *Micelles, Membranes, Microemulsions and Monolayers*. Springer Verlag, Berlin, Germany, 1994.

[3] J. C. Shelley and M. Y. Shelley. *Curr. Opin. Coll. Int. Sci.*, 5:101, 2000.

[4] R. Goetz and R. Lipowsky. *J. Chem. Phys.*, 108:7397, 1998.

[5] S.J. Marrink, D. P. Tieleman, and A. E. Mark. *J. Phys. Chem. B*, 104:12165, 2000.

[6] D. P. Tieleman, S. J. Marrink, and H. J. C. Berendsen. *Biochim. Biophys. Acta*, 1331:235, 1997.

[7] S. E. Feller and R. W. Pastor. *J. Chem. Phys.*, 111:1281, 1999.

[8] S. E. Feller. *Curr. Opin. Coll. Int. Sci.*, 5:217, 2000.

[9] R. Goetz, G. Gompper, and R. Lipowsky. *Phys. Rev. Lett.*, 82:221, 1999.

[10] E. Lindahl and O. Edholm. *BioPhys. J.*, 79:426, 2000.

[11] S.J. Marrink and A. E. Mark. *J. Phys. Chem. B*, 105:6122, 2001.

[12] W. K. den Otter and W. J. Briels. *J. Chem. Phys.*, 118:4712, 2003.

[13] J. B. Maillet, V. Lachet, and P. V. Coveney. *Phys. Chem. Chem. Phys.*, 1:5277, 1999.

[14] P.K. Maiti, Y. Lansac, M. A. Glaser, and N. A. Clark. *Langmuir*, 18:1908, 2002.

[15] L. M. Walker. *Curr. Opin. Coll. Int. Sci.*, 6:451, 2001.

[16] G. C. Maitland. *Curr. Opin. Coll. Int. Sci.*, 5:301, 2000.

[17] Y. Rouault. *J. Chem. Phys.*, 111:9859, 1999.

[18] M. Kröger and R. Makhloufi. *Phys. Rev. E*, 53:2531, 1996.

[19] W. Smith and T. R. Forester. *J. Mol. Graphics*, 14:136, 1996.

[20] H. J. C. Berendsen, J. M. Postma, W. F. van Gunsteren, A. Di Nola, and J. R. Haak. *J. Chem. Phys.*, 81:3684, 1984.

[21] W. K. den Otter. *J. Chem. Phys.*, 123:214906, 2005.

[22] L. D. Landau and E. M. Lifshitz. *Statistical Physics, Part 1*, volume 5 of *Course of Theoretical Physics*, pages 396–400. Butterworth-Heinemann, Oxford, UK, 3 edition, 1999.

[23] L. J. Magid. *J. Phys. Chem. B*, 102:4064, 1998.

[24] R. P. Feynman, R. B. Leighton, and M. Sands. *The Feynman Lectures on Physics*, volume II, chapter 38-5. Addison-Wesley, Reading, MA, 1966.

[25] M. Doi and S. F. Edwards. *The theory of polymer dynamics*, chapter 2. Clarendon press, Oxford, U.K., 1998.

# Summary

The dynamical properties of membranes, i.e., lipid bilayers, in aqueous solvent have been investigated by means of coarse-grained molecular dynamics simulations. Because of their amphiphilic nature, lipids dissolved in water can form a wide range of clusters, from spherical globules and worm-like micelles to bilayers and vesicles, where the hydrophobic tails of the lipids are shielded from the surrounding solvent by their hydrophilic heads. The particular lipids simulated here self-assemble into a bilayer-structure, which is mirror symmetric with respect to its mid-plane. Because bilayers are held together by relative weak non-bonded interaction forces, they behave in many respects as two-dimensional liquids suspended in a three-dimensional solvent matrix. This makes bilayers very susceptible to external forces, which give rise to deformations of the overall shape of the bilayer and to flow within the bilayer.

The main goal of the current investigation is to establish methods to determine both the surface shear viscosity and the intermonolayer friction coefficient of the bilayer by means of computer simulations on the molecular level. The methods are tested using two well-known contemporary coarse-grained amphiphilic models by Goetz and Lipowsky and by Marrink *et al.*.

In chapter 2 the coarse-grained model bilayer was exposed to two shear flows directed along the bilayer surface. The first field, with a vorticity perpendicular to the bilayer, induces a regular shear deformation in the bilayer. The resistance of the bilayer against this flow is characterized by a two-dimensional surface viscosity, which, analogous to the three-dimensional viscosity, relates the shear force per unit of length of bilayer to the shear rate. The second flow field, with a vorticity parallel to the bilayer, causes the two constituent monolayers to slide past one another. A friction coefficient is defined by the ratio between the sliding force per unit of bilayer area and the velocity difference between the two monolayers.

The main results of chapters 3 and 4 are a confirmation of the theory by Seifert and Langer describing the relaxation dynamics of undulations in lipid bilayers, and the conclusion, illustrated by the presented molecular dynamics simulations, that at length scales below $\sim 0.1\mu$m the relaxations are dominated by intermonolayer friction. The relaxation times

that follow from these equilibrium simulations confirm the intermonolayer friction coefficient deduced from the non-equilibrium simulations in chapter 2. An accurate estimate of the intermonolayer friction coefficient is not only interesting by itself, as a key parameter in a study on bilayer dynamics, but also because of its indirect, and hitherto largely unappreciated, consequences for the calculation of bilayer bending rigidities, and possibly also other static properties, by molecular dynamics simulations.

In chapter 5, the single-tail coarse-grained lipid model by Goetz and Lipowsky has been extended with pairwise-additive friction and random forces, because the bilayer dynamics obtained with the original model was considerably faster than that of experimental bilayers. Although the model now reproduces the experimental viscosities of water and liquid alkanes, the slowing-down of the bilayer dynamics is insufficient to recover quantitative agreement with experimental data. A similar discrepancy was observed for the double-tailed coarse-grained lipid model by Marrink *et al.*. By varying the tail lengths we observe two clear trends for the flow properties of bilayers. The intermonolayer friction coefficient is sensitive to the asymmetry of the tails, which roughens the interface between the two monolayers by interdigitation of the longer tails. The surface shear viscosity is modulated by the combined lengths of the two tails, and hardly varies with the asymmetry of the tails. Experimental data to compare these results against are rare, and we express the expectation that the current work inspires future experimental and simulation studies on the flow properties of bilayers in relation to their lipid composition.

In chapter 6 we use molecular dynamic simulations to calculate the mechanical properties of a coarse-grained amphiphilic worm-like micelle. First of all we demonstrate that our worm is inherently stable, i.e., it does not depend on periodic boundary conditions for its continued survival, which sets it apart from some, and perhaps even all, previously simulated worms. We have shown that a force field based on the Lipowsky model, as used in the simulations, meets the stability criteria only after a fourfold increase of the volume of the head particle. The averaged structure factors of a thermally-excited tensionless worm in a periodic simulation box scale with the wave number according to $S \sim q^{-4}$, as predicted by the Helfrich model. The persistence length and bending rigidity are obtained from the proportionality constant. We observed pronounced differences between the worm's response to elongation and compression. When stretched, the undulations of all modes decrease, the

contour length increases, and the line tension becomes linear in the height of the simulation box. Under strong compression the undulations of only the first mode increase, while the contour length and the line tension reach a plateau value: the worm buckles. Both cases agree well with the Helfrich model.

# Samenvatting

De dynamische eigenschappen van membranen, oftewel lipide bilagen, opgelost in water zijn onderzocht met gecoarse-grainde moleculaire dynamica simulaties. Door hun amfifiele karakter kunnen lipiden in water een breed scala aan clusters vormen, van bolvormige en worm-achtige micellen tot bilagen en vesicles, waarbij de hydrofobe staarten van de lipiden worden afgeschermd van het omringende water door hun hydrofiele koppen. De lipiden die hier worden gesimuleerd zelf-assembleren in een bilaag structuur, met spiegelsymmetrie in het midvlak. Omdat bilagen door relatief zwakke niet-covalente interactiekrachten bij elkaar worden gehouden gedragen ze zich in veel opzichten als twee-dimensionale vloeistoffen gesuspendeerd in een drie-dimensionale achtergrond vloeistof. Dit maakt bilagen erg gevoelig voor externe krachten, die gemakkelijk deformaties van de globale vorm en stromingen binnen de bilaag veroorzaken.

Het hoofddoel van dit onderzoek is om methoden te ontwikkelen om zowel de oppervlakte afschuifviscositeit als de intermonolaag frictiecoëfficiënt van een bilaag te bepalen middels computersimulaties op het moleculaire niveau. De methoden zijn getest met twee bekende recente gecoarse-grainde amfifiele modellen, geïntroduceerd door Goetz en Lipowsky en door Marrink en collega's.

In hoofdstuk 2 wordt de gecoarse-grained model bilaag onderworpen aan twee langs het bilaagoppervlak gerichte afschuifstromingen. Het eerste veld, met een vorticiteit loodrecht op de bilaag, induceert een reguliere afschuifstroming in de bilaag. De weerstand van de bilaag tegen deze stroming wordt gekarakteriseerd door een twee-dimensionale oppervlakte viscositeit die, analoog aan de bekende drie-dimensionale viscositeit, de afschuifkracht per eenheid lengte van de bilaag relateert aan de afschuifstroomsnelheid. Bij het tweede stromingsveld, met een vorticiteit parallel aan de bilaag, slippen de twee samenstellende monolagen langs elkaar. Een frictiecoëfficiënt wordt gedefiniëerd als de verhouding van de slipkracht per eenheid bilaagoppervlak en het snelheidsverschil tussen de monolagen.

De belangrijkste resultaten van hoofdstukken 3 en 4 zijn een bevestiging van de theorie van Seifert en Langer, die de relaxatiedynamica van undulaties in bilagen beschrijft, en de conclusie, ondersteund door de gepresenteerde moleculaire dynamica simulaties, dat

de relaxaties gedomineerd worden door de intermonolaagfrictie op lengteschalen beneden $\sim 0.1\mu$m. De relaxatietijden die uit deze evenwichtssimulaties volgen bevestigen de intermonolaag frictiecoëfficiënt die uit de niet-evenwichtssimulaties van hoofdstuk 2 werd afgeleid. Een accurate schatting van de intermonolaag frictiecoëfficiënt blijkt niet alleen van belang als een centrale parameter in de beschrijving van bilaagdynamica, maar ook wegens zijn voorheen onderschatte consequenties in de berekening van de bilaagbuigbaarheidscoëfficiënt, en mogelijk andere statische eigenschappen, middels moleculaire dynamica simulaties.

In hoofdstuk 5 wordt het gecoarse-grainde lipide model van Goetz en Lipowsky uitgebreid met paarwijs-optelbare frictie en random krachten, omdat de bilaag dynamica van het originele model aanzienlijk sneller is dan dat van experimentele bilagen. Alhoewel het model nu de experimentele viscositeiten van water en vloeibare alkanen reproduceert blijkt de vertraging van de bilaagdynamica onvoldoende om een kwantitatieve overeenstemming met de experimentele data te bewerkstelligen. Een gelijksoortige discrepantie wordt gevonden met de twee-staartige model lipiden van Marrink en collega's. Door de staartlengtes te variëren observeren we twee duidelijke trends in de stromingseigenschappen van bilagen. De intermonolaagfrictiecoëfficiënt is gevoelig voor de asymmetrie van de staarten, omdat het scheidingsvlak tussen de twee monolagen ruwer wordt door verstrengelingen van de lange staarten. De oppervlakteafschuivingsviscositeit wordt gemoduleerd door de gecombineerde lengte van de staarten, en variëert nauwelijks met de asymmetrie van de staarten. Experimentele gegevens om deze resultaten mee te vergelijken zijn zeldzaam, en we hopen dat het huidige werk een inspiratie is voor toekomstig experimenteel en simulatie onderzoek naar de stromingseigenschappen van bilagen in relatie tot hun samenstellende lipiden.

In hoofdstuk 6 gebruiken we moleculaire dynamica simulaties om de mechanische eigenschappen van een gecoarse-grainde amfifiele worm-achtige micelle te berekenen. Allereerst tonen we aan dat het model inherent stabiel is - de worm is voor zijn overleving niet van de periodieke randvoorwaarden afhankelijk - waarmee het model zich onderscheidt van veel, en mogelijk zelfs alle, voorgaande simulaties van wormen. We tonen aan dat een krachtenveld gebaseerd op het Lipowsky model, zoals gebruikt in de simulaties, pas aan de stabiliteitscriteria voldoet na een viervoudige vergroting van het volume van het kopdeeltje. De gemiddelde structuurfactoren van een thermisch geëxciteerde spanningsloze worm in een periodieke si-

mulatiedoos schalen met het golfgetal als $S \sim q^4$, zoals voorspeld door het Helfrich model. De persistentielengte en de buigbaarheidscoëfficiënt volgen dan uit de evenredigheidsfactor. We zien een opmerkelijk verschil tussen de respons van de worm op elongatie en compressie. Onder rek nemen de undulaties van alle modes af, de contourlengte neemt toe, en de lijnspanning wordt linear in de lengte van de simulatiedoos. Onder sterke compressie nemen alleen de undulaties van de eerste mode toe, terwijl de contourlengte en de lijnspanning een plateau bereiken: de worm knikt. Beide situaties kunnen worden beschreven met het Helfrich model.

# Acknowledgements

The thesis you are reading is the result of extensive work carried out in almost five years. All these five years I have been working, living, and communicating with people. Contacts with them gave me a lot of support and stimulation to finish the thesis. And now, when the period of working on the thesis has almost finished, it is time to express my gratefulness to those people.

First of all my gratitude goes to my mother, who is always on my mind. For me she was the greatest stimulus to finish my work. I feel the deepest sense of gratitude to my promotor, Professor Wim Briels, who gave me his fatherlike attention and favour. I am grateful to my direct supervisor Wouter den Otter for his patience during his work with me and for the effort he made to integrate me successfully in the Dutch society. His enormous knowledge-database and working capacity are a classical example for me.

I am grateful to my father, my brother and his family. They helped me to become who I am. Thanks to Yuriy Zatovskiy who helped me to find this OIO position at University of Twente. Special thanks go to the families Belov, Ovsyanko, and Tolpekin for moral and spiritual support as well as for tasty dinners. Separate thanks to Paolo Baraggia, for nice communication and a pleasant chess-mate. Sincere thanks to Aleksandr Novogilov, Petr Khomyakov, Nina Dziomkina, Ivan Nikolaev, and VAVAN for making this time interesting and pleasant. Thanks to my parents-in-law Jack and Jeanne van Huijkelom for all their love and interest they showed in me. My dear roommate Peter Kindt and colleagues Albert van den Noort, Amol Thakre, Johan Padding, Yu-Guo Tao and Marieke Janssen. Finally, I thank my wife Eefje and my daughter Leoni, for their love, support, patience, and understanding in allowing me to spend so much time on this thesis.

Sergey Alfredovich Shkulipa.
Enschede, The Netherlands,
November 2006.

# About the author

Sergey Alfredovich Shkulipa was born on March 1, 1976 in Odessa, in The Union of Soviet Socialist Republics. After graduation from Richelieu Lyceum in 1992, he studied at the Faculty of Mathematics and Mechanics at the Odessa State University. His graduation work was carried out at the Theoretical Mechanics and Aero-hydrodynamics group of Prof. Dr. S. K. Aslanov and was concentrated on the mathematical description of shock and detonation wave propagations. After graduating from the Odessa State University in 1997, he stayed in the same group for a postgraduate program. In 1997-2000 he worked as a teacher of Mathematics and Computer Science, in the Odessa Richelieu Natural Sciences Lyceum, Ukraine. In December of 2001, he joined the Computational Biophysics group, which at that time was called the Computational Dispersion Rheology group, at the University of Twente in the Netherlands, and started his Ph.D. study under the supervision of Prof. Dr. W. J. Briels. During his Ph.D. he investigated the mechanical properties of amphipilic ensembles using computer simulations. The results of his Ph.D. research are described in this thesis. Since September 2006, he works at ASML in Veldhoven, the Netherlands.